A FINITE ELEMENT STUDY OF STEEL RAFTER TO CONCRETE RING BEAM CONNECTIONS USED IN TRINIDAD & TOBAGO

A Thesis
Submitted in Partial Fulfilment of the Requirements for the Degree of
Master of Science in Civil Engineering

of
The University of the West Indies

Alden Daniel
2022

Department of Civil and Environmental Engineering
Faculty of Engineering
St. Augustine Campus

THE UNIVERSITY OF THE WEST INDIES
School for Graduate Studies and Research

DECLARATION FORM FOR THE REPRODUCTION OF THESIS/RESEARCH PAPER/PROJECT REPORT

A thesis/research paper/project report which is accepted by the University for the award of a Higher Degree is placed in the University Libraries, and an electronic copy may be placed in an open access institutional repository. The copyright of the thesis/research paper/project report is retained by the author.

THIS DECLARATION MUST BE COMPLETED AND RETURNED WITH THREE (3) UNBOUND COPIES OF THE REVISED THESIS TO THE CAMPUS OFFICE OF GRADUATE STUDIES AND RESEARCH

To be completed by the candidate

NAME IN FULL (Block capitals**)** _____

TITLE OF THESIS/RESEARCH PAPER/PROJECT REPORT: _____

_____

_____

DEGREE FOR WHICH THESIS/RESEARCH PAPER/PROJECT REPORT IS PRESENTED:

_____

To be completed by the University

DATE OF AWARD OF DEGREE: _____

DECLARATION

1. I authorise The University of the West Indies, subject to the conditions set out in paragraph 3 below, to make a microform or digital copy of my thesis/research paper/project report for its preservation and for the purpose of inter-library loan and supply of copies.
2. I recognise that my thesis/research paper/project report will be made available for public reference, inter-library loan and copying.
3. I understand that before any person is permitted to read, borrow or reproduce a single copy of my thesis/research paper/project report he/she will be required to sign the following declaration: "I recognise that the copyright of the above mentioned thesis/research paper/project report rests with the author. No information derived from it may be published without acknowledgement, and no part of the work may be reproduced in any form without the prior written consent of the author."
4. I warrant that this authorisation does not, to the best of my belief, infringe the rights of any third party.

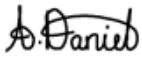

_____ _____

Signature of Student Date

Note: A candidate may apply to the Senate at the time of submitting the thesis/research paper/project report for deposit in the Libraries or thereafter:-

1. To retain personally for three years the sole right to grant permission to copy his/her work for distribution.
2. To withhold the thesis/research paper/project report and its abstract from access for a period of one year provided that he/she shows either evidence of having applied for a patent in respect of his/her work, or other good cause. Application may be made for withholding the thesis/research paper/project report and its abstract from access for a further period but approval will only very exceptionally be given for a period exceeding three years overall.

ABSTRACT

A Finite Element Study of Steel Rafter to Concrete Ring Beam Connections Used in Trinidad & Tobago

Alden Daniel

Rafter to ring beam connections are the most critical connections in a roof as their failure can result in dislodgement of the entire roof along with its framing and covering. The aim of this study was to conduct a finite element analysis study on the performance of some of the non-coded steel rafter to concrete ring beam connections used in Trinidad and Tobago. The most popular of these connections involve using steel rebars that are cast into the ring beam and subsequently welded to the rafter. Nine versions of this connection were identified and categorized as Type 2 & Type 3. The Type 2 Connections are those in which the rebars are welded to the top flange of the rafter and the Type 3 Connections are those in which the rebars are welded to the bottom flange of the rafter. The Type 2 and Type 3 connections consisted of several variations including mechanically anchoring the rebar to the rafter without welds, using one and two rebars, varying of the rebar embedment depth and using 90 degree and straight rebars. A Type 1 standard, code-compliant, bolted-endplate connection was used as the control for the investigation. The connections were analysed using “ABAQUS” and the maximum load resistances were compared with computed category 1 hurricane loads for this region. The load capacities of all the connections were found to be lower than the control connection but were still adequate for hurricane category 1 loads, with the exception of the connection in which the rebars were mechanically anchored to the rafter without welds. The Type 2 connections were less stiff, experienced larger rafter displacements, inflicted less damage on the concrete ring beam, and required less rebar embedment to prevent pull-out failure than the Type 3 connections.

Keywords: Alden Daniel; Rafter; Ring Beam; Rafter Connection; Finite Element Analysis; Bond Strength; Damage Plasticity; Bond-Slip; Development Length; Embedment Depth; Pull-out Test; Abaqus; Von Mises, Wind Load; Roof Loads.

TABLE OF CONTENTS

LIST OF FIGURES

LIST OF TABLES

LIST OF PHOTOS

CHAPTER 1

INTRODUCTION

1.1 Background

Trinidad and Tobago is geographically positioned near the southern edge of the hurricane belt and is therefore at risk for being struck by major hurricanes. Its close proximity to the equator at approximately 10.6 degrees latitude, subjects it to high temperatures and humidity that provides the perfect fuel for hurricanes. Over the years, this has been exacerbated by seasonal climate change as a direct effect of global warming and which has resulted in more frequent and intense occurrences of these events. According to Prevatt, Dupigny-Giroux, and Masters (2010), the 21st century has seen a southward shift in the hurricane belt which has increased the exposure and risks to hurricanes for Trinidad and Tobago and other islands of the Lesser Antilles. Data from the National Weather Service and the National Oceanic and Atmospheric Administration (NOAA) shows that every year during the hurricane season, an average of 13 tropical storms pass through the Caribbean, six of which develop into hurricanes that cause damage to roofs and other property, resulting in major financial losses.

The Caribbean region comprises of developing countries with many low budget houses built using substandard construction techniques and materials. The most exposed and vulnerable part of a house when subjected to high winds is the roof. Roofs make up a large percentage of the overall cost of a house and are sometimes the first part of a structure to get destroyed during a hurricane. A roof consists of various elements including the roof covering, the roof frame and the connections that hold them together. In a typical roof configuration, the roof covering is connected to the roof frame via purlins and the roof frame is then connected to the building's frame. The roof frame typically consists of rafters and in this context, the building frame can be considered as just the ring beam. This connection of the rafter to the ring beam is considered the most critical roof

connection because it serves as the final point of support for the roof, and is therefore the point where all wind loads culminate before being transferred to the ring beam. When this connection fails, the entire roof inclusive of the roof covering, the purlins, the rafters and all the other connections are blown away.

In the Caribbean gable and hip roofs are two of the most popular roof configurations and the frame for these roofs are traditionally constructed using timber rafters. Gibbs (2000) pointed out that a major deficiency in the use of timber rafters is the longitudinal splitting of the rafter with the top half disappearing with the roof-covering and leaving the bottom half in place. The splits originate and propagate from the holes drilled horizontally through the rafters to receive the holding-down rods. In recent times, steel rafters are being used in lieu of timber rafters, particularly in Trinidad and Tobago where structural steel has become a very popular building material. The use of steel rafters has eliminated the failure mode of rafter splitting but there have still been numerous instances of steel framed roofs being completely dislodged when subjected to winds lower than hurricane category winds. It is apparent that the switch from timber rafters to steel rafters has shifted the point of failure from the rafter itself towards its connection with the ring beam. The proliferation of this new failure mode reinforces the need for more attention to be paid to the way steel rafters are connected to ring beams.

The depth of the steel rafters that are typically used in low budget residential construction in Trinidad and Tobago is between four and six inches, while in high end residential and commercial construction the rafters are much larger. The larger rafters used in high end residential and commercial construction are typically connected to the ring beam using expensive steel appendages such as rafter stubs and baseplates which are welded to the rafter and bolted to the concrete ring beam. These appendages are seldom used in low budget residential construction due to the cost associated with the extra materials required for their installation. They are also more difficult to physically “fit-up” within the restricted space around the smaller rafters used in residential construction. As a result of these limitations, local builders have resorted to innovative, less

expensive and uncomplicated alternatives to secure the steel rafters to the concrete ring beam. One such connection that has become quite popular and is being used extensively across the country involves the embedment of one or two rebars into the concrete ring beam which is then site welded directly to the rafter. This connection eliminates the need for expensive baseplates, welds and bolts.

This popular connection type is not featured in any building code or design guide so there is no standard governing its application. As a consequence of this, local builders have been afforded the freedom to further improvise the connection to suit their preference or to overcome on site challenges. The connection has since morphed into various versions. In some instances, one rebar is used to fix the rafter and in some instances two rebars are used. The rebar(s) is sometimes welded to the top flange of the rafter and sometimes it is welded to the bottom flange. In other variations, the length or diameter of the rebar is varied and the rebar is sometimes embedded into the concrete ring beam with a straight end and sometimes with a hooked end.

Given the increasing popularity of this connection type and the absence of a documented standard to govern its use, it would be worthwhile investigate its behaviour and adequacy. This paper therefore presents a study utilizing computer-aided finite element analysis to investigate the performance of the various versions of this connection type.

Photo 1: Entire roof blown off in Point Fortin Trinidad

Source: Webb (2019)

Photo 2: Entire roof blown off in Point Fortin Trinidad

Source: Braxton-Benjamin (2021)

Photo 3: Roof partially blown off in Chase Village Trinidad

Source: Holder (2020)

1.2 Problem Statement

Small building contractors have been constructing non-coded steel rafter to concrete ring beam connections especially on low budget residential buildings. This is either due to financial constraints or simplicity. While these connections may resist failure under normal loading conditions, they may fail under the moderate to high loads that are produced by hurricanes. In Trinidad and Tobago, we have seen many instances of entire roofs being blown away when their steel rafters dislodge from the concrete ring beam. This is an indication that more attention needs to be paid to the anchoring of steel rafters to concrete ring beams.

1.3 Hypothesis

1. The non-coded steel rafter to concrete ring beam connections used in local residential construction cannot withstand the wind loads recommended by

the relevant building codes. In Trinidad and Tobago, this wind load is equivalent to that produced by a category 1 hurricane.

2. The non-coded steel rafter to concrete ring beam connections used in local residential construction are likely to fail either by pull-out of the anchors or by yielding of the anchors or both.

1.4 Research Questions

1. What are the non-coded steel rafter to concrete ring beam connections used in residential construction?
2. What are the stresses in these connections when subjected to code prescribed loads?
3. How much force can these connections withstand before failure?
4. How are these connections likely to fail?

1.5 Aim

To conduct a finite element analysis study on the performance of some of the non-coded steel rafter to concrete ring beam connections used in Trinidad and Tobago.

1.6 Objectives

General Objectives:

1. To identify the different types of non-coded steel rafter to concrete ring beam connections used in residential construction in Trinidad and Tobago.
2. To conduct a finite element analysis study on the performance of non-coded steel rafter to concrete ring beam connections when subjected to code prescribed loads.

Specific Objectives:

To develop a finite element model to simulate the pull-out action of an embedded steel bar in concrete in order to:

1. Study the bond-slip behaviour between an embedded steel bar and concrete and
2. Study the damage behaviour of concrete when subjected to the pull-out action of an embedded steel bar.

1.7 Scope / Limitations

1. Roof Configuration & Member Sizes:

1.0.1 **Roof Eave** length is 600mm from the centerline of the ring beam to edge of the rafter.

1.0.2 **Rafters** are 89mm wide by 152mm deep structural steel members with a weight of 16kg/m.

1.0.3 **Ring Beams** are 150mm wide by 200mm deep unreinforced concrete beams.

2. Roof Connection:

2.0.1 **Anchor Rods** are 12mm diameter, grade 40, mild steel rebars as these are readily available and are more suitable for welding. High tensile deformed rebars were not considered since they are not suitable for welding.

2.0.2 **Anchor bolts** are 12mm diameter, 150mm long, A325 high strength bolts.

2.0.3 **Base Plate thickness** is 12mm.

3. Load Application:

3.0.1 **Wind Load** is applied as a static uplift force on the rafters and is based on the loading requirements of the ASCE 7 code.

3.0.2 **Failure load** is considered as the first load which causes failure in any one of the connection elements or parts.

4. Material Strength:

4.0.1 **Concrete** compressive strength is 20MPa cylinder strength.

4.0.2 **Structural Steel** for the rafter is grade ASTM A992 with a yield strength of 345MPa.

4.0.3 **Reinforcement/Anchor Rods** is ASTM A615 mild steel rebar with a yield strength of 275MPa.

4.0.4 **Welds** are assumed to be constructed with E70 welding electrodes with a minimum tensile strength of 490MPa and carried out in accordance with the specifications of the American welding society (AWS D1.1).

5. Wind Load Design Criteria:

5.0.1 **Wind Load design criteria** is based on the ASCE 7 code requirements. The **building height** for the design load is three stories since most low budget residential homes are limited to this height. i.e. approximately 40 feet from ground to roof apex. A **wind speed** of 117 mph was used as the design wind speed in accordance with the recommendations of the Design Branch of the Ministry of Works in Trinidad and Tobago. This wind speed is associated with a category 1 hurricane. Exposure category D was assumed, this category is associated with buildings located near the shore line or near open water. This represents the worst-case loading condition since buildings in the Caribbean are commonly constructed near the sea.

5.0.2 **Importance category** two (2) was used for residential buildings.

5.0.3 **Rafter Spans** were varied between a maximum of 12 meters and a minimum of 6 meters. These spacings are typically used in residential construction.

5.0.4 **Rafter Tributary Width** or space between adjacent rafter frames was varied between a maximum of 6 meters and a minimum of 3 meters. These spacings are typically used in residential construction.

5.0.5 **Roof Slope** or pitch is 15 degrees which is a common slope used in residential construction. Flatter roof slopes experience higher uplift forces. The Trinidad and Tobago Small Building Committee (2004, 36) indicates that roof slopes between 0 degrees and 20 degrees are more vulnerable to uplift forces.

6. Finite Element Model

6.0.1 **Finite Element Program** used was ABAQUS software (SIMULIA, 2013).

6.0.2 **Concrete Damage Model** used was the concrete damaged plasticity model to simulating the complete behaviour of the concrete in both tension and compression as well as damage characteristics under static/dynamic and cyclic/monotonic loading.

6.0.3 **Bond Slip Model** used was the traction-separation model to capture cohesive behaviour, damage initiation and damage evolution at the concrete-steel interface.

6.0.4 **Steel Model** used was an elastoplastic steel model to capture both the elastic and plastic deformation characteristics of the steel elements.

CHAPTER 2

LITERATURE REVIEW

2.1 Introduction

The load resistance provided by the connections in this study, is primarily provided by steel rebars that are welded to the rafter and embedded in the ring beam. The embedment of the steel rebar in the concrete ring beam forms a composite material and therefore, there must be a mechanism to transfer loads from one material effectively to the other. This mechanism is the interfacial bond between the individual materials which is critical to the overall performance of the composite material and is therefore the main focus of this literature review.

2.2 Bond Stress and Failure Modes

When a reinforcing bar is embedded in concrete, the bond between the bar and the concrete allows them to function as a single monolithic body. This bond is due to chemical adhesion, friction and mechanical interlock due to surface imperfections in plain bars and ribs in deformed bars. If the bar is subjected to sufficient tensile or compressive forces, then the force has to be transferred from the bar to the concrete in the form of shear stresses. This shear stress is referred to as bond stress. In doing so, there is a gradual destruction of the adhesive bond occurring after the point of initial slip. While the adhesive bond is deteriorating, frictional forces begin to develop simultaneously due to surface roughness/imperfections in the bar and due to interaction of the bar ribs bearing on the concrete. As the bar continues to slip, frictional forces on the face of the bar reduces while frictional forces on the faces of the lugs continue to increase and take over as the principal mechanism of force transfer. As shown in figure 2 below, the bar faces experience both compressive and shear stresses which resolve into tensile stresses leading to the development of micro cracks in planes

both parallel and perpendicular to the bar. These cracks are known as Goto Cracks (Goto 1971) as shown in figure 1 (a) below, they may result in a conical failure surface. If the concrete cover is sufficiently small and or there is no lateral confinement, transverse cracks develop near the ribs and propagate towards the surface of the concrete, these cracks are known as splitting cracks as shown below in figure 1(c). This is also demonstrated in figure 3 below, where it is shown that the resultant force from the ribs is resolved into a force (u'=u tanB) which is perpendicular to the bar and which radiates towards the surface as splitting cracks. If there is sufficient cover, higher rates of loading or transverse reinforcement to prevent or delay splitting failure, the system will fail by shearing along a surface parallel to the bar at the tip of the ribs resulting in what is called pull-out failure, as shown in figure 1(d).

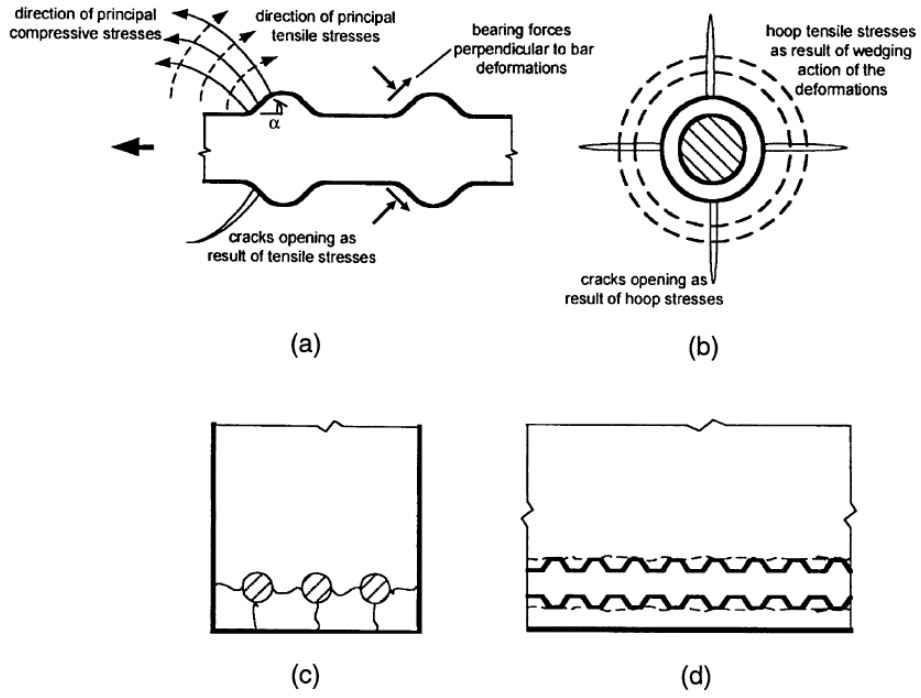

Figure 1: Cracking and damage mechanisms in bond

Source: ACI (2003, 4)

Note:(a) side view of a deformed bar with deformation face angle α showing formation of Goto (1971) cracks; (b) end view showing formation of splitting cracks parallel to the bar; (c) end view of a member showing splitting cracks

between bars and through the concrete cover; and (d) side view of member showing shear crack and/or local concrete crushing due to bar pull-out.

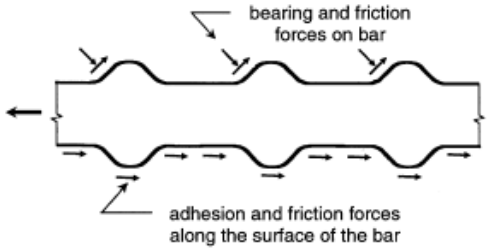

Figure 2: Bond force transfer mechanism

Source: ACI (2003, 3)

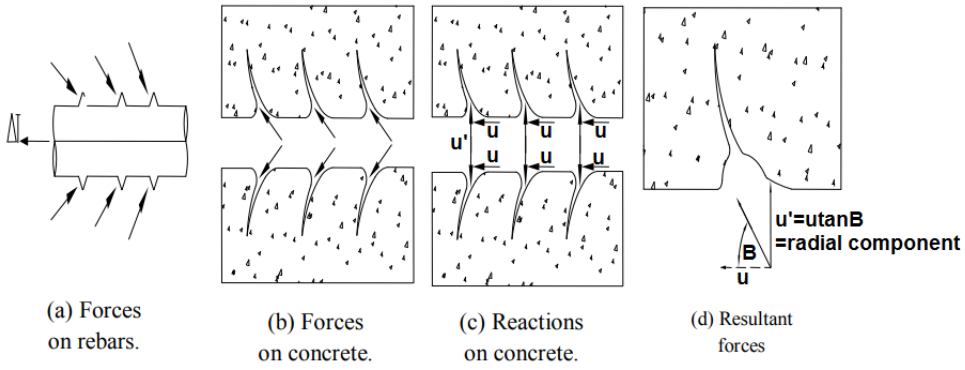

Figure 3: Transfer of forces

Source: Gangolu, Priyanka, and Eligehausen (2016, 2)

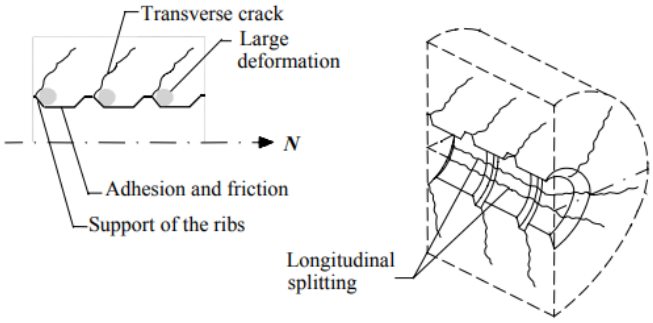

Figure 4: Deformation zones and cracking caused by bond

Source: Vandewalle (1992) as cited in Lundgren (1999, 12)

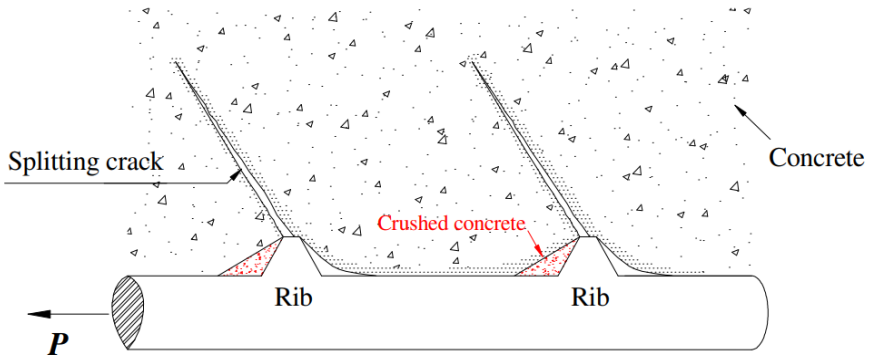

Figure 5: Mechanical interaction bet. concrete and deformed steel

Source: Lin et al. (2019, 1)

According to Tepfers (1973), the angle α between the principal compressive bond stress, see **figure 6** below, and the bar axis depends on whether there is adhesion bond left on the ribs and also on the rib face angle. The compression fields begin in a band around the lugs and expand outward at approximately 45º angles to form cones of compression, as shown in figure 6 below. The radial components of the bond forces are balanced against circumferential tensile stress rings in the concrete. The rings have their thinnest part in the concrete cover protecting the reinforcement and this is where longitudinal cracks tend to first appear when the ring is stressed to rupture. These cracks may first appear as internal cracks not visible from the outside surface of the concrete but may be initiated by tensile stress peaks without the ultimate tensile load capacity of the concrete ring being reached at the same time. When the ultimate load capacity is reached the ring breaks and a longitudinal crack appears. The concrete ring resistance falls and some movement between the reinforcing bar and the concrete takes place due to crushing of the concrete in front of the rings. The angle **α** between the bond force and the bar axis may change at this stage. The radial components of the bond forces load the concrete cantilever around the bar-the remainder of the concrete. The cantilevers are loaded to their ultimate capacity when they break following a failure pattern of minimum stressed surface.

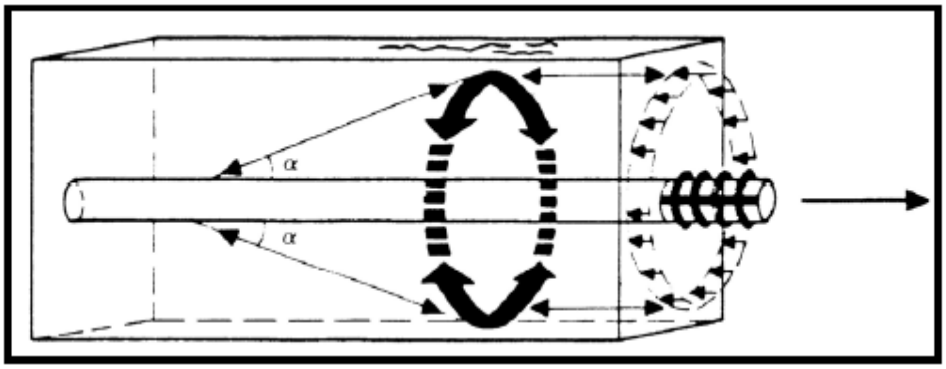

Figure 6: Schematic of internal forces within a RC specimen

Source: Tepfers (1973, 26)

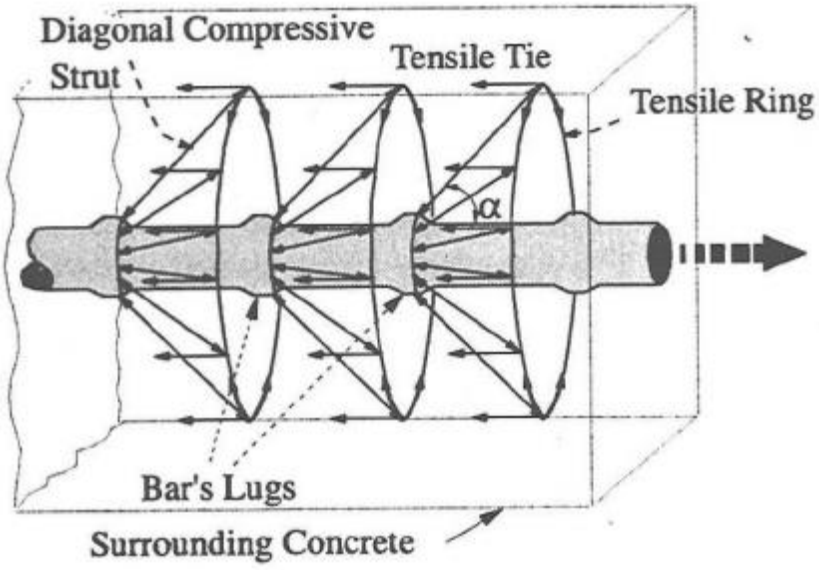

Figure 7: Ring tensile stresses

Source: Ensink et al. (2012, 11)

Figure 8: Concrete cylinder failing by splitting

Source: Bouazaoui and Li (2008, 107)

The transition between pull-out and splitting failure generally depends on the position of the bar, the bar surface, the transverse reinforcement and the concrete cover. According to Murcia-Delso, Stavridis, and Shing (2013), the transition of splitting failure to pull-out failure is stated for related concrete covers of c/d = 2.5 to 3.5. If the bar is sufficiently anchored and the stress in the rebar can become sufficiently high then the bar can fail by yielding and even strain hardening. The schematic bond-slip relationship between pull-out and splitting failure is shown below.

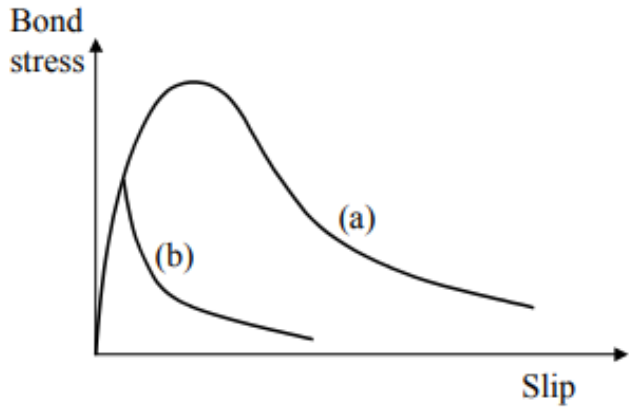

Figure 9: Schematic bond-slip relationship

Source: Lundgren (1999, 13)

Notes:(a) pull-out failure; (b) splitting failure, or loss of bond due to yielding of the reinforcement.

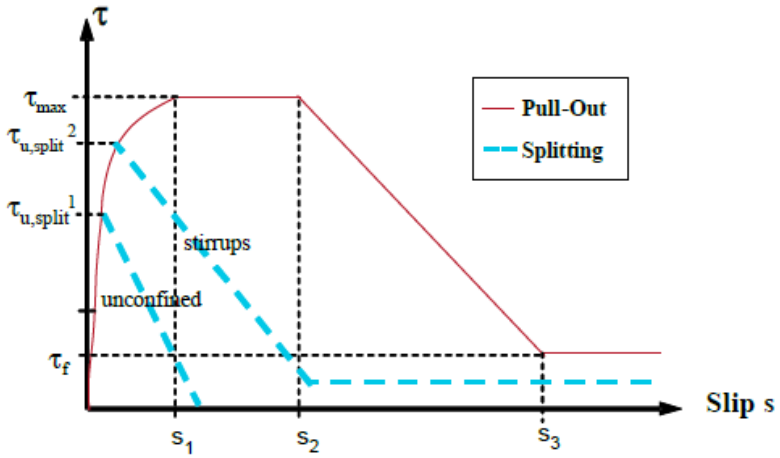

Figure 10: Analytical bond stress-slip relationship

Source: CEB FIB (2010)

ACI (2003) summarizes of the governing factors contributing to bond strength of a deformed bar embedded in concrete:

- The mechanical properties of the concrete (associated with tensile and bearing strength);
- The volume of the concrete around the bars (related to concrete cover and bar spacing parameters);
- The presence of confinement in the form of transverse reinforcement, which can delay and control crack propagation;
- The surface condition of the bar; and
- The geometry of the bar (deformation height, spacing, width, and face angle).

Figure 11 below shows a typical bond stress vs slip curve for a bar under monotonic loadings. ACI (2003) explains that the graph rises sharply because of adhesion until splitting cracks are formed, leading to softening of the curve. Where a splitting crack has opened and is unrestrained by confinement reinforcement the rebar ribs may slip without causing local damage to the concrete. If the loading rate is high or there is adequate confinement of the splitting cracks, the ribs tend to crush the concrete in between them forming effective ribs with a reduced face angle or forming a shear crack at the tip of the ribs as shown above in figure 1 (d). The phenomenon with the concrete forming a reduced face angle is also demonstrated in figure 14 below.

When a bar is cast in concrete and curing begins, shrinkage of the concrete occurs and the concrete tries to pull away from the rebar but is resisted by the adhesion forces at the interface. This action causes tensile stresses to develop at the interface leading to the development of micro cracks. These micro cracks are usually the initiation points for the development of splitting cracks when the bar is subsequently subjected to tensile loads.

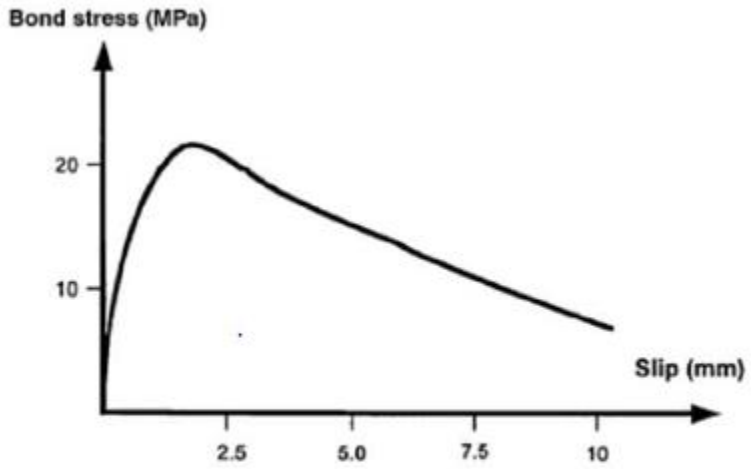

Figure 11: Bond stress vs slip curve for bar failing by pull-out

Source: Eligehausen, Popov, and Bertero (1982, 88)

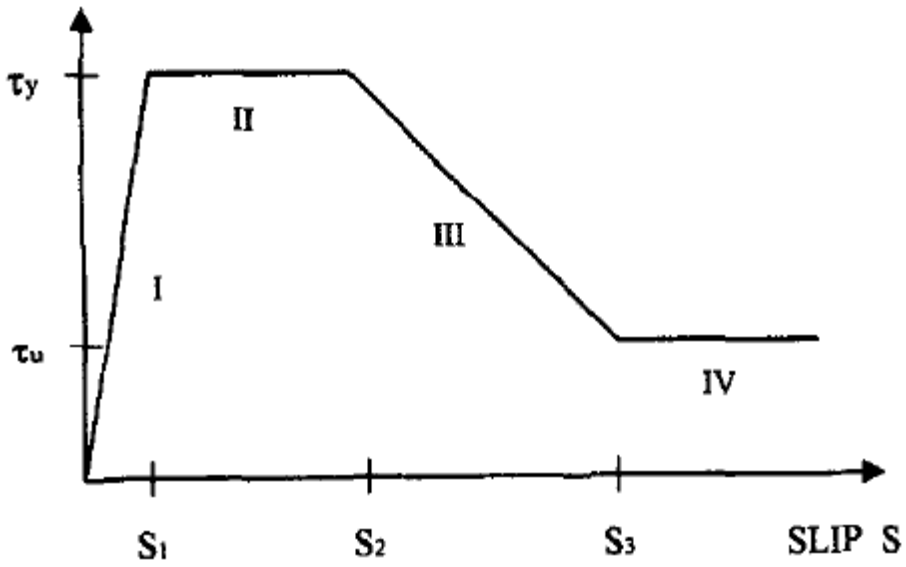

Figure 12: Idealized local bond-slip relationship

Source: Yankelevsky (1997, 783)

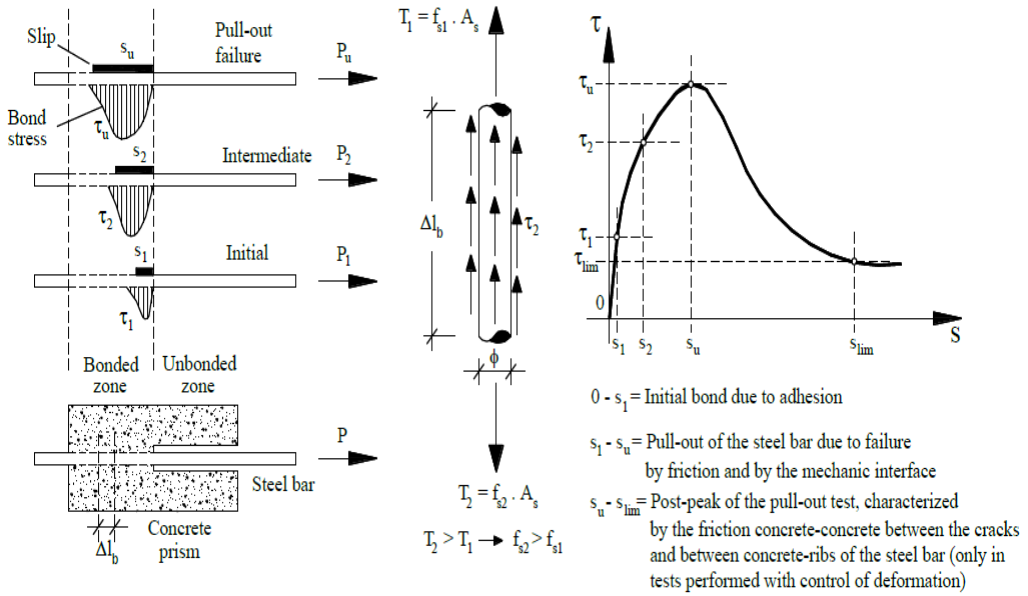

Figure 13: Bond stress and slip behaviour in pull-out test

Source: Filho, De Nardin, and Debs (2019, 3)

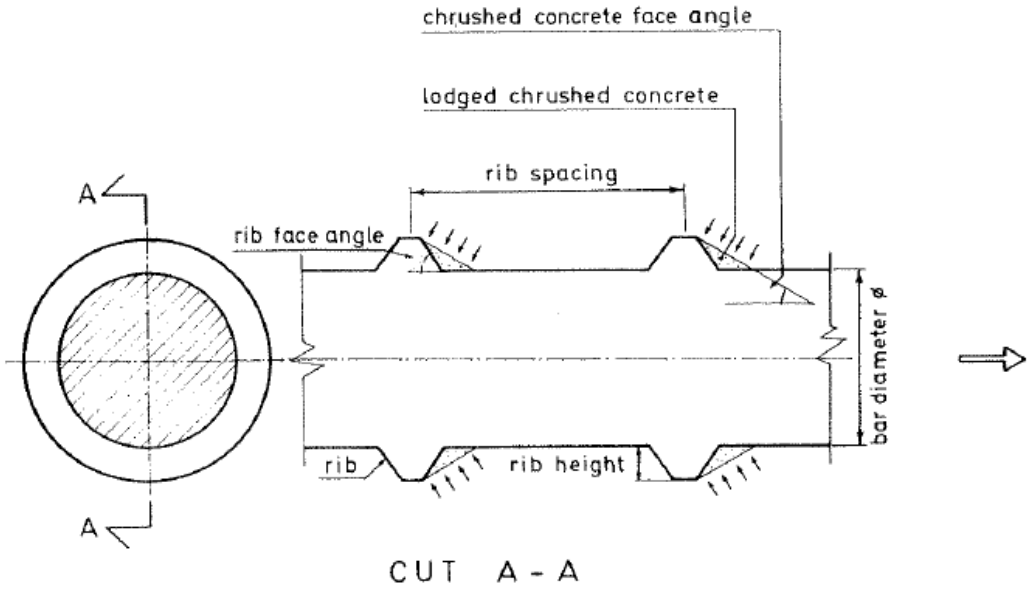

Figure 14: The geometry of rebar and mechanical interaction with concrete

Source: Tepfers (1973, 24)

Research done by Rehm and Van Amerongen (1961) and Lutz and Gergely (1967) identified the cause of failure of the bond between concrete and steel as either crushing of the concrete in front of the ribs and or splitting of the concrete by wedging action. The geometric rib parameter a/c was related to bond failure, this is the ratio of the rib height to the rib spacing. With closely spaced high ribs the failure mode of pull-out would govern due to the shearing of the concrete between the ribs. Conversely, when the rib spacing's are large, i.e. larger than 10 times the rib height, the partially crushed concrete would form a wedge in front of the ribs and the bar is more likely to fail by splitting. The two types of failures are shown below in figure 15.

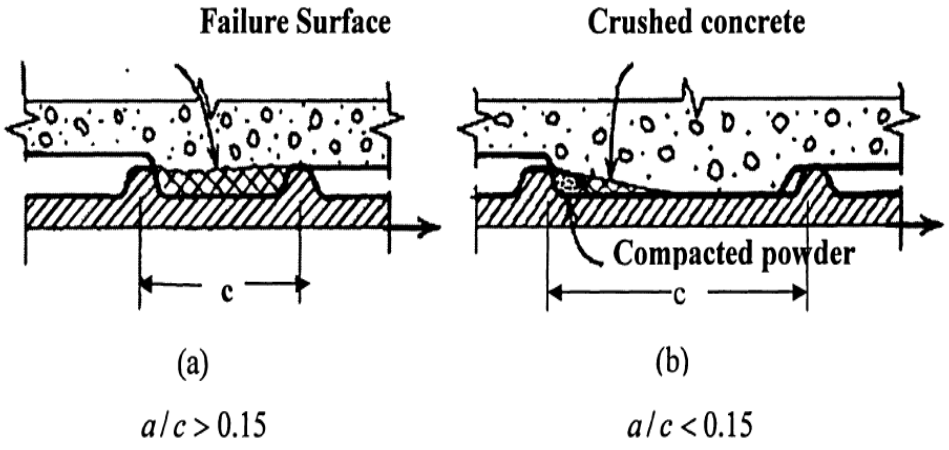

Figure 15: Failure mechanisms at the ribs of deformed bars

Source: Rehm and Van Amerongen (1961)

2.3 Factors Affecting Bond Strength

The bond between steel and concrete has been proven to be sensitive to many factors including, concrete strength, steel strength, embedment length, concrete cover thickness, rib spacing and geometry, concrete confinement, corrosion and temperature. A few of these factors are elaborated on in the proceeding sections based on works by previous researchers.

2.3.1 Concrete Strength

Bond stress is influenced by both compressive strength and tensile strength of concrete. For instance, bearing stress of the rebar ribs on the concrete induces high compressive stress on the concrete while the development of micro cracks is due to tensile stress forming perpendicular to the rebar.

Tepfers (1973) showed that when higher strength concrete is used, the slope of the bond stress distribution varies significantly over the length of the bar.

Martin (1982) observed that for a slip range of 0.1 to 1 mm, the bond stress is proportional to the compressive strength when concrete strength varies from 16 to 50 MPa. He also found that for a very small slip, less than 0.01 mm, and for a high slip, larger than 1 mm, the influence of concrete compressive strength is less important and proportional to the 2/3 power of the concrete compressive strength.

2.3.2 Cover Thickness

Bond strength is strongly influenced by the thickness of concrete cover between the rebar and the face of the concrete. This cover gives protection to the rebar and it provides confinement against the development of splitting cracks. According to Tepfers (1973), the increase in cover thickness results in improved bond strength and highly influences the mode of failure. He observed that higher concrete covers are likely to result in pull-out failure and low concrete covers tent to result in splitting failures. According to Murcia-Delso, Stavridis, and Shing (2013), the transition of splitting failure to pull-out failure is stated for related concrete covers of c/d = 2.5 to 3.5.

2.3.3 Bar Geometry

The geometry of the bar, mainly the height, width, spacing and angle of the ribs greatly influences the bond strength. Abrams (1913) who conducted the

first studies on concrete-steel bonds using pull-out tests, identified a relationship between the ratio of the bearing area of the projections (projected area measured perpendicular to the bar axis) and the entire surface area of the bar in the same length. He found that this ratio could be used as a metric for evaluating the bond strength of deformed bars. To improve bond strength, he recommended that this ratio be more than or equal to 0.2, this resulted in manufacturers reducing the spacing of these projections to less than what was being used commercially in deformed bars at the time.

Rehm and Van Amerongen (1961) was able to relate the geometric parameter a/c (rib height to rib spacing) to bond strength. He found that a ratio of 0.065 produced the most optimal bond strength for a deformed bar embedded in concrete.

According to Lutz and Gergely (1967) and Rehm and Van Amerongen (1961), bars with steep rib angles i.e. more than 40 degrees, slip occurs by crushing of the ribs in front of the ribs and with flat rib angles, slipping occurs as the ribs push the concrete away from the ribs.

Darwin and Graham (1993) related the relative rib area to the bond force slip response. The relative rib area can be taken as: projected rib area normal to the bar axis / (nominal bar perimeter x centre-to centre rib spacing). Under conditions of low confinement, the bond strength was found to be independent of the deformation pattern but under increased confinement by thicker bar cover or transverse reinforcement, the bond strength increases with the relative rib area.

ASTM (2016) recommends certain limits on the bar deformations. They recommend that the deformations be placed with respect to the axis of the bar such that the included angle is not less than 45°. Where the line of deformations forms an included angle with the axis of the bar from 45 to 70° inclusive, the deformations shall alternately reverse in direction on each side, or those on one side shall be reversed in direction from those on the opposite side. Where the line of deformations is over 70°, a reversal in direction shall not be required. The average spacing or distance between deformations on each side of the bar shall not exceed seven tenths of the nominal diameter of the bar. The overall length of

deformations shall be such that the gap (measured as a chord) between the ends of the deformations shall not exceed 12.5 % of the nominal perimeter of the bar. Where the ends terminate in a rib, the width of the rib shall be considered as the gap between these ends. The summation of the gaps shall not exceed 25 % of the nominal perimeter of the bar. The nominal perimeter of the bar shall be 3.1416 times the nominal diameter.

2.4 Research on Plain / Smooth Reinforcement

Abrams (1913) in his early studies on bond performance of plain bars using pull-out tests, proved that bond resistance of plain bars was inferior to that of deformed bars. He noted that the lack of ribs and surface deformations in plain reinforcement prevents effective transfer of bond forces by mechanical interlock. Instead, the bond forces are transferred via surface adhesion between the concrete and steel before slip occurs, and by wedging action of small concrete particles that break free upon slipping. Olesen, Sozen, and Siess (2008) showed that the bond between steel bars and concrete consists of the adhesive resistance and the micro-interlocking action due to the indentations of the plain bar surface and that the latter is the main factor. Wight and MacGregor (2011) suggested that the effectiveness of this bond mechanism may be affected by the Poisson effect which causes the bar under tension to reduce in cross sectional area. This reduction causes the steel to pull away from the concrete and therefor reducing its contact area with the concrete.

Abrams (1913) work also confirmed an allowable maximum bond stress of 0.04 f 'c for plain reinforcement. In pull-out tests conducted by Abrams (1913) on plain bars, bond resistance reached its maximum at a loaded end slip of about 0.01 in. (0.25 mm). For deformed bars, the load-slip performance was the same as for plain bars up to the slip corresponding to the maximum bond resistance of the plain bars.

Mylrea (1948) proposed bond stress distributions varying along the length of the bar in pull-out tests and suggested that the bond stress would reduce as the slip increased. These bond stress distributions were supposedly from empirical data since he did not present any theoretical validation for the relationship between bond slip and bond length. Mylrea cautioned that if there is insufficient bond along the length of the bar then there would be anchorage failure unless end anchors are provided. As a precaution, maximum allowable stresses were introduced in 1920 based on Abrams (1913) investigations and in 1951 end hooks were required on all plain rebars.

The 1993 CEB-FIP Model Code provided design guidelines for plain reinforcement and proposed a bond stress-slip model which also implied no loss of strength with increasing end slip in pull-out specimens. The curve reached a maximum bond stress of $0.3\sqrt{Fc'}$ at a slip of 0.1 mm and maintained this stress as the slip increased.

Edwards and Yannopoulos (1979) and Bennett and Snounou (1982) also demonstrated a relationship between bond stress, slip, and bar forces but Kankam (1997) was able to develop an empirical prediction model for tensile specimens reinforced with plain bars. However, this model also assumed no loss of bond stress with slip.

Early research conducted by Abrams and Mylrea concluded that bond stress decreased with increasing slip while later researchers CEB and Kankam suggested that bond stress remained constant with increasing slip. These bond models contradict each other and therefore the evaluation of pull-out specimens cannot be rationally solved without knowing which of the bond models are correct.

Xing et al. (2015) conducted a series of pull-out tests where plain bars were compared with deformed bars by varying embedment depth and diameter. The tests showed that the bond strength of plain bars was significantly smaller than deformed bars, roughly 18.3% of the deformed bars.

2.5 Pull-out Test Specifications

According to Sadeghi and Sharma (2019) there are different well known standards and references for investigating the bond strength between concrete and steel. One such standards is the popular The International Union of Laboratories and Experts in Construction Materials (1994) for pull-out tests. The standard involves the pulling out by applying a tension force in a static loading rate to a rebar cast into a square concrete prism. The force and the relative displacement between the rebar at the unloaded end and the concrete (bond slip) are monitored and recorded. The RILEM specifications recommends that the length of the bar be 10 times the bar diameter with a bond length of 5 times the bar diameter. A plastic sleeve is cast into the concrete to create a de-bonded zone at the front of the bar and to ensure that the bonded zone is exactly 5 times the bar diameter. The pull-out loading rate Vp is maintained at $Vp = 0.5d^s$(N/sec) where d is the diameter of the bar.

A 5mm thick rubber plate is placed beneath the concrete to reduce the friction between the concrete and the support steel plate because this friction can erroneously negate against splitting failure. Another potential deficiency in this setup is the fact that the concrete goes into compression while the rebar is in tension due to the concrete being restrained at the supporting plate. This boundary condition does not accurately simulate any real-life situations since in most cases, the rebar and the concrete are simultaneously in tension or compression. If the pull-out test is simulated using finite element analysis, the researcher has the flexibility to adjust the boundary conditions to suit the intended application, for instance, the boundary condition can be applied to the opposite side of the concrete prism so that the concrete would go into tension simultaneously with the rebar. Figure 16 below shows the pull-out test setup by Sadeghi and Sharma (2019).

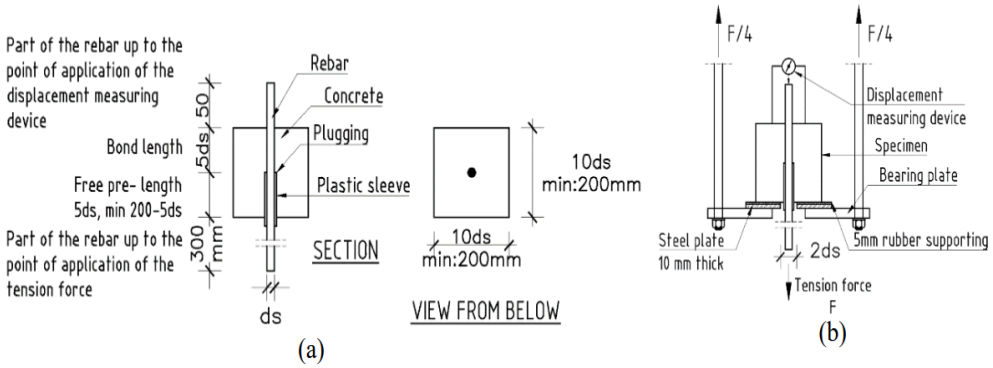

Figure 16: Pull-out test setup and specifications

Source: Sadeghi and Sharma (2019).

2.6 Pull-Out Tests Results by Other Researchers

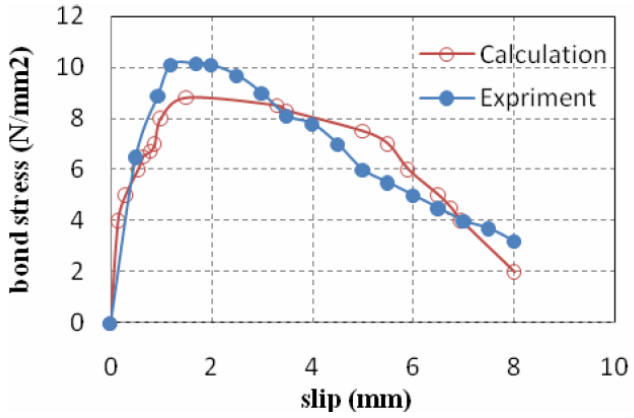

Figure 17: Pull-out test experiment vs FEA of a Ø12mm steel bar with ribs

Note: The experiment was performed by Lettow, Mayer, and Eligehausen (2003) and the finite element analysis by Shafaei, Hosseini, and Marefat (2009).

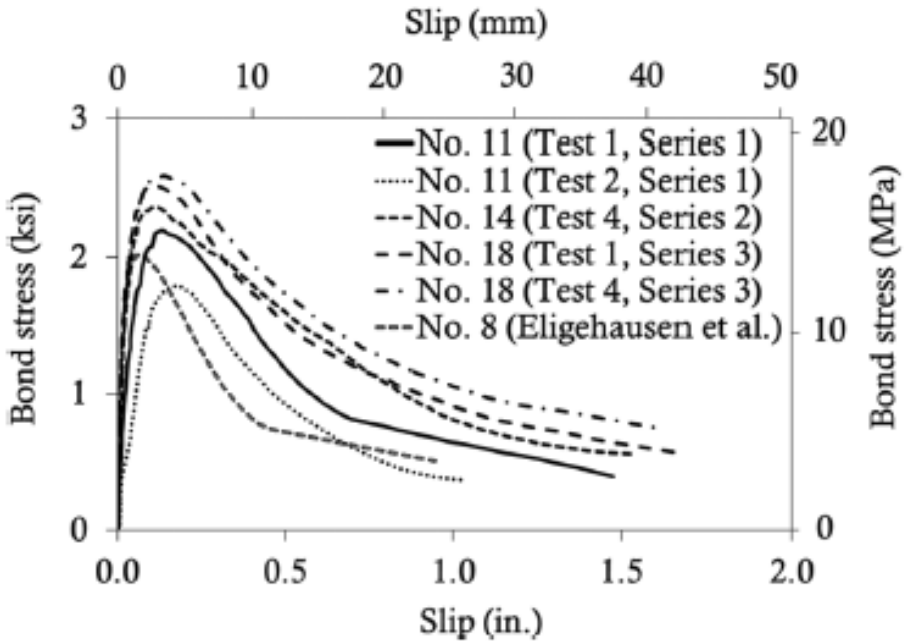

Figure 18: Pull-out test experimental results

Note: Murcia-Delso, Stavridis, and Shing (2013) in Series 1 to 3, which had concrete strengths of approximately 5 ksi (34.5 MPa) vs the curve obtained by Eligehausen, Popov, and Bertero (1982) for a No. 8 (25 mm) bar and 4.35 ksi (30 MPa) concrete.

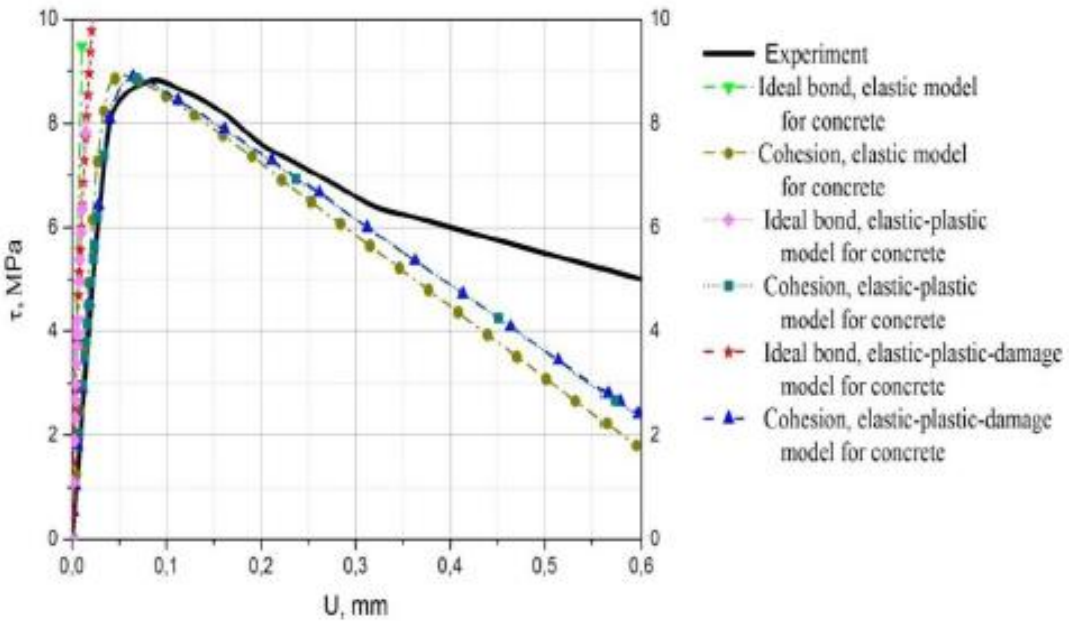

Figure 19: Pull-out test experiment vs FEA

Note: Experiment performed by Beliaev et al. (2016) using 14mm diameter bars vs finite element model using different bond characteristics.

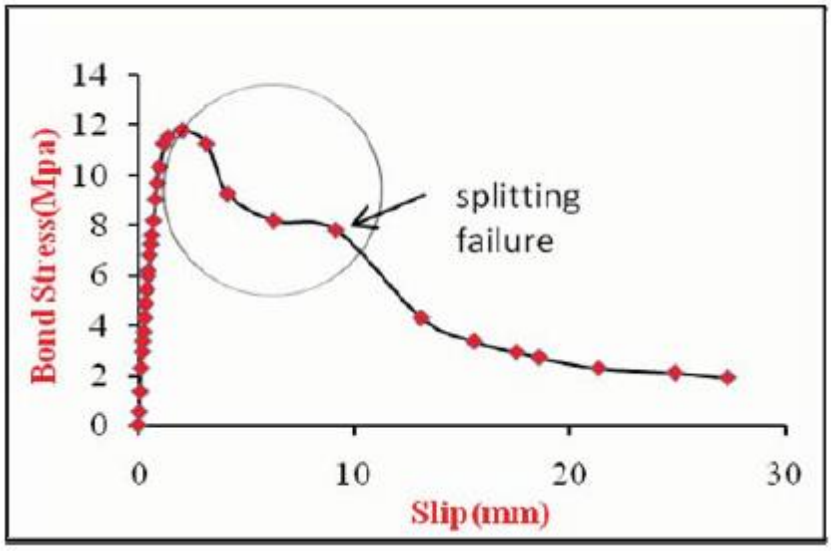

Figure 20: Bond stress-slip relationship of 10mm deformed bar (fcu=27MPa)

Source: Sahi, Al-Zuhairi, and Al-Fatlawi (2009)

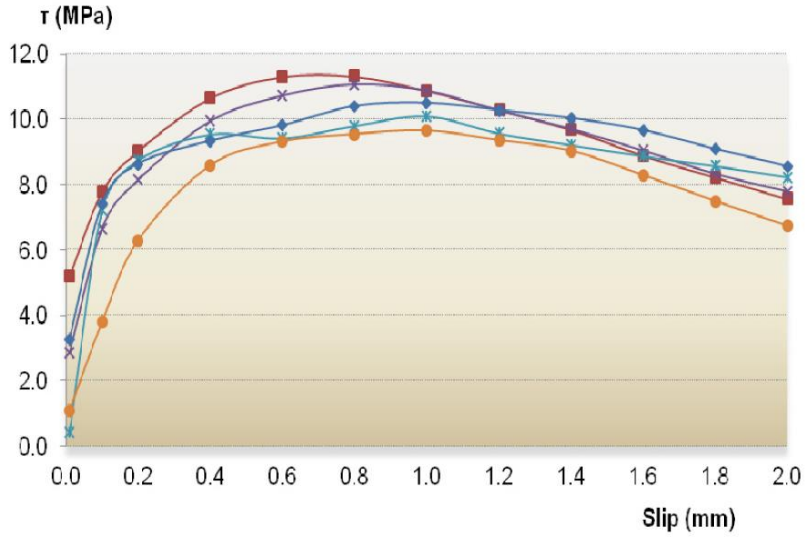

Figure 21: Bond stress-slip10.0mm diameter ribbed bars in 25MPa concrete

Source: Carvalho et al. (2017)

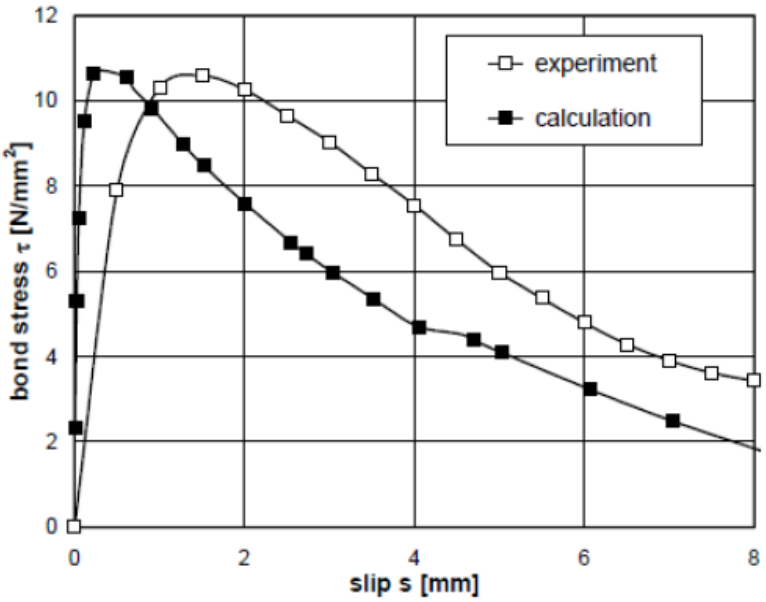

Figure 22: Pull-out experiment vs numerical analysis

Note: The experiment was done by Lettow, Mayer, and Eligehausen (2003) and the numerical simulation for bond stress and hoop stress was done by Bulck (2015).

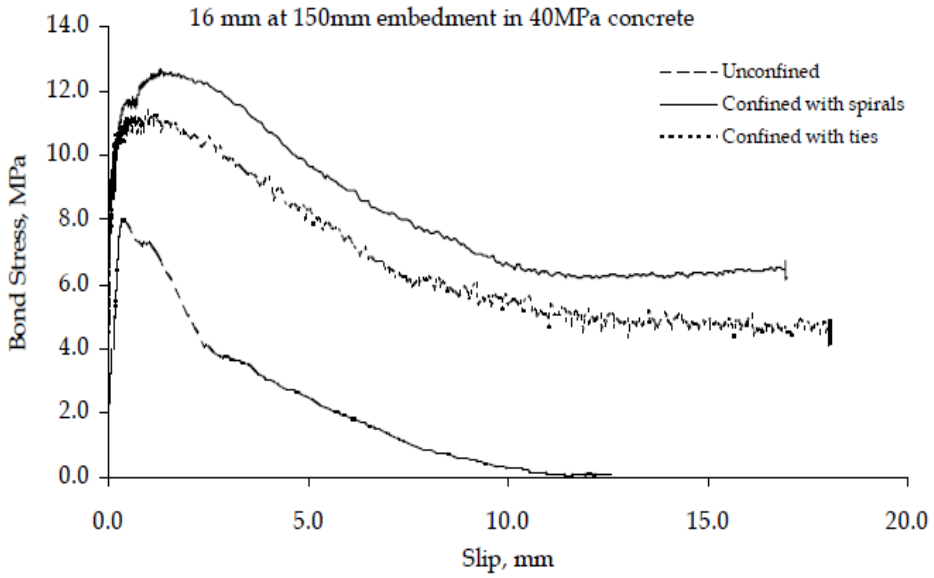

Figure 23: Bond stress vs slip with 16mm bars at 150mm embedment

Source: Gangolu et al. (2007)

2.7 Finite Element / Material Modeling

2.7.1 Concrete Damaged Plasticity Model

ABAQUS software (SIMULIA, 2013) has the capability to simulate concrete damage using three types of crack models for reinforced concrete. (1) The Smeared Crack Concrete Model, (2) The Brittle Crack Concrete Model, and (3) Concrete Damaged Plasticity Model.

The smeared cracking model is more suitable for monotonic loading under low confining pressures and the brittle cracking model is more suitable in applications that are dominated by tensile cracking as it assumes linear elastic behaviour in compression. The Concrete Damaged Plasticity Model would be the preferred model in this study because it is the most advanced of the three models as it is capable of simulating the complete behaviour of the concrete in both tension and compression as well as damage characteristics under static/dynamic and cyclic/monotonic loading.

According to Beliaev et al. (2016), an elastic-plastic damage model can be used to capture the degradation of elastic stiffness in the concrete as well as irreversible deformations upon mechanical loading. This requires elastic-plastic constitutive equations to be combined with continuum damage mechanics to describe the mechanical behaviour of the concrete upon loading. The elastic-plastic concrete behaviour can be coupled with Damage by defining damage growth as a function of accumulated plastic strains (Lubliner et al. 1989). The extension and propagation of micro cracks contributes significantly to the concrete inelastic behaviour due to the role it plays in degrading the concrete's elastic stiffness. This phenomenon is modeled using a single-scalar damage variable. The damage variable ranges from 0 for the undamaged material to 1 for completely damaged material. The constitutive equation of elastic-plastic material with scalar isotropic damage was introduced by Kachanov (1999) and further developed by Rabotnov, Leckie, and Prager (1970) and others and it takes the following form:

$$\boldsymbol{\sigma} = (\mathbf{1}-\mathbf{D}) \cdot {}^{4}\mathbf{C}_{\mathbf{0}}{}^{e} \cdot\cdot (\boldsymbol{\varepsilon} - \boldsymbol{\varepsilon}^{p}) = {}^{4}\mathbf{C}_{\mathbf{0}}{}^{e} \cdot\cdot (\boldsymbol{\varepsilon} - \boldsymbol{\varepsilon}^{p}) \qquad (1)$$

where $\boldsymbol{\sigma}$ is Cauchy stress tensor, D is the scalar stiffness degradation variable, $\boldsymbol{\varepsilon}$ is the strain tensor, $\boldsymbol{\varepsilon}^{p}$ is the plastic strain tensor, ${}^{4}\mathbf{C}_{\mathbf{0}}{}^{e}$ the initial (undamaged) elastic stiffness of the material, while ${}^{4}\mathbf{C}^{e} = (\mathbf{1}-\mathbf{D}) \cdot {}^{4}\mathbf{C}_{\mathbf{0}}{}^{e}$ is the degraded elastic stiffness tensor. The effective stress tensor is defined by the relation $\bar{\boldsymbol{\sigma}} = {}^{4}\mathbf{C}_{\mathbf{0}}{}^{e} \cdot\cdot (\boldsymbol{\varepsilon} - \boldsymbol{\varepsilon}^{p}) = \boldsymbol{\sigma}/(\mathbf{1}-\mathbf{D})$

The evolution of the scalar degradation variable is defined by the function $D=D(\bar{\boldsymbol{\sigma}}, \tilde{\boldsymbol{\varepsilon}}^{p})$ governed by a set of the effective stress tensor $\bar{\boldsymbol{\sigma}}$ and hardening (softening) variables $\tilde{\boldsymbol{\varepsilon}}^{p}$. In the Lubliner model (Lubliner et al. 1989), the stiffness degradation is initially isotropic and defined by degradation variable D_c in a compression zone and variable D_t in a tension zone. The cracking (under tension) and the crushing (under compression) in concrete are represented by increasing values of the hardening (softening) variables. These variables control the evolution of the yield surface and the degradation of the elastic stiffness. The

yield function represents a surface in effective stress space F ($\bar{\boldsymbol{\sigma}}$, $\tilde{\boldsymbol{\varepsilon}}^{p}$) $\leq$ 0 which determines the states of failure or damage.

Plastic flow is governed by a flow potential function G ($\bar{\boldsymbol{\sigma}}$) according to the non-associative flow rule:

$$\dot{\varepsilon}^{p} = \dot{\lambda}\, \frac{\partial G(\bar{\boldsymbol{\sigma}})}{\partial \bar{\sigma}} \tag{2}$$

As validated by Jankowiak and Lodygowski (2005), the flow potential *G* and yield function F are accepted in the forms:

$$G = \sqrt{(F_c - m.f_t.tan\beta)^2 + 3\bar{J}_2} + \frac{1}{3}\bar{I}_1.tanB \tag{3}$$

$$F = \frac{1}{1-\alpha}\left(\sqrt{3J_2} + \alpha\,.I_1 + \theta(\bar{\varepsilon}^{P})\langle\bar{\sigma}_{max}\rangle - \gamma\langle-\bar{\sigma}_{max}\rangle\right) - \bar{\sigma}_c(\tilde{\varepsilon}_c{}^{P}) \tag{4}$$

where f_t and f_c are the uniaxial tensile and compressive strengths of concrete, respectively, β is the dilation angle measured in the $\frac{1}{3}\bar{I}_1 - \sqrt{3\bar{J}_2}$ plane at high confining pressure, while *m* is an eccentricity of the plastic potential surface, $\bar{I}_1 = 1 \cdot\cdot\, \bar{\sigma}$ and $\bar{J}_2 = \frac{1}{2}\, dev\, \bar{\sigma} \cdot\cdot\, dev\bar{\sigma}$

2.7.2 Uniaxial Tension and Compression Stress Behaviour

According to the Abaqus Documentation (2017a), the damaged plasticity model is a continuum, plasticity-based, damage model for concrete. It assumes that the main two failure mechanisms are tensile cracking and compressive crushing of the concrete material. The two hardening variables, ε_t^{pl} and ε_c^{pl}, controls the evolution of the yield or failure surface. They are linked to failure mechanisms under tension and compression loading and are referred to as tensile and compressive equivalent plastic strains.

Figure 24 and figure 25 below shows the uniaxial tensile and compressive responses of concrete for the model which is characterized by damaged plasticity.

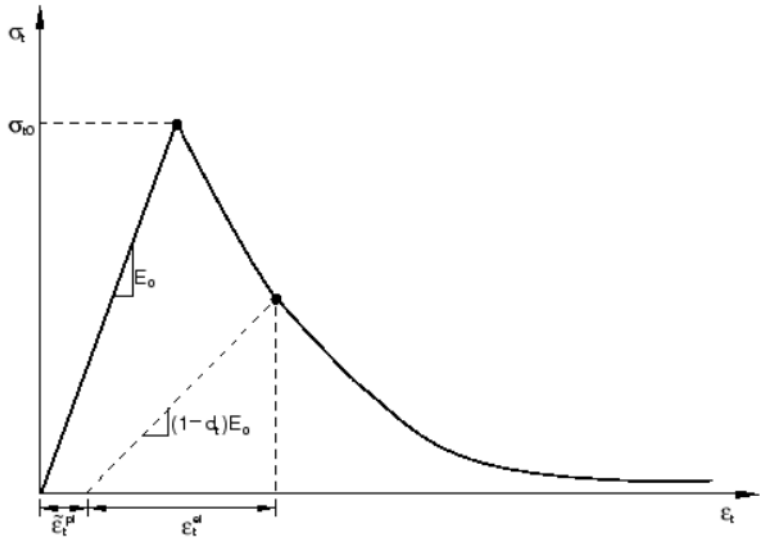

Figure 24: Uniaxial tension curve for concrete

Source: Abaqus Documentation (2017a)

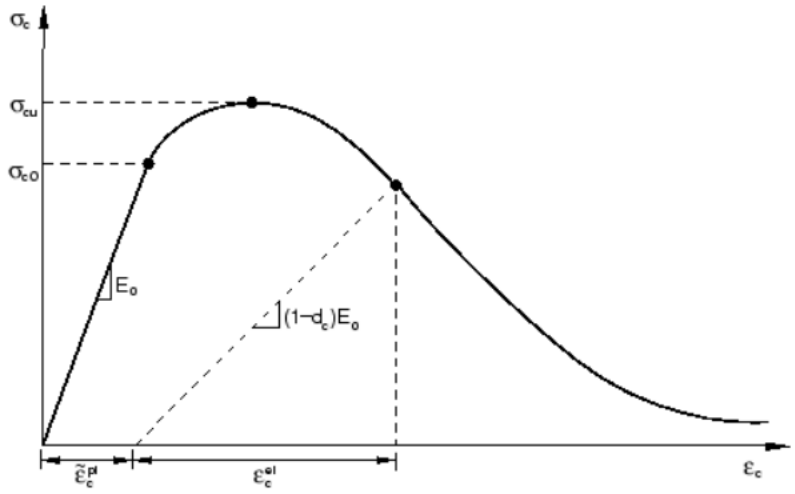

Figure 25: Uniaxial compression curve for concrete

Source: Abaqus Documentation (2017a)

Figure 24 above shows the stress-strain curve subjected to uniaxial tension loads, the response is linear and elastic up to the failure stress $\sigma_{t0.}$ The failure stress corresponds to the development of microcracks in the concrete. The micro cracks widen and propagate throughout the concrete and this is represented by the softening branch of the curve which introduces strain localization in the concrete.

Figure 25 above shows stress-strain curve subjected to uniaxial compression loads, the response is linear and elastic up to the failure stress $\sigma_{c0.}$ Beyond this stress, is the plastic regime where the concrete experiences stress hardening and when the ultimate stress, σ_{cu} is reached, the concrete experiences strain hardening.

The uniaxial stress-strain curves can be converted into stress versus plastic-strain curves using the following expressions.

$$\sigma_t = \sigma_t\left(\varepsilon_t^{pl}, \dot{\varepsilon}_t^{pl}, \theta, f_i\right), \tag{5}$$

$$\sigma_c = \sigma_c\left(\varepsilon_c^{pl}, \dot{\varepsilon}_c^{pl}, \theta, f_i\right), \tag{6}$$

where the subscripts t and c refer to tension and compression, respectively; ε_t^{pl} and ε_c^{pl} are the equivalent plastic strains, $\dot{\varepsilon}_t^{pl}$and $\dot{\varepsilon}_c^{pl}$ are the equivalent plastic strain rates, θ is the temperature, and *fi*, (i=1,2,…) are other predefined field variables.

As shown in figure 24 and figure 25, when there is unloading of the concrete from any point on the strain softening branch of the curves, the unloading response is weaker or less stiff that the original loading response. This is representative of damage or degradation in the elastic stiffness of the concrete and is characterized by the damage variables dt and dc which are functions of the plastic strain, temperature, and field variables:

$$d_t = d_t\left(\varepsilon_t^{pl}, \theta, f_i\right), \qquad 0 \le d_t \le 1 \tag{7}$$

$$d_c = d_c\left(\varepsilon_c^{pl}, \theta, f_i\right), \qquad 0 \le d_c \le 1 \tag{8}$$

The damage variables range from 0 to 1 where 0 represents the undamaged concrete and 1 represents the full damaged concrete with total loss of strength. If E_0 is the initial (undamaged) elastic stiffness of the material, the stress-strain relations under uniaxial tension and compression loading are, respectively:

$$\sigma_t = (1 - d_t)\, E_0\left(\varepsilon_t - \varepsilon_t^{pl}\right) \tag{9}$$

$$\sigma_c = (1 - d_c)\, E_0\left(\varepsilon_c - \varepsilon_c^{pl}\right) \tag{10}$$

The effective tensile and compressive cohesive stresses are defined as:

$$\bar{\sigma_t} = \frac{\sigma_c}{(1-d_t)}\, E_0\left(\varepsilon_t - \varepsilon_t^{pl}\right) \tag{11}$$

$$\bar{\sigma_c} = \frac{\sigma_c}{(1-d_c)} E_0\left(\varepsilon_c - \varepsilon_c^{pl}\right) \tag{12}$$

The effective cohesion stresses determine the size of the yield (or failure) surface.

2.7.3 Uniaxial Cyclic Behaviour

According to Abaqus Documentation (2017a), when a concrete member is subjected to uniaxial cyclic loads the degradation behaviour is a little more complex and involved, compared with uniaxial static loading. It involves the opening and closing of previously formed cracks during subsequent cycles. Previous researchers have found through experimentation that there is some recovery of elastic stiffness as the load changes sign particularly from tension to compression which causes cracks to close. The stiffness recovery effect is known as the unilateral effect.

The concrete damaged plasticity model assumes that the reduction of the elastic modulus is given in terms of a scalar degradation variable d as

$$E=(1-d)E_0 \tag{13}$$

where E_0 is the initial (undamaged) modulus of elasticity of the material.

The above expression is valid for both the tension and compressions sides of the cycle. The stiffness degradation variable, *d*, is a function of the stress state and the uniaxial damage variables, d_t and d_c under the following relationship:

$$(1-d) = (1-s_t d_c)(1-s_c d_t), \tag{14}$$

where

s_t and s_c are functions of the stress state that are introduced to model stiffness recovery effects associated with stress reversals. They are defined according as:

$$s_t=1-w_t\, r^*(\sigma_{11}) \; ; \; 0\leq w_t \leq 1 \tag{15}$$

$$s_c=1-w_c\,(1-r*(\sigma_{11})) \; ; \; 0\leq w_c \leq 1 \tag{16}$$

where

$$r^*(\sigma_{11}) = H(\sigma_{11}) = \begin{cases} 1 \; if \; \sigma_{11} > 0 \\ 0 \; if \; \sigma_{11} < 0 \end{cases} \tag{17}$$

The weight factors w_t and w_c are considered as material properties and control the recovery of stiffness upon load reversal. This is illustrated in Figure 26 below, where the load changes from tension to compression.

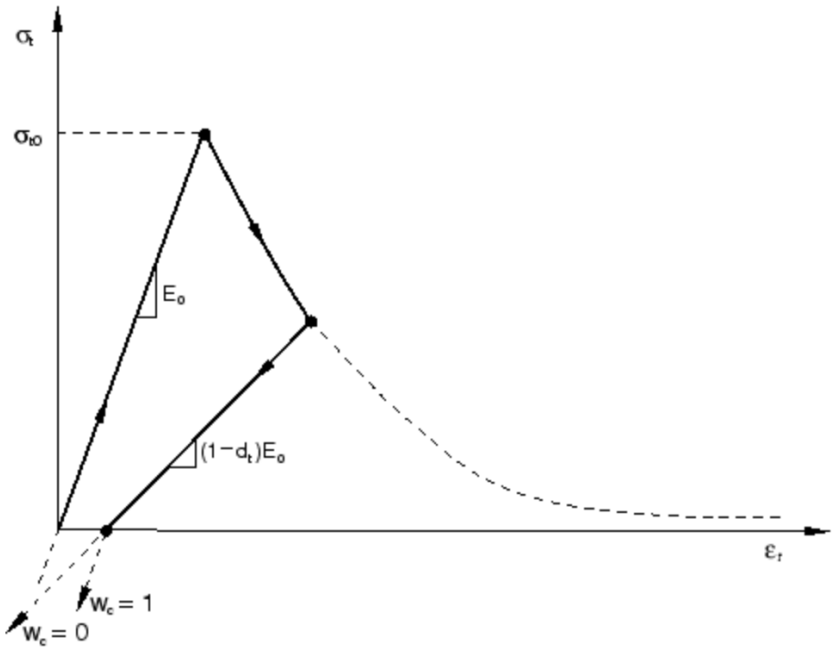

Figure 26: Illustration of the compression stiffness recovery parameter w_c

Source: Abaqus Documentation (2017a)

If we assume that the concrete had no previous compressions damage then:

$$\varepsilon_c^{pl}=0 \text{ and } d_c=0. \tag{18}$$

so

$$(1-d)=(1-s_c d_t)=(1-(1-w_c(1-r*))d_t) \tag{19}$$

In tension ($\sigma_{11}>0$), $r*= 1$; therefore, $d=d_t$ as expected.

In compression ($\sigma_{11}<0$), $r*=0$, and $d=(1-w_c)\, d_t$. If $w_c=1$, then $d=0$; therefore, the material fully recovers the compressive stiffness (which in this case is the initial undamaged stiffness, $E=E_0$). If, on the other hand, $w_c=0$, then $d=d_t$ and there is no stiffness recovery. Intermediate values of w_c result in partial recovery of the stiffness.

2.7.4 Tension Stiffening

According to Abaqus Documentation (2017a), the post failure behaviour for concrete in tension can be modeled in Abaqus using tension stiffening properties. These properties define the strain softening and cracked behaviour of concrete. It also allows the modeling of the reinforcement of cracked concrete. In Abaqus, tension stiffening can be specified by means of a post failure stress-strain relation or by a fracture energy cracking criterion.

Post failure behaviour in reinforced concrete is defined by specifying post failure stress as a function of cracking, ε_t^{ck}. The cracking strain is the total strain minus the elastic strain corresponding to the undamaged material; that is, $\varepsilon_t^{ck}=\varepsilon_t$ - ε_{0t}^{el} , where $\varepsilon_{0t}^{el}=\sigma_t/E^0$, as illustrated in figure 27 below.

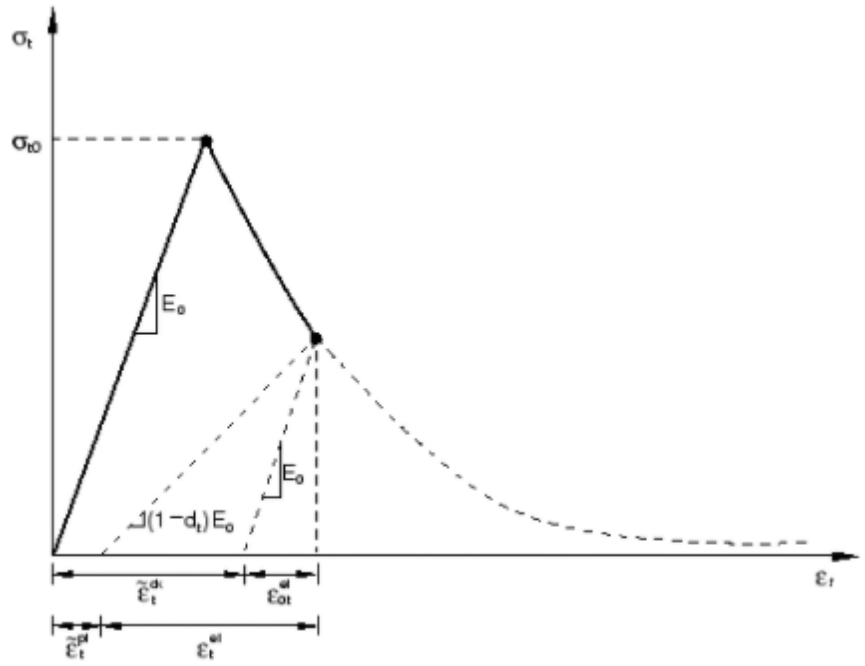

Figure 27: Illustration of cracking strain ε_t^{ck} used for the tension stiffening data

Source: Abaqus Documentation (2017a)

Abaqus automatically converts the cracking strain values provided to plastic strain using the relationship below,

$$\varepsilon_t^{pl} = \varepsilon_t^{ck} - \frac{d_t}{(1-d_t)}\frac{\sigma_t}{E_o} \tag{20}$$

2.7.5 Compression Behaviour

According to Abaqus Documentation (2017a)**,** in order to define the behaviour of plain concrete under compression outside of the elastic regime, data is provided in the form of stress and inelastic or crushing strain ε_c^{in} . The stress-strain curve can be extended beyond the ultimate stress into the strain-softening regime.

Hardening data can also be given in terms of the inelastic strain, ε_c^{in}. The compressive inelastic strain is defined as the total strain minus the elastic strain corresponding to the undamaged material, $\varepsilon_c^{in} = \varepsilon_c - \epsilon_{0c}^{el}$, where ε_{0c}^{el}=σ_c/E^0, as illustrated in figure 28.

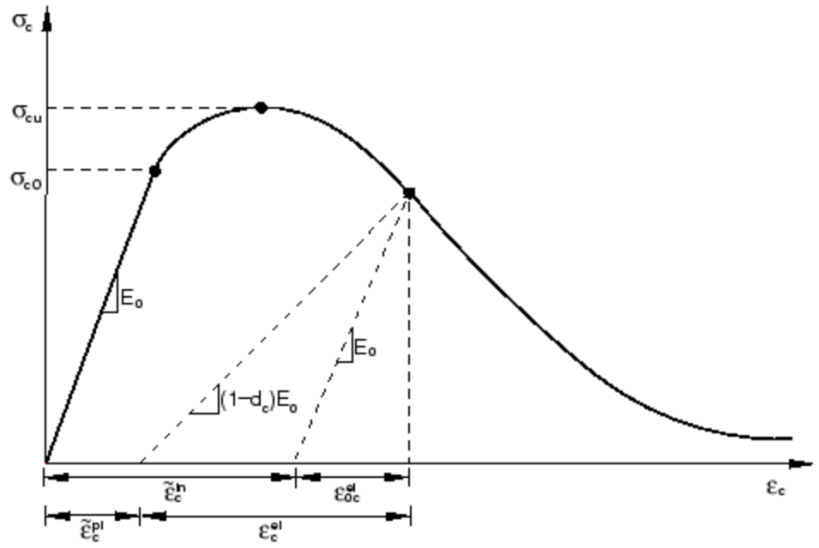

Figure 28: Definition of compressive inelastic (or crushing) strain ε_c^{in}

Source: Abaqus Documentation (2017a)

Abaqus automatically converts the inelastic strain values to plastic strain values using the following relationship,

$$\varepsilon_c^{pl} = \varepsilon_c^{in} - \frac{d_c}{(1-d_c)}\frac{\sigma_c}{E_o} \tag{21}$$

2.7.6 Plastic Flow

According to Abaqus Documentation (2017a)**,** non-associated potential plastic flow is assumed for the concrete damaged plasticity model. The flow potential G used for this model is the Drucker-Prager hyperbolic function:

$$G = \sqrt{(\epsilon\sigma_{t0}tan\psi)^2 + \bar{q}^2} - \bar{p}\,tan\psi, \tag{22}$$

Where

$\psi(\phi, f_i)$ is the dilation angle in the p–q plane at high confining pressure;

$\sigma_{t0}(\phi, f_i) = \sigma_t|\varepsilon_t^{pl} = 0, \dot{\varepsilon}_t^{pl}$ is the uniaxial tensile stress at failure, taken from the user-specified tension stiffening data; and

$\epsilon(\phi, f_i)$ is a parameter, referred to as the eccentricity, that defines the rate at which the function approaches the asymptote (the flow potential tends to a straight line as the eccentricity tends to zero).

This flow potential, which is continuous and smooth, ensures that the flow direction is always uniquely defined. The function approaches the linear Drucker-Prager flow potential asymptotically at high confining pressure stress and intersects the hydrostatic pressure axis at 90°.

In Abaqus, the default flow potential eccentricity is ϵ=0.1, which implies that the material has almost the same dilation angle over a wide range of confining pressure stress values. Increasing the value of ϵ provides more curvature to the flow potential, implying that the dilation angle increases more rapidly as the confining pressure decreases. Values of ϵ that are significantly less than the default value may lead to convergence problems if the material is subjected to low

confining pressures because of the very tight curvature of the flow potential locally where it intersects the p-axis.

2.7.7 Yield Function

According to Abaqus Documentation (2017a)**,** the model makes use of the yield function of Lubliner et al. (1989), with the modifications proposed by Lee and Fenves (1998) to account for different evolution of strength under tension and compression. The evolution of the yield surface is controlled by the hardening variables, ε_t^{pl} and ε_c^{pl}. In terms of effective stresses, the yield function takes the form,

$$F = \frac{1}{1-\alpha}\left(\bar{q} - 3\alpha\bar{p} + \beta(\varepsilon^{pl})\,\langle\hat{\bar{\sigma}}_{max}\rangle - \gamma\langle\hat{\bar{\sigma}}_{max}\rangle\right) - \bar{\sigma}_c(\varepsilon^{pl}) = 0 \tag{23}$$

With

$$\alpha = \frac{\frac{\sigma_{b0}}{\sigma_{co}}-1}{2\frac{\sigma_{b0}}{\sigma_{co}}-1}; 0 \le \alpha \le 0.5, \tag{23.1}$$

$$\beta = \frac{\bar{\sigma}_c(\varepsilon^{pl})}{\bar{\sigma}_t(\varepsilon^{pl})}(1-\alpha) - (1+\alpha); 0, \tag{23.2}$$

$$\gamma = \frac{3(1-k_c)}{2k_c-1}. \tag{23.3}$$

Here,

$\hat{\bar{\sigma}}_{max}$ is the maximum principal effective stress;

$\frac{\sigma_{b0}}{\sigma_{co}}$ is the ratio of initial equibiaxial compressive yield stress to initial uniaxial compressive yield stress (the default value is 1.16);

$\bar{\sigma}_t(\varepsilon^{pl})$ is the effective tensile cohesion stress; and

$\bar{\sigma}_c(\varepsilon^{pl})$ is the effective compressive cohesion stress.

2.7.8 Interface Modeling

According to Abaqus Documentation (2017b), cohesive behaviour is modeled to represent destroying of the reinforced-concrete bond. A traction-separation model is utilized and this initially assumes linear elastic behaviour followed by the initiation and evolution of bond damage. The elastic behaviour is presented in the form of an elastic constitutive matrix that relates the nominal stresses to the nominal strains across the interface. The nominal stresses are the force components divided by the original area at each integration point and the nominal strains are the separations divided by the original thickness at each integration point.

The nominal traction stress vector consists of three components: t_n, t_s and t_t , which represent the normal and the two shear tractions respectively. The corresponding separations are denoted by δn, δs and δt. The elastic behaviour is represented by the following equation:

$$\begin{pmatrix} t_n \\ t_s \\ t_t \end{pmatrix} = \begin{bmatrix} Knn & Kns & Knt \\ Kns & Kss & Kst \\ knt & kst & ktt \end{bmatrix} \begin{pmatrix} \delta n \\ \delta s \\ \delta t \end{pmatrix} \tag{24}$$

Modeling the bond damage allows for the simulation of the degradation and eventual failure of the bond between the concrete body and steel rebar. The failure mechanism consists of a damage initiation criterion and a damage evolution law.

The bond damage initiation refers to the beginning of degradation of the cohesive response at a contact point. The process of degradation begins when the contact stresses and/or contact separations satisfy certain damage initiation criteria as shown below.

Maximum nominal stress criterion: the bond damage is assumed to initiate when the maximum contact stress ratio (as defined in the expression below) reaches a value of one. This criterion can be represented as:

$$\max\left\{\frac{\langle t_n \rangle}{{t^0}_n}, \frac{t_s}{{t^0}_s}, \frac{t_t}{{t^0}_t}\right\} = 1 \tag{25}$$

Maximum nominal separation criterion: the bond damage is assumed to initiate when the maximum separation ratio (as defined in the expression below) reaches a value of one. This criterion can be represented as:

$$\max\left\{\frac{\langle \delta_n \rangle}{{\delta^0}_n}, \frac{\delta_s}{{\delta^0}_s}, \frac{\delta_t}{{\delta^0}_t}\right\} = 1 \tag{26}$$

Quadratic nominal stress criterion: Damage is assumed to initiate when a quadratic interaction function involving the nominal stress ratios (as defined in the expression below) reaches a value of one. This criterion can be represented as:

$$\left\{\frac{\langle t_n \rangle}{{t^0}_n}\right\}^2 + \left\{\frac{t_s}{{t^0}_s}\right\}^2 + \left\{\frac{t_t}{{t^0}_t}\right\}^2 = 1 \tag{27}$$

Quadratic nominal strain criterion: Damage is assumed to initiate when a quadratic interaction function involving the nominal strain ratios (as defined in the expression below) reaches a value of one. This criterion can be represented as:

$$\left\{\frac{\langle \delta_n \rangle}{{\delta^0}_n}\right\}^2 + \left\{\frac{\delta_s}{{\delta^0}_s}\right\}^2 + \left\{\frac{\delta_t}{{\delta^0}_t}\right\}^2 = 1 \tag{28}$$

Figure 29 below shows a typical traction separation response with a failure mechanism.

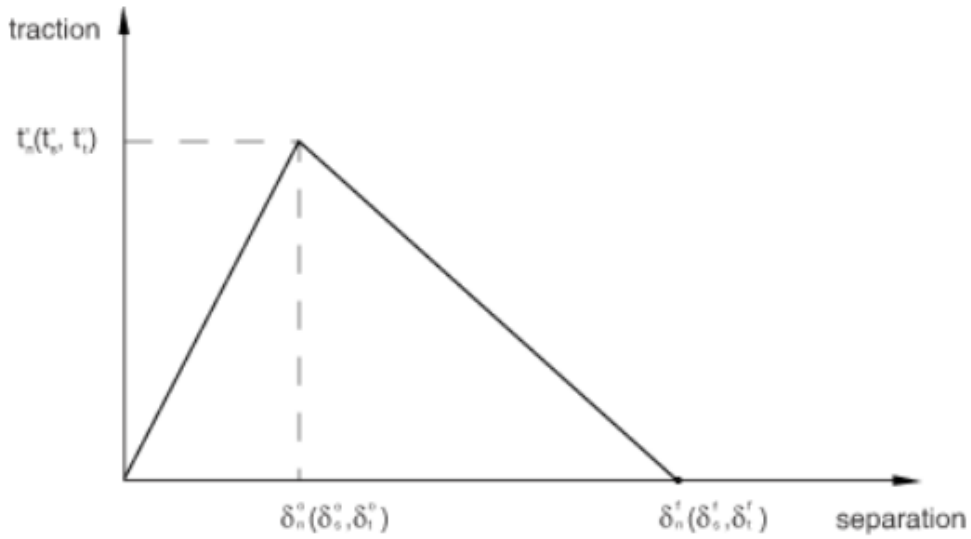

Figure 29: Typical traction-separation response

Source: Abaqus Documentation (2017b)

The bond damage evolution law describes the rate at which the cohesive stiffness is degraded once the corresponding initiation criterion is reached.

A scalar bond damage variable, Db, represents the overall damage at the contact point. It initially has a value of 0. If damage evolution is modelled, Db monotonically increases from 0 to 1 upon further loading after the initiation of damage. The contact stress components are affected by the damage according to

$$tn = \begin{cases} (1 - Db)\bar{t_n}\,, & t_n > 0 \\ \bar{t}_n\,, & t_n \leq 0 \end{cases}, \tag{29}$$

$$t_s = (1 - Db)\bar{t_s}, \tag{29.1}$$

$$t_t = (1 - Db)\bar{t_t}, \tag{29.2}$$

where

t_n, t_s and t_t are the contact stress components predicted by the elastic traction separation behaviour for the current separations without damage.

To describe the evolution of bond damage under a combination of normal and shear separations across the interface, it is useful to introduce an effective separation (Camanho and Dávila 2002) defined as

$$\delta_m = \sqrt{\langle \delta_n \rangle^2 + {\delta_s}^2 + {\delta_t}^2} \tag{30}$$

An evolution of the bond damage variable Db was used for exponential softening, that reduces (in the case of damage evolution under a constant mode mix, temperature, and field variables) to

$$Db = 1 - \left\{\frac{{\delta_m}^0}{\delta_m^{max}}\right\}\left\{1 - \frac{1-exp\left(-\alpha\left(\frac{\delta_m^{max}-{\delta_m}^0}{{\delta^f}_m-{\delta^0}_m}\right)\right)}{1-\exp(-\alpha)}\right\} \tag{31}$$

In the expression above α is a non-dimensional parameter that defines the rate of damage evolution.

CHAPTER 3

METHODOLOGY

A finite element analysis study was performed using ABAQUS software Version 13.1, to investigate various versions of non-coded connections commonly used in local residential construction. Before setting up the final test models, the loading criteria was established based on the wind loads that are expected to be experienced by a typical structure in this region.

A pull-out test model was first developed to calibrate the parameters of the bond slip model for the embedment of a mild steel rebar in concrete. The model was subjected to a mesh convergence study to ensure that the results were independent of the chosen mesh size. With the final selected mesh size, the model was analysed and the bond slip interaction model was calibrated against the pull-out test results of a previous experiment done by another researcher.

Models of the various versions of the non-coded connections were then developed using the parameters established from the pull-out calibration model. A mesh convergence study was conducted on these models using various mesh sizes to ensure that the results were again independent of the chosen mesh size. With the final selected mesh size, the models were set up for final analysis. An upward displacement was applied to each rafter and the resultant forces, stresses in the steel connecting elements, stresses & damage in the concrete and stresses at the concrete-steel interface was examined. A pull-out test was then performed on the models using varying embedment depths to determine that minimum effective rebar embedment depth that will preclude pull-out failure. The rebar diameter was also varied to determine the effects of varying the rebar diameter on the pull-out capacity.

The following are the details of all the steps undertaken:

3.1 Calculation of Wind Loads

Wind loads were calculated based on the procedures of chapter 6 of the ASCE 7 code. The inputs for this calculation are as follows:

3.1.1 Calculation of **Velocity Pressure, V_h** using the following inputs:

I, importance factor (1 for category 2)

V, wind speed (117mph)

Kz, velocity pressure exposure coefficient (1,2&3 story building with roof apex 6m,9m and 12m above ground)

Kzt, topographic factor (using worst case factor of 1)

Kd, wind directionality factor (0.85 for main wind force resisting system)

3.1.2 Calculation of **Design Pressure, P_h** using the following additional inputs:

G, gust effect factor (0.85 for rigid structures)

Cp, external pressure coefficients (using worst case factor of 1.3 for a low pitch roof i.e. < 10 degrees)

3.1.3 Calculation of **Connection Load, F**

The design wind pressure was applied to the tributary area of the rafter using various rafter spacings ranging from 3m to 6m and various rafter spans ranging from 6m to 12m. The resulting uniformly distributed wind load on the rafter was then projected to the connection joint to represent the connection load. A summarized table was then produced displaying the connection load for each combination of rafter spacing and rafter span.

3.2 Pull-out Test Calibration/Verification Model

The pull-out test model was set up to mimic the results of a past experiment conducted in accordance with RILEM/CEB/FIB requirements. The results of this experiment was presented in the journal paper titled “Simulation of

Pulling the Reinforcing Bar from Concrete Block with Account of Friction and Concrete Damage" by Mikhail Beliaev**,** Artem Semenov, Sergey Semenov, and Andrey Benin. The model was set up with the geometric parameters shown below in figure 30and loading conditions shown in figure 31.

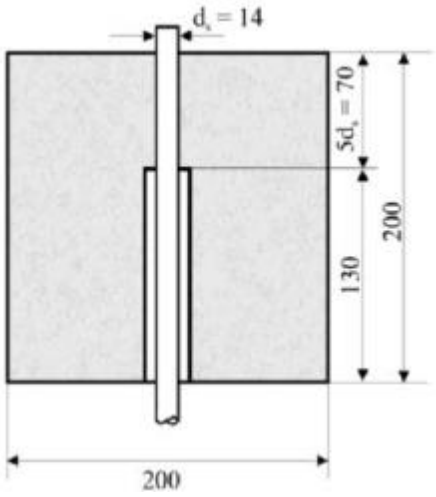

Figure 30: Geometric parameters of concrete block with steel anchor

Source: (Beliaev et al. 2016)

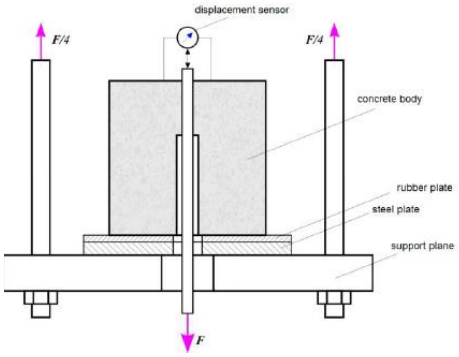

Figure 31: Loading Conditions for Experiment

Source: (Beliaev et al. 2016)

The test was conducted on tensile tester Shimadzu AG-300kN. Steel reinforcement 14mm diameter and B25 concrete was used in the experiment.

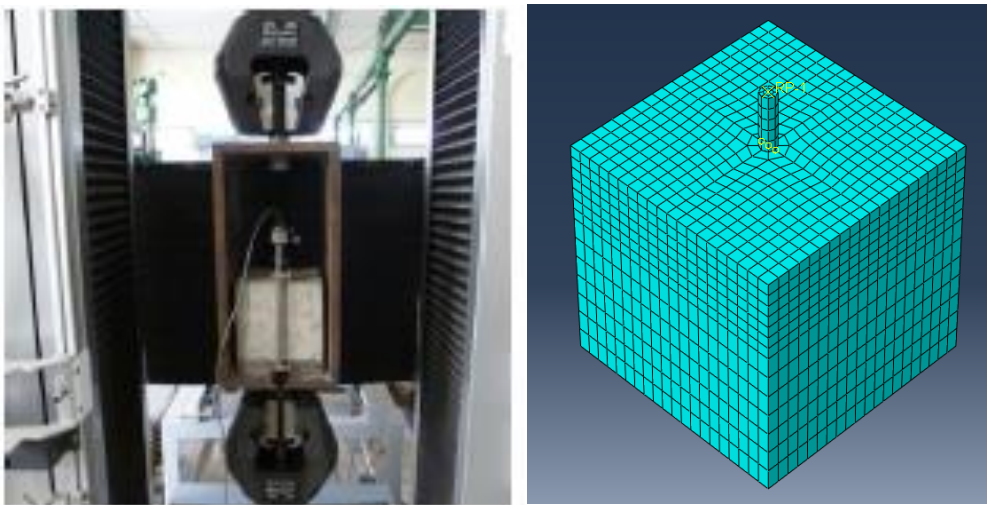

(a) (b)

Figure 32: Pull-out test setup apparatus vs FEA model

Note:(a) Tensile tester Shimadzu AG-300kN; (b) 3D FE model to mimic experiment.

3.2.1 Material Model

Concrete Model:

Density=$2.4x10^{-9}$ tonnes/mm^3

Compressive strength=20MPa Cylinder or 25MPa Cube

Young's Modulus=30,000 MPa

Poisons' Ratio=0.2

Concrete Damage Plasticity Model:

Table 1 below shows the physical properties of the damaged plasticity model developed by Jankowiak and Lodygowski (2005) as cited in and cited Claudio Amadio, Nader Akkad, and Marco Fasan (2015) for the grade of concrete used i.e.C20/25.

Table 1: Concrete damage plasticity model for the calibration experiment

Material's parameters				Compression behaviour				Tension behaviour			
Elasticity		*Plasticity*		*Yield Stress (MPa)*	*Inelastic Strain*	*Damage Parameter*	*Inelastic Strain*	*Yield Stress (MPa)*	*Cracking Strain*	*Damage Parameter*	*Inelastic Strain*
Class	20/25	Dilation Angle	38°	11.2	0	0	0	2.9	0	0	0
E[GPa]	30	Eccentricity	0.1	18	0.0007	0	7.50E-05	1.6	0.00015	0	3.30E-05
v	0.2	fb_0/fc_0	1.12	21	0.001	0	9.90E-05	0.75	0.00035	0.4064	1.60E-04
		K	0.666	26	0.002	0	1.54E-04	0.25	0.0006	0.6964	2.80E-04
		Viscosity	0.002	20.5	0.0034	0	7.62E-04				
				13	0.005	0.1954	2.56E-03				
						0.5964	5.68E-03				
						0.8949	1.17E-02				

Steel Rebar Model:

Density= 7.8×10^{-9} tonnes/mm^3

Young's Modulus=206,000 MPa

Poisons' Ratio=0.3

Yield Stress=235MPa

3.2.2 Analysis Step

Type=Static General

Time Period=1

Maximum number of increments= 100000

Increment size= initial (0.01) minimum (1E-20) maximum (0.1)

Field output= Contact shear stress (CSHEAR2-frictional shear stress),

History output=Displacement (U2-displacement)

3.2.3 Interaction Model

Interaction type=surface to surface contact

Master surface=embedded rebar surface

Slave surface=concrete hole surface

Sliding formulation=small sliding

Contact property=cohesive contact

Tangential behaviour, friction coefficient=0.5

Cohesive behaviour, knn=1500 MPa/mm kss=360 MPa/mm ktt=360 MPa/mm

Damage initiation (maximum normal stress):

normal direction=110MPa

shear direction-1=9MPa

shear direction-2=9MPa

Damage evolution:

Type=displacement

Softening=linear

Total Plastic Displacement=1mm

Damage stabilization:

Viscosity coefficients=0.0005

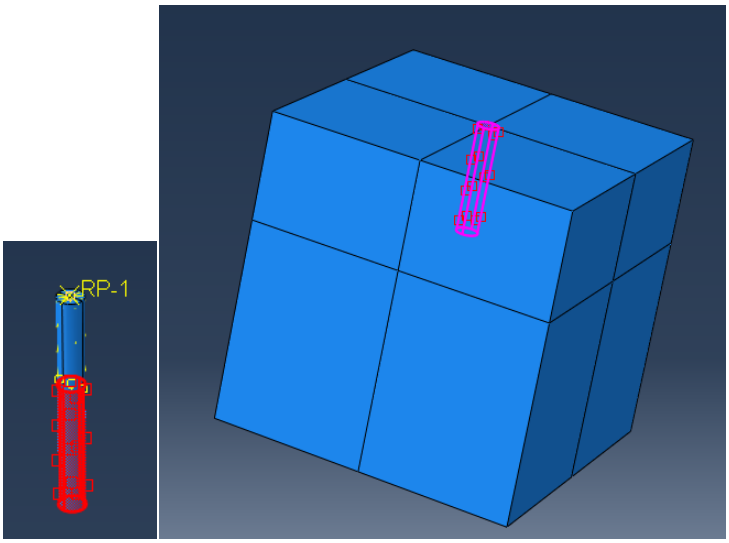

(a) (b)

Figure 33: Master and slave contact surfaces on the rebar and the concrete

Note:(a) contact surface on the embedded rebar (Master Surface) and (b) contact surface on the concrete block (slave surface).

3.2.4 Loading

Type= Displacement of 0.6mm applied uniformly to the top of the rebar.

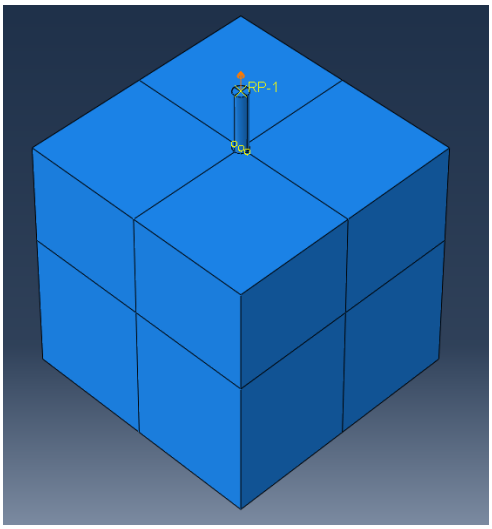

Figure 34: Displacement applied to top of rebar

3.2.5 Meshing

Mesh size=10mm

Mesh Controls:

Element Shape=Hexagonal

Mesh Technique= Structured

Element Type= 10,684 number of 8-node linear brick, reduced integration, hourglass controlled elements.

3.2.6 Pull-out Test-Mesh Convergence Study

The model was analysed with mesh sizes varying in increments of 5mm, from 5mm up to 25mm. The contact stresses were plotted against the rebar displacement for each mesh size and examined for convergence. Convergence was noted as the instance when the graph was least responsive to changes in the

mesh size. The results using this mesh size was used for comparison with the past experimental results.

3.2.7 Pull-out Test-Finite Element Analysis vs Experiment

The model was analysed using the converged mesh size identified in section 3.2.6 above and the contact stresses were plotted against the rebar displacement. This plot was then superimposed over the corresponding plot for the past experiment. Once there was agreement between the two graphs the pull-out model was considered to be successfully calibrated and the parameters cleared to be used in the subsequent analysis.

3.2.8 Pull-out Test-Time History Analysis

The model was analysed with a fine 6mm mesh and allowed to run until pull-out failure occurred. The displacement that was applied to the rebar was equal to the bar embedment depth. This was done to ensure that the bar was pulled entirely out of the concrete. The stresses in the steel bar and at the steel-concrete interface was monitored at different loading increments.

3.3 Connection Models

Ten (10) separate models were created using the same interaction property used in the calibrated pull-out model in section 3.2.7 above. The material properties were those identified in the scope above which were:

3.3.1 Material Model

Concrete Model:

Density=2.4×10^{-9} tonnes/mm^3

Compressive strength=20MPa Cylinder or 25MPa Cube

Young's Modulus=30,000 MPa

Poisons' Ratio=0.2

Concrete Damaged Plasticity Model:

C20/25 concrete with the same damage plasticity model as used above in the pull-out test calibration/verification model, See table 2 below.

Table 2: Concrete damage plasticity model used for the 10 connections

Material's parameters				Compression behaviour				Tension behaviour			
Elasticity		*Plasticity*		*Yield Stress (MPa)*	*Inelastic Strain*	*Damage Parameter*	*Inelastic Strain*	*Yield Stress (MPa)*	*Cracking Strain*	*Damage Parameter*	*Inelastic Strain*
Class	20/25	Dilation Angle	38°	11.2	0	0	0	2.9	0	0	0
E[GPa]	30	Eccentricity	0.1	18	0.0007	0	7.50E-05	1.6	0.00015	0	3.30E-05
v	0.2	f_{b0}/f_{c0}	1.12	21	0.001	0	9.90E-05	0.75	0.00035	0.4064	1.60E-04
		K	0.666	26	0.002	0	1.54E-04	0.25	0.0006	0.6964	2.80E-04
		Viscosity	0.002	20.5	0.0034	0	7.62E-04				
				13	0.005	0.1954	2.56E-03				
						0.5964	5.68E-03				
						0.8949	1.17E-02				

Anchor Bolt Material:

Size=12mm

Grade=ASTM A325

Density= 7.8x10-9 tonnes/mm3

Young's Modulus=210,000 MPa

Poisons' Ratio=0.3

Expected Yield Stress=660MPa

Ultimate tensile Strength=830MPa

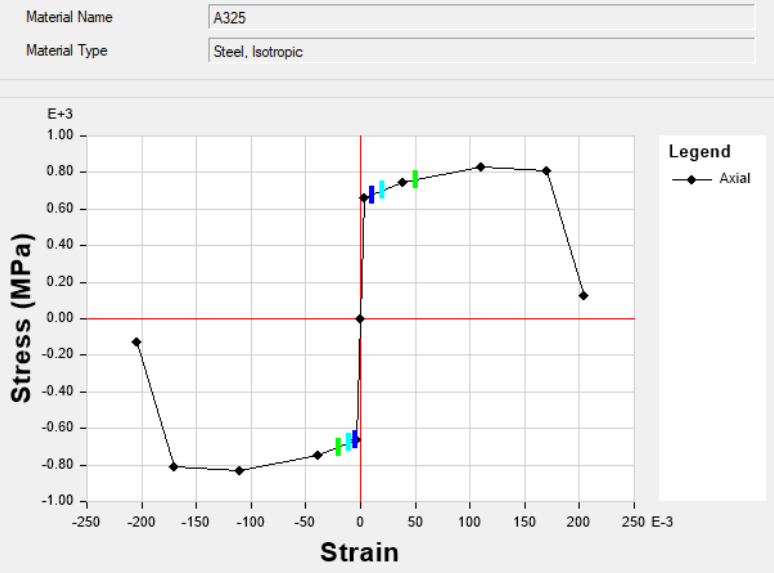

Figure 35: ASTM A325 stress strain curve for the anchor bolt

	Yield Stress	Plastic Strain
1	660	0
2	749.97	0.037991204
3	830	0.104328246
4	807.49	0.156971171
5	127.67	0.185644046

Figure 36: ASTM A325 expected yield stress vs plastic strain for the anchor bolt

Mild Steel Rebar Anchor Material:

Size=12mm

Grade=ASTM A615 Grade 40

Density= 7.8×10^{-9} tonnes/mm^3

Young's Modulus=210,000 MPa

Poisons' Ratio=0.3

Expected Yield Stress=303.37MPa

Ultimate tensile Strength=455.05MPa

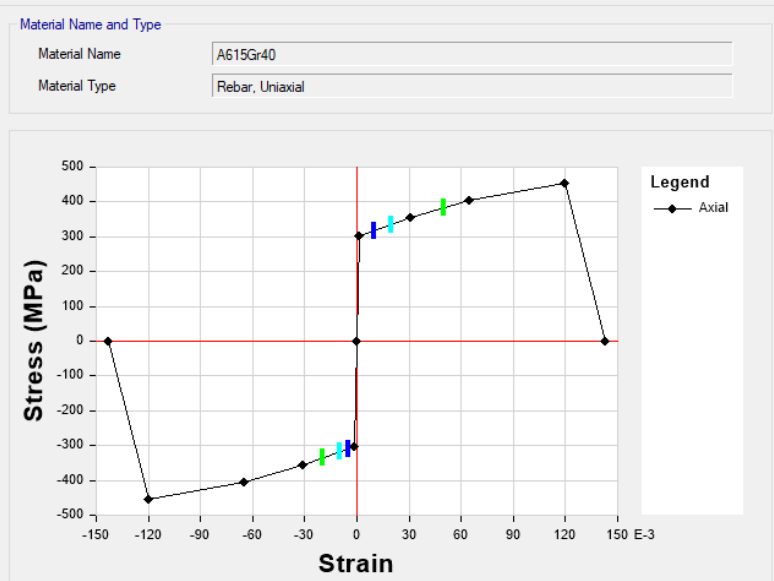

Figure 37: ASTM A615gr40 stress strain curve for the rebars

	Yield Stress	Plastic Strain
1	303.37	0
2	353.93	0.030624278
3	404.49	0.06243775
4	455.05	0.113311111

Figure 38: ASTM A615 gr40 expected yield stress vs plastic strain for the rebars

Rafter Structural Steel Material:

Section= UB 152x89x16

Grade=ASTM A992 Grade 50

Density= 7.8×10^{-9} tonnes/mm^3

Young's Modulus=210,000 MPa

Poisons' Ratio=0.3

Expected Yield Stress=379.21MPa

Ultimate tensile Strength=492.98MPa

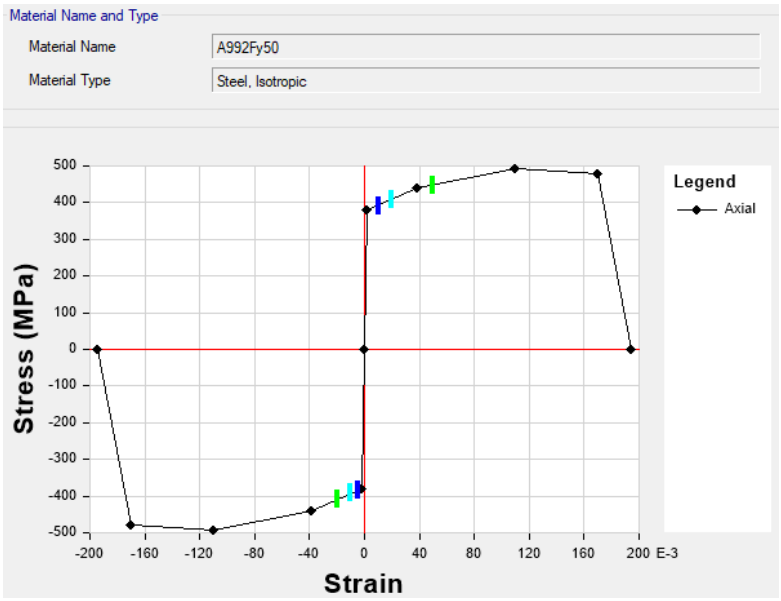

Figure 39: ASTM A992 steel stress strain curve for the steel rafter

	Yield Stress	Plastic Strain
1	379.21	0
2	439.42	0.038002328
3	492.98	0.104341146
4	477.91	0.156984468

Figure 40: ASTM A992 yield stress vs plastic strain for the steel rafter

3.3.2 Boundary Conditions:

Fixed restraints were applied to the ends and underside of each ring beam to replicate the condition of a continuous ring beam supported on a block wall. The inner end of the rafter was pinned and the outer eave end was left free to replicate the condition of a continuous rafter under uplift load where the eave end is unrestraint, See figure 41 below.

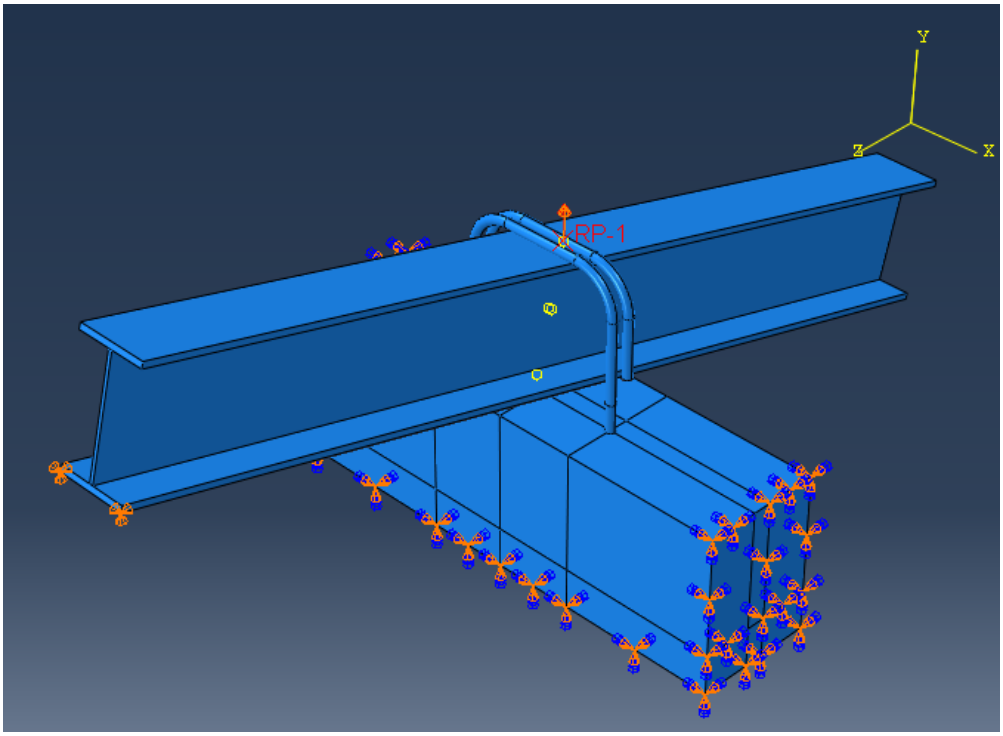

Figure 41: Boundary conditions on connection model

3.3.2 Connection Loading

A uniform displacement up to a maximum of 400 mm was applied to the top flange of each rafter to ensure that the connections were sufficiently loaded. A number of output variables were monitored including the reaction force of the rafter, von mises stress in the anchors, concrete damage, displacement at the top of the anchors and the displacement at the bottom of the anchors. The deflected shape of the connection is shown below in figure 42.

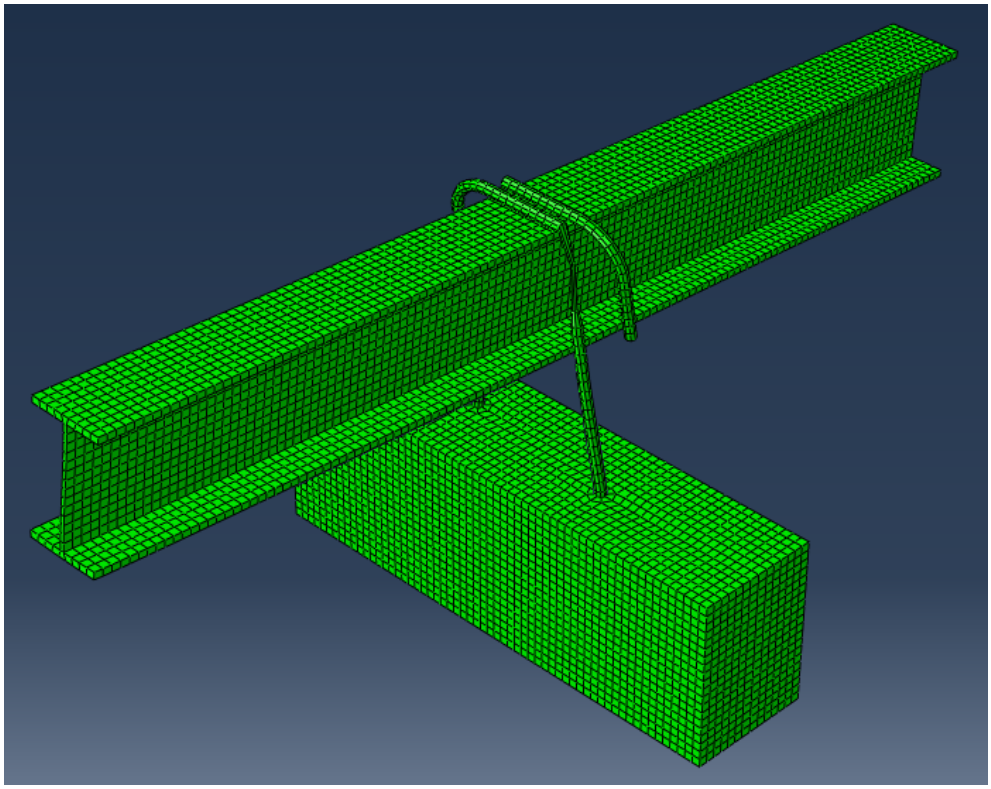

Figure 42: Deflected shape of connection

3.3.3 Connection Diagrams

1. Model 1 Diagram (Engineered / Coded Connection)

This model is considered the coded or standard connection type. It consists of a rafter with a vertical welded rafter stub sitting on a base plate. There are two anchor bolts which are embedded 150mm into the ring beam to receive the base plate.

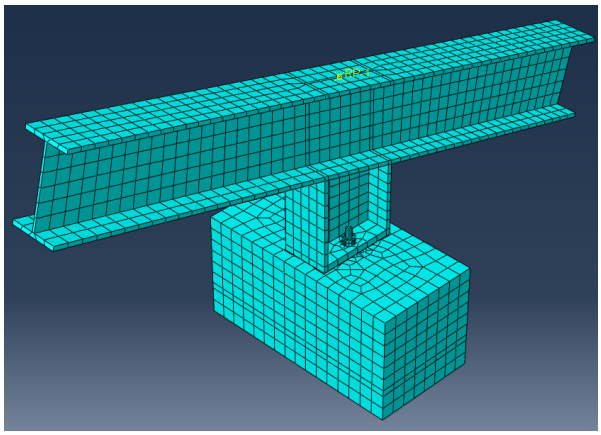

Figure 43: Model 1 assembly

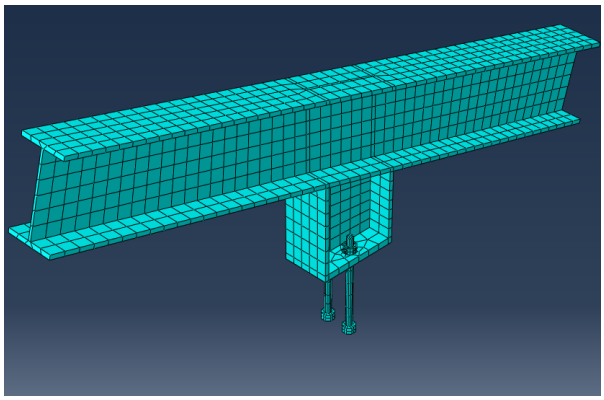

Figure 44: Model 1 rafter

Photo 4: Conn. type 1 on a house in Arima, Trinidad

Photo 5: Anchor bolts for Conn. type 1 on a house in Arima, Trinidad

2. Model 2 Diagram

This model comprises of two rebars embedded 150mm into the ring beam with a 90-degree hook at the embedded end. The top of the rebars are wrapped around and fully welded to the rafter.

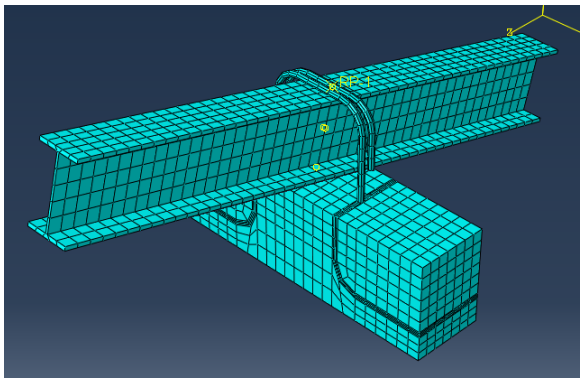

Figure 45: Model 2 assembly

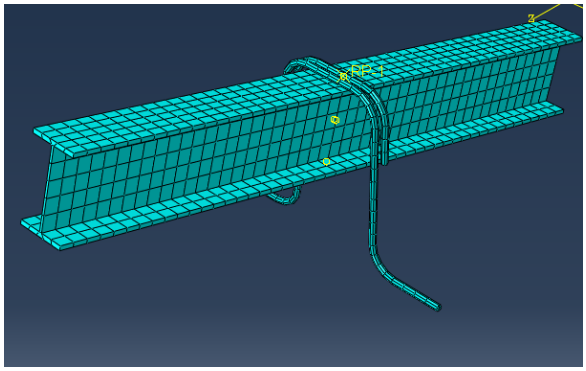

Figure 46: Model 2 rafter

Figure 47: Conn. type 2 on a house in Arima, Trinidad

3. Model 2a Diagram

In this model two rebars are developed 150mm into the ring beam without a standard hook. The top of the rebars are wrapped around and fully welded to the rafter.

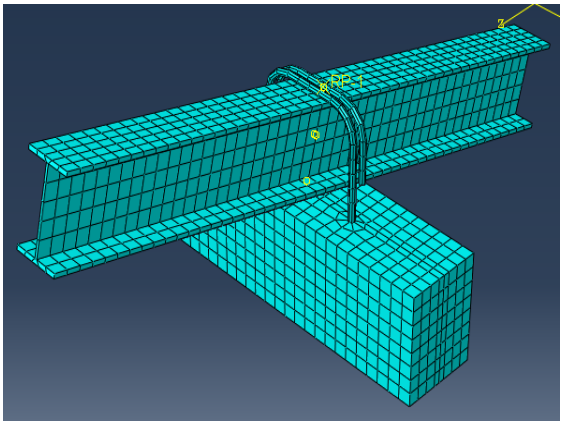

Figure 48: Model 2a &2a1 assembly

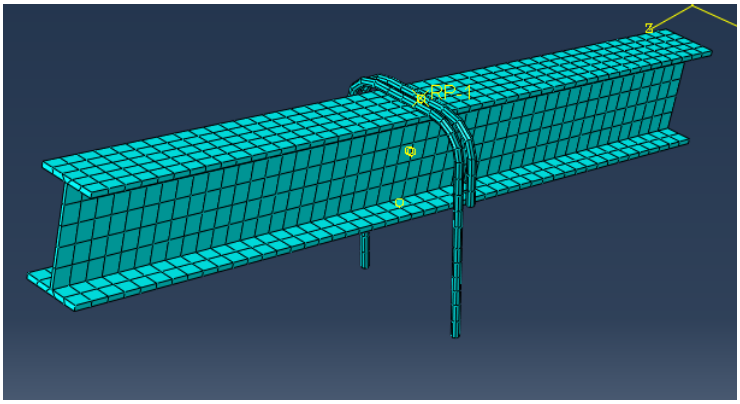

Figure 49: Model 2a & 2a1 rafter

4. Model 2a1 Diagram

This model is similar to model 2a except that in this case, no welds are used and the two rebars are simply wrapped firmly around the rafter.

5. Model 2b Diagram

In this model one rebar is developed 150mm into the ring beam without a standard hook. The top of the rebar is wrapped around and fully welded to the rafter.

.

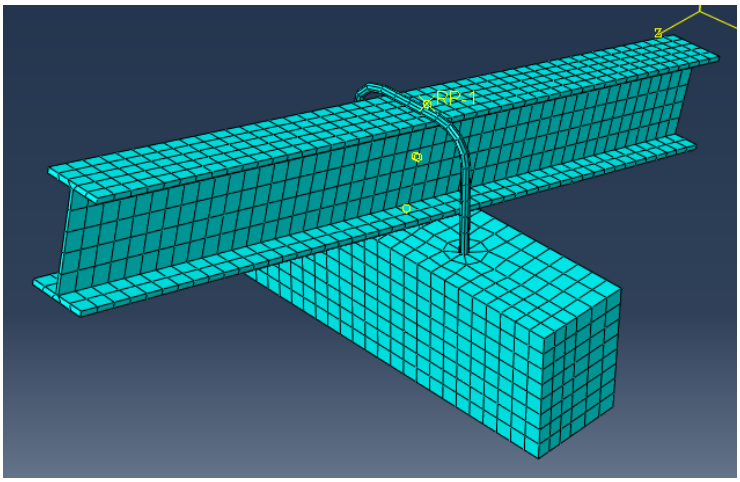

Figure 50: Model 2b& 2b1 assembly

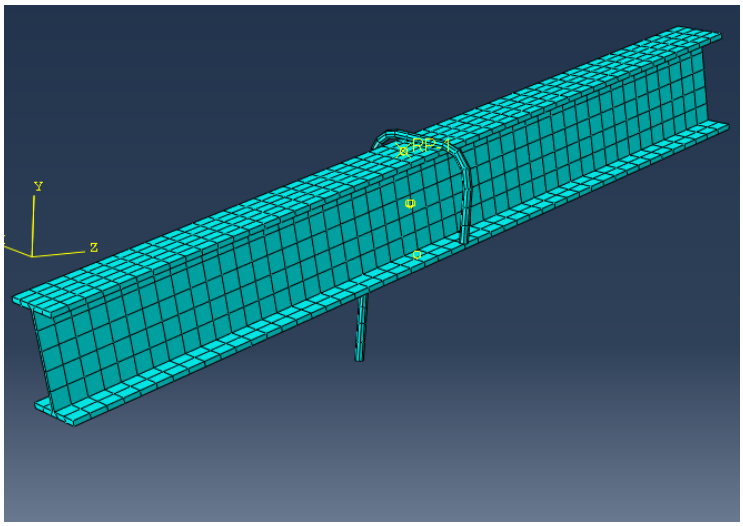

Figure 51: Model 2b & 2b1 rafter

Figure 52: Conn. type 2b on a house in Barataria, Trinidad

Figure 53: Conn. type 2b on a house in Barataria, Trinidad

6. Model 2b1 Diagram

In this model one rebar is developed 75mm into the ring beam without a standard 90-degree hook. The 75mm embedment is sufficiently less than the development length of the bar. The top of the rebar is wrapped around and fully welded to the rafter.

7. Model 3 Diagram

In this model two vertical rebars are embedded in the ring beam to a depth of 150mm with a standard hook. The rebars are welded to the side of the bottom flange of the rafter. A third horizontal stiffener rebar is welded perpendicular to the vertical rebars and to the underside of the rafter's bottom flange.

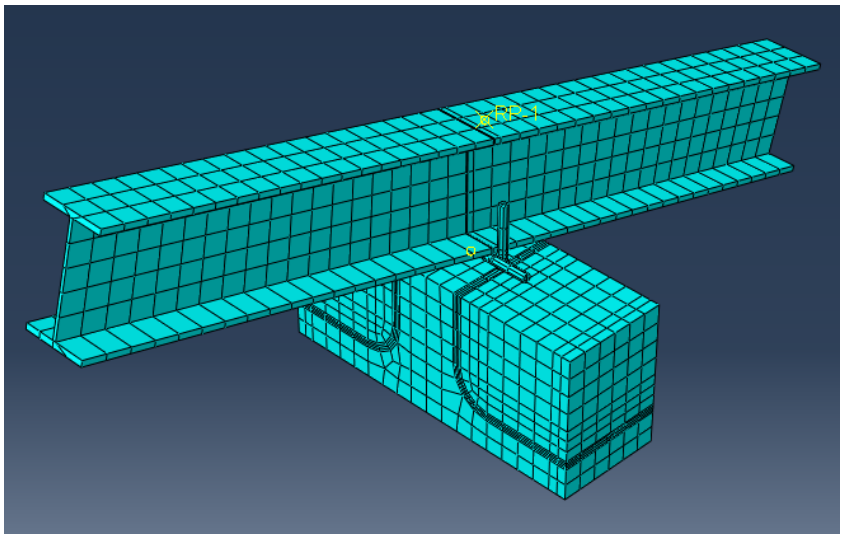

Figure 54: Model 3 assembly

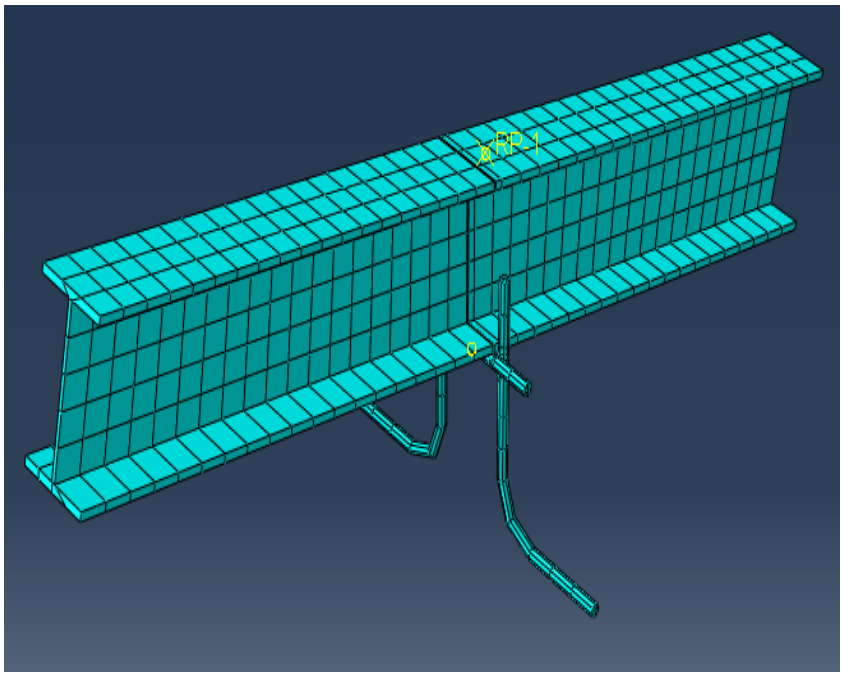

Figure 55: Model 3 rafter

Figure 56: Connection type 3 on a house in Arima, Trinidad

8. Model 3a1 Diagram

In this model two vertical rebars are embedded in the ring beam to a depth of 150mm but the rebars do not have a standard hook at the embedded end. The rebars are welded to the side of the bottom flange of the rafter. A third horizontal stiffener rebar is welded perpendicular to the vertical rebars and to the underside of the rafter's bottom flange.

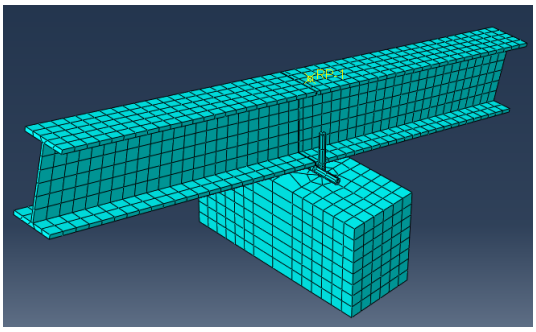

Figure 57: Model 3a1 assembly

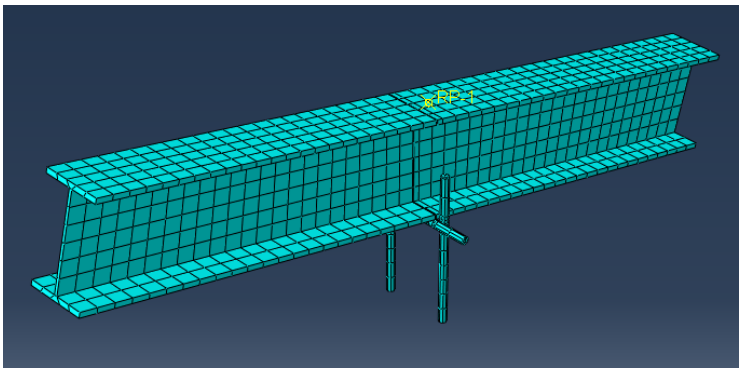

Figure 58: Model 3a1 rafter

9. Model 3a2 Diagram

In this model two vertical rebars are embedded in the ring beam to a depth of 150mm but the rebars do not have a standard hook at the embedded end. The rebars are welded to the side of the bottom flange of the rafter. The third horizontal stiffener rebar used in connection 3a1 is not present in this model.

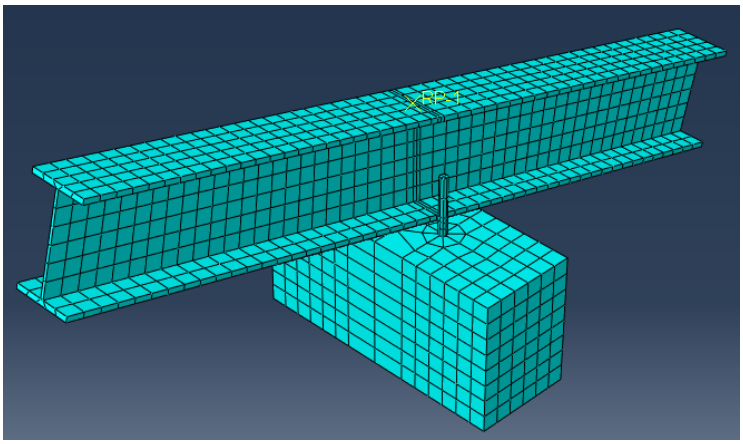

Figure 59: Model 3a2 assembly

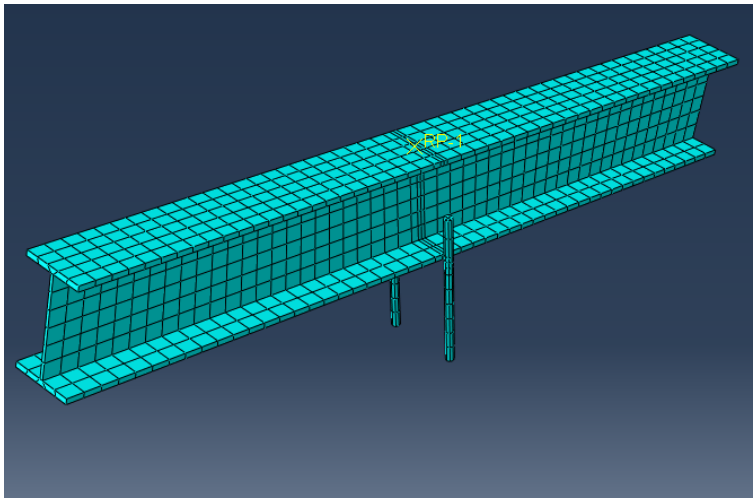

Figure 60: Model 3a2 rafter and two vertical straight rebars

Figure 61: Connection type 3a2 on a house in Arima, Trinidad

10. Model 2b1 (Retrofit Connection) Diagram

This model is a retrofit for connection model 2b1. It entails a retrofit frame consisting of horizontal steel anchors embedded into the side of the ring beam and welded or bolted to a vertical plate that fits snug with the external face of the ring beam. This plate also has a welded vertical rebar anchor which wraps around and is also welded to the top of the rafter.

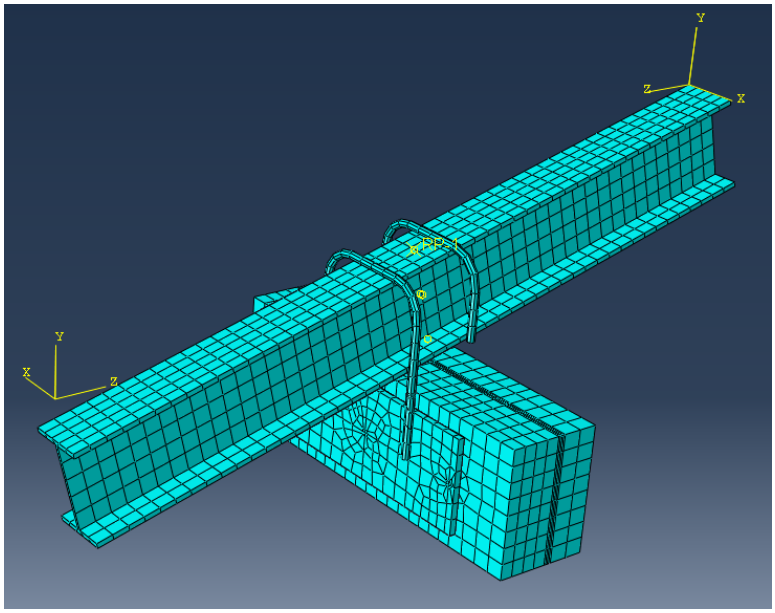

Figure 62: Model 2b1-retrofit assembly

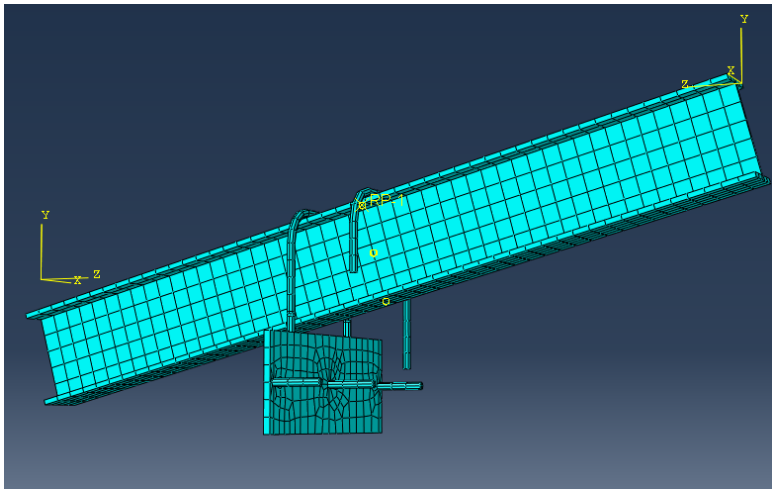

Figure 63: Model 2b1-retrofit rafter, anchor bar and retrofit frame

3.4 Connection Models-Mesh Convergence Study

Connection 2a & 3a were used to conduct a mesh convergence study by running an analysis for these connections using mesh sizes in 5mm increments from 10mm up to 40mm. A Force-Displacement curve was plotted on the same graph for each analysis and examined for convergence. The analysis was found to have converged when the Force-Displacement curves were no longer responsive or sensitive to the varying mesh size.

3.5 Connection Models-Pull-out Test

Connection 2b1 and 3a1 were modified using various increasing rebar embedment depths starting at 75mm. Connection 2b1 was chosen for this experiment because it was expected to be more susceptible to pull-out since it is anchored with only one rebar as opposed to the two anchors used in the other connections. For each embedment depth, the von mises stress in the rebar was monitored along with the displacements at the top and bottom of the rebar. The embedment depths where the anchors ceased to pull-out of the concrete was noted as the embedment limit for the “pull-out” failure mode.

3.6 Connection Models-Study on Effect of Increasing Rebar Diameter

Connection 2b was used to investigate the effect of increasing the rebar diameter on the performance of the connection. The rebar diameter was increased from 12mm to 16mm and the force displacement curves as well as the displacement of the rebar was monitored and compared.

.

CHAPTER 4

ANALYSIS & DISCUSSION

4.0 Pull-Out Test-Mesh Convergence Study

The pull-out model was analysed using mesh sizes equal to 5mm,10mm,15mm,20mm and 25mm. The results are shown below in figure 64. Based on these results, convergence occurred between the 15mm mesh and the 10mm mesh, as these curves were almost identical. This indicates that the output results using either of these mesh sizes can be considered to be accurate and insensitive to the mesh size. The 10mm mesh was selected as the converged mesh size for the subsequent analysis.

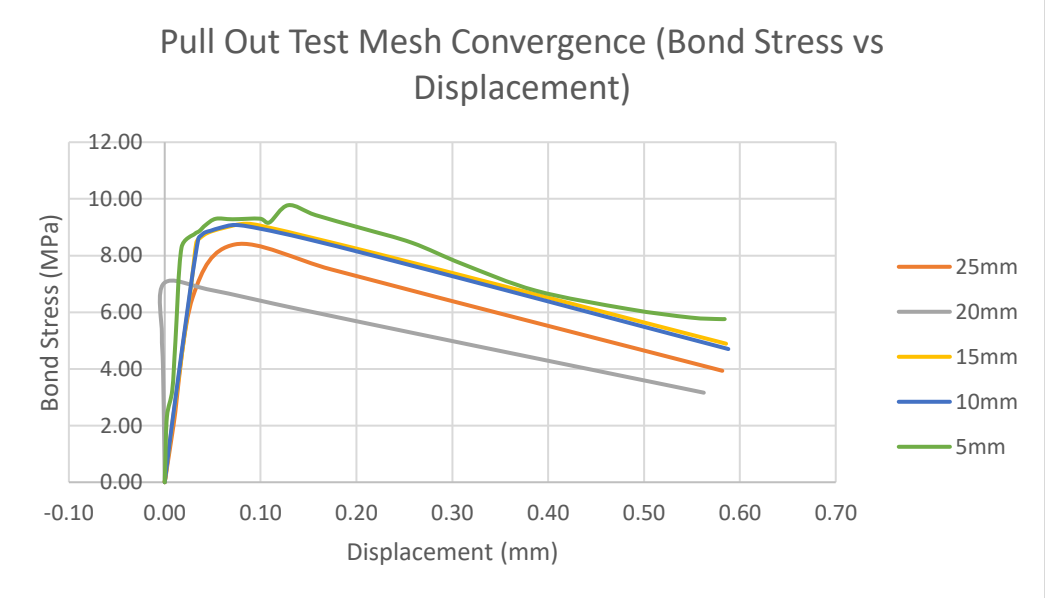

Figure 64: Results of mesh convergence study for the Pull-Out Model

4.1 Pull-Out Test-Finite Element Analysis vs Experiment

The pull-out model was analyzed using the 10mm mesh and the pull-out curve was compared with the pull-out curve from the experiment in section 3.2 which was extrapolated from figure 19 above. The results are shown below in figure 65. The stress-displacement curves show good agreement up to a maximum stress of approximately 8.9MPa and then diverges slightly as cracking and debonding is initiated. Generally, the curves show good agreement and gives sufficient confidence that the parameters have been adequately calibrated and the pull model validated.

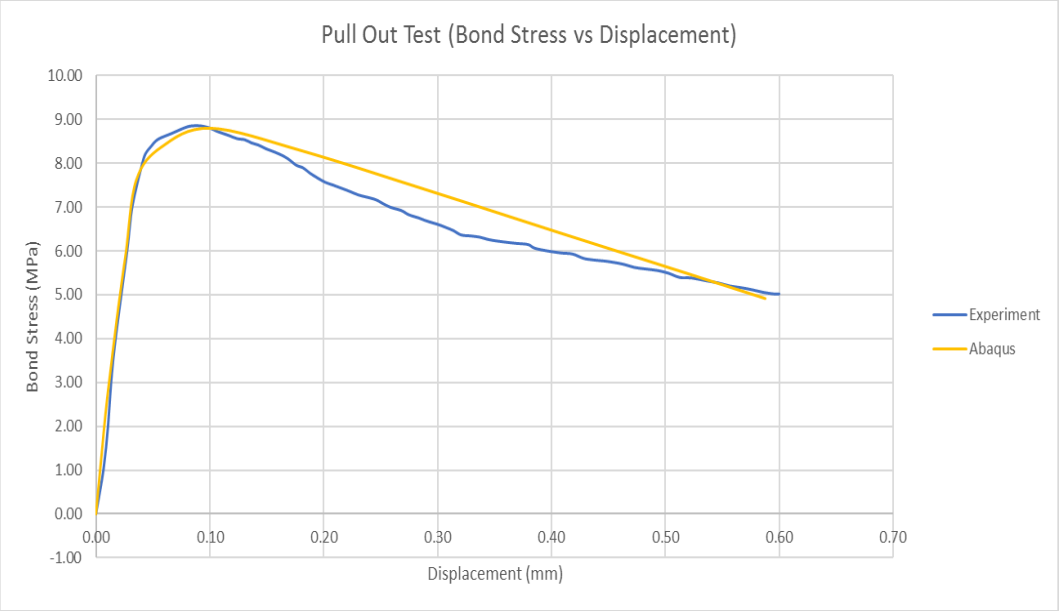

Figure 65: Results of FEA vs experiment from Beliaev et al. (2016)

4.2 Pull-out Test-Time History Stress Analysis

The pull-out model was analysed using a 6mm mesh until pull-out failure occurred. figure 66 below shows that the stress initiated at the top of the bar and continued down the bar and into the concrete as the loading increased. The contact shear stress (bond stress) reached its maximum at Step-4 with a maximum contact shear stress of 9.679MPa, with a displacement of 0.03mm and steel Von Mises stress of 122.8MPa. It is important to note that the stress in the steel within the concrete (approximately 70MPa) is substantially lower than the steel stress (122.8MPa) at the top of the bar outside of the concrete. This indicates effective force transfer across the steel-concrete interface where the stress in the steel is being dissipated within the concrete.

The stress in the steel and the bond stress decreased gradually after the maximum stress was reached. At Step-8 there was significant slippage and this can be seen by the drastic reduction in steel Von Mises stress from 100.4 MPa 5.622 MPa and a reduction in the contact shear bond stress from 8.12MPa to 0.9016MPa. From this point, the bar was pulled out of the concrete with little resistance, decreasing values of contact shear stress and steel stress. No damage was observed in the concrete during the pull-out process due to the short embedment length and adequate cover provided to the rebar.

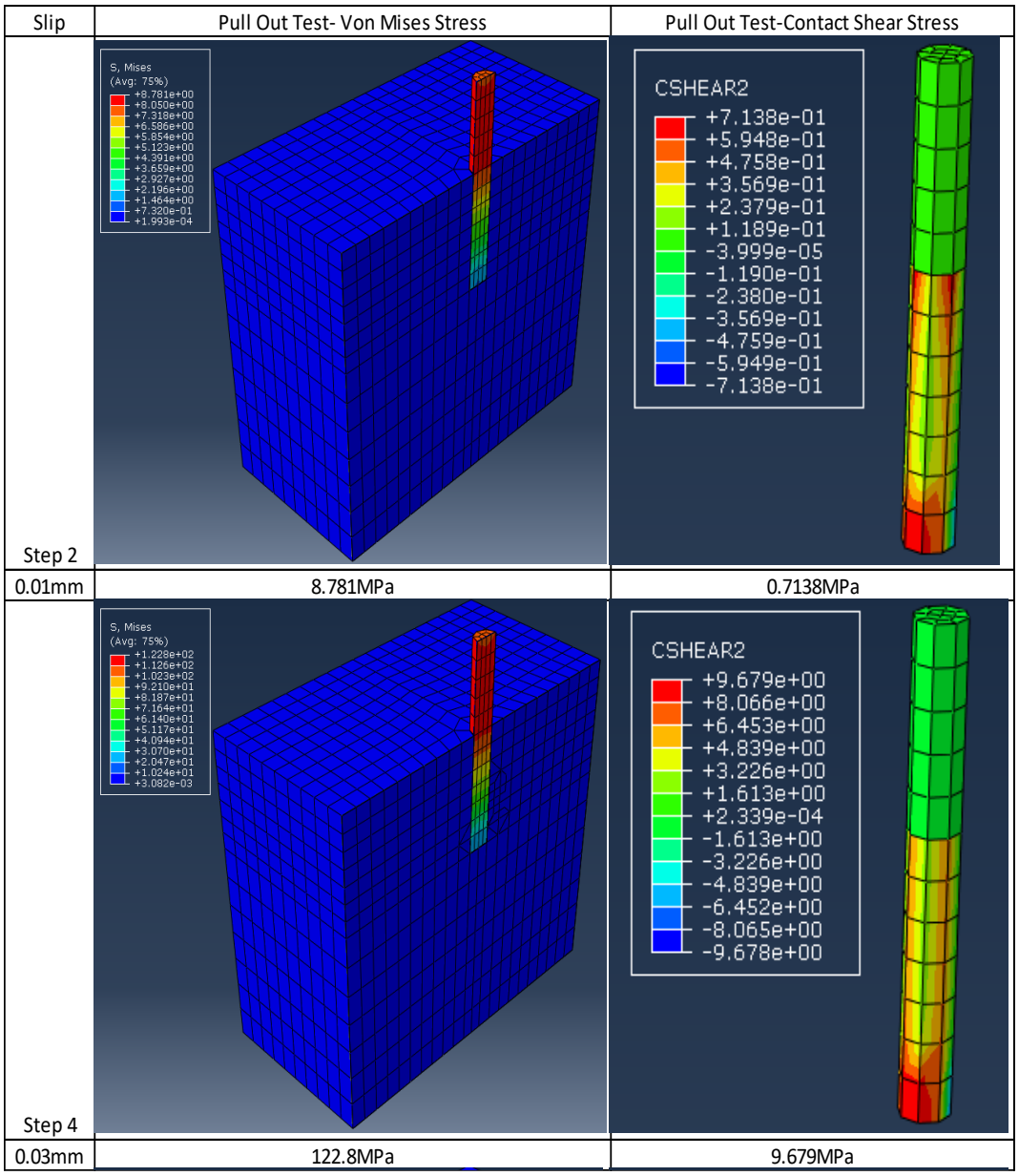

Figure 66: (a) Von Mises Stress in steel and contact shear (bond stress) at interface

Step 6	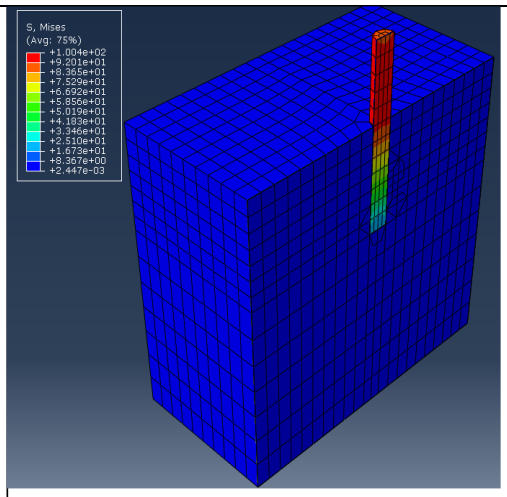	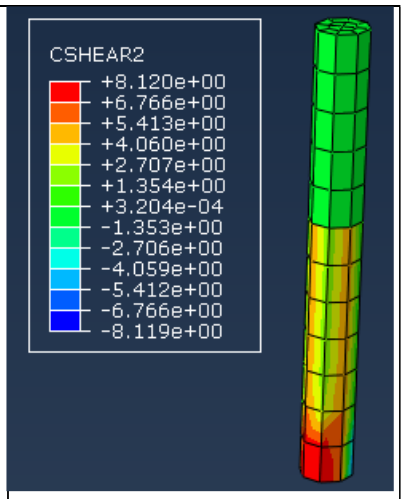
0.13mm	100.4MPa	8.12MPa
Step 8	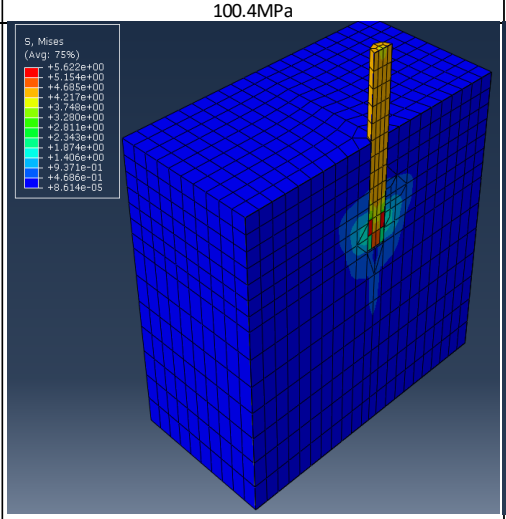	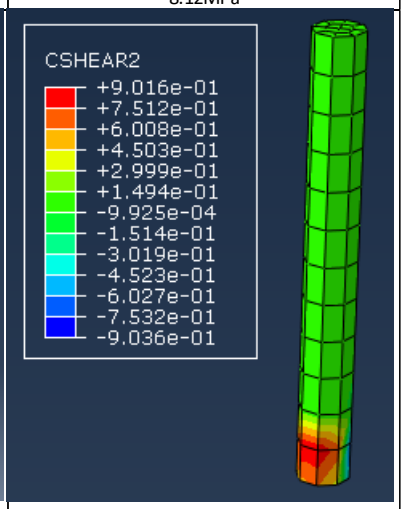
1.23mm	5.622MPa	0.9016MPa
Step 12	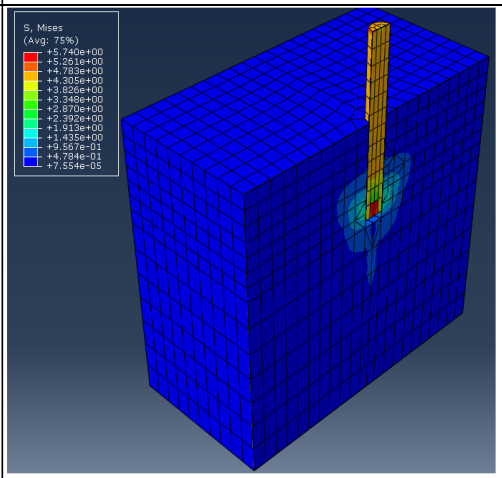	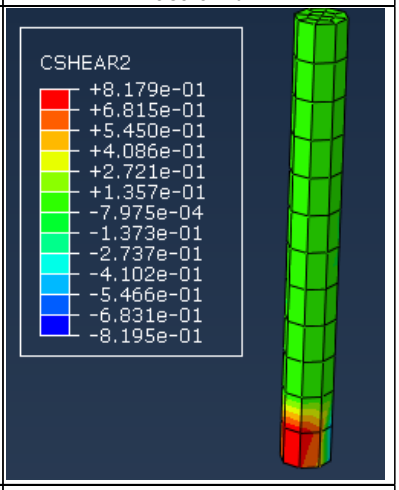
5.12mm	5.740MPa	0.8179MPa

Figure 67: (b) Von Mises Stress in steel and contact shear (bond stress) at interface

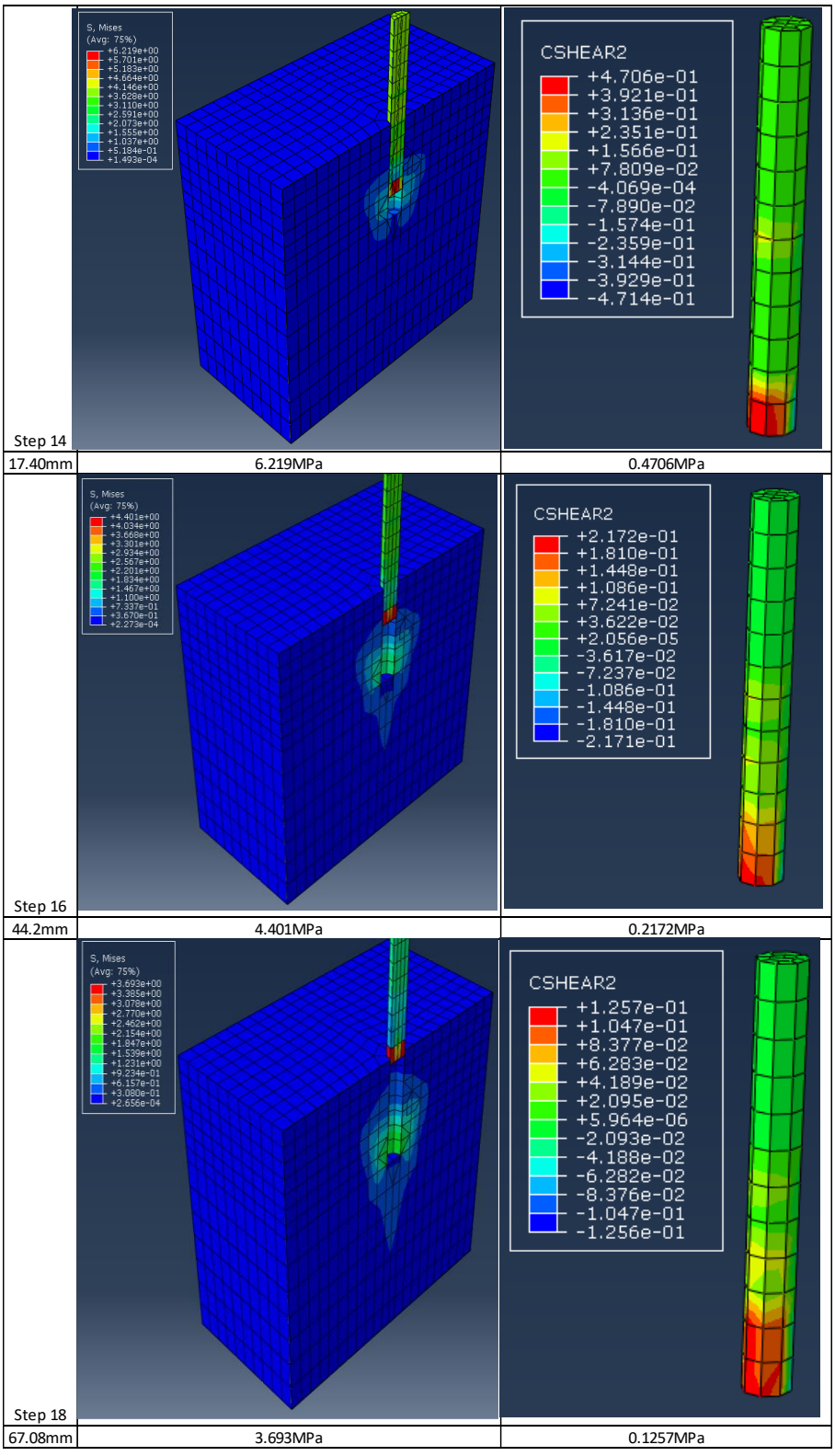

Figure 68: (c) Von Mises Stress in steel and contact shear (bond stress) at interface

4.3 Connection Models-Mesh Convergence Study

Connection 2a1 was analysed using mesh sizes equal to 10mm, 15mm, 20mm, 30mm, 35mm and 40mm. The results are shown below in figure 69. With the exception of the 40 mm mesh, the results show good convergence particularly before the yield point is reached. There is less post-yield convergence since finite element analysis are typically less stable when there is significant inelastic deformation. For this analysis, a median mesh size of 25mm can be appropriately considered as the converged mesh size.

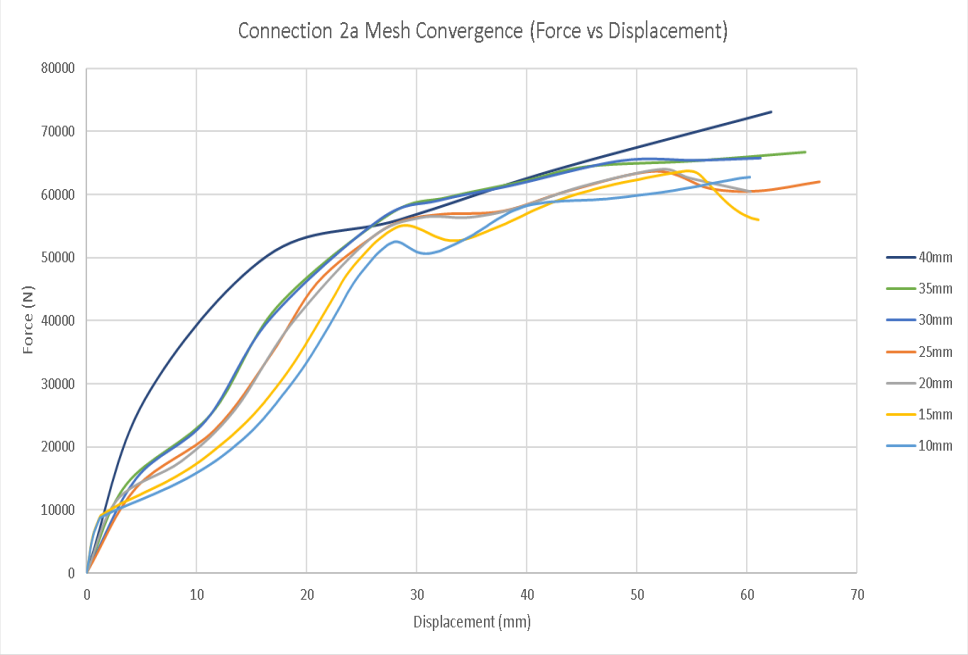

Figure 69: Mesh convergence-force vs displacement graph for type 2 connections

The procedure was then repeated with connection 3a1 where the analysis was carried out using mesh sizes varying in increments of 5mm between 40mm and 25mm. The results are shown below in figure 70. The results again show very good convergence before yield. As such, a mesh size of 25mm was selected for use in the subsequent analyses as it was expected to provide an optimal balance between accuracy and computation time.

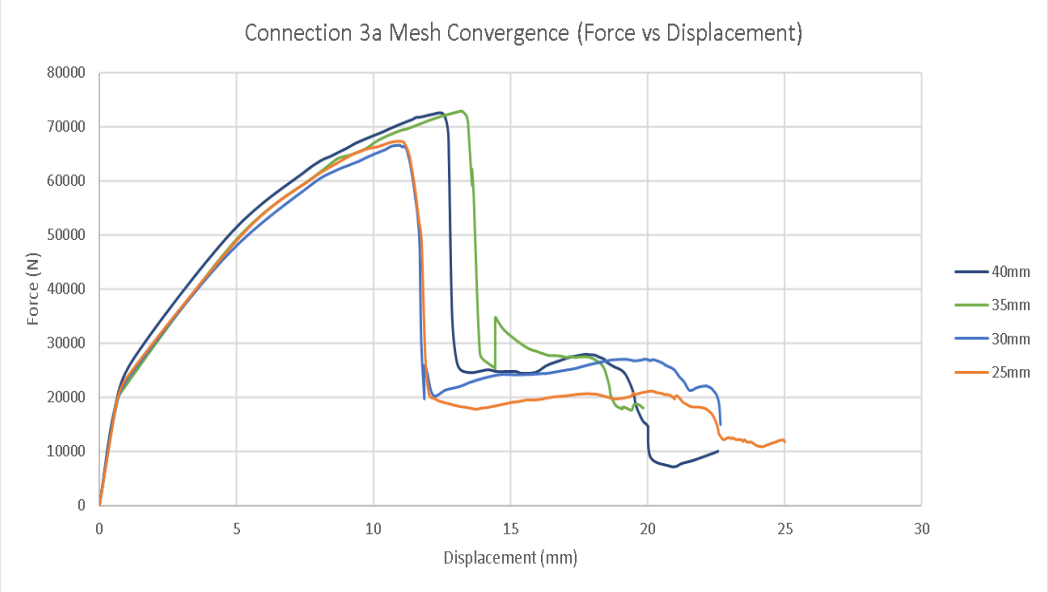

Figure 70: Mesh convergence-force vs displacement graph for type 3 connections

4.4 Connection Models-Pull-Out Test

Connection 2b1 and 3a1 were used in this pull-out test to represent the type 2 and type 3 connections respectively. They were both analysed with various anchor embedment depths varying from 75mm up to 150mm for connection 2b1 and varying from 75mm up to 210mm for connection 3a1, the displacement at the bottom of the anchor was monitored for each analysis.

Figure 71 below shows that for connection 2b1, there was complete pull-out with the 75mm embedment where the anchor bottom displacement exceeded the embedment depth. Between embedment depths of 85mm and 120mm, there was increased pull-out resistance as demonstrated by the steady reduction of the anchor bottom displacements and the negative gradient of the graph. The slope of the graph plateaued at an embedment depth of 120mm where the anchor bottom-displacements approached zero. Based on this, the effective embedment depth to preclude pull-out, was conservatively taken as 120mm.

Figure 73 below shows that for connection 3a1 there was no resistance to complete pull-out between embedment depths of 75mm and 155mm where anchor displacements exceeded the embedment depths and there was a steady increase in the slope of the graph. From an embedment depth of 155mm, the embedment depths started decreasing steadily until the slope of the graph plateaued at an embedment depth of 185mm with an anchor bottom-displacement of around 16mm. The slope of the graph plateaued finally again at an embedment depth of 205mm with an anchor bottom-displacement close to zero. Based on this, the effective embedment depth to preclude pull-out can be conservatively taken as 205mm. This represents a 70% increase in pull-out capacity from connection 2a1.

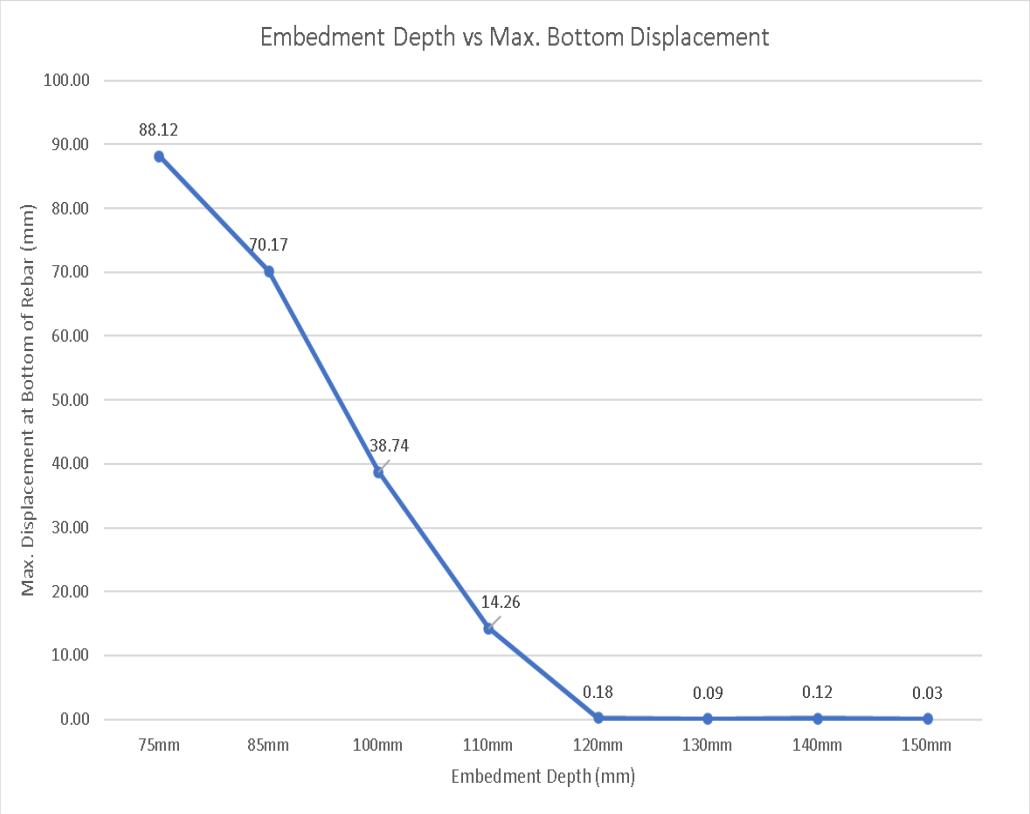

Figure 71: Pull-out test: conn.2b1 embedment vs anchor displacement

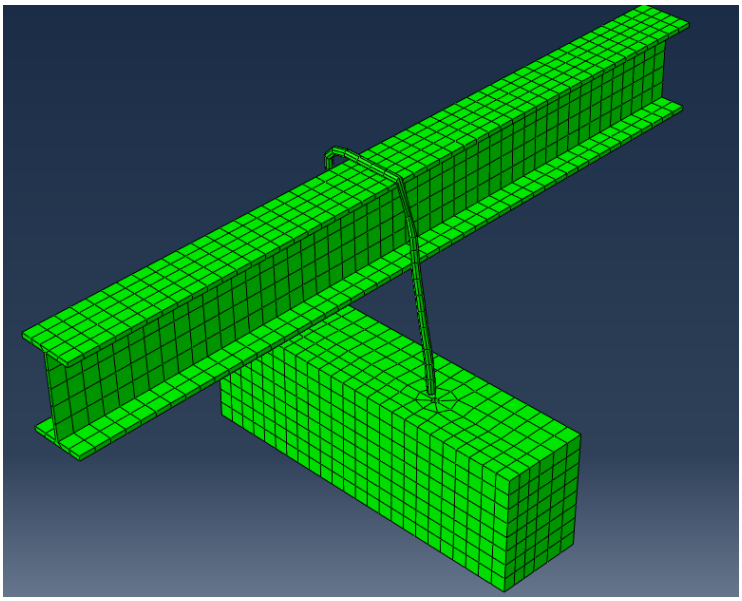

Figure 72: Deflected shape of conn. 2a1 failing by complete pull-out

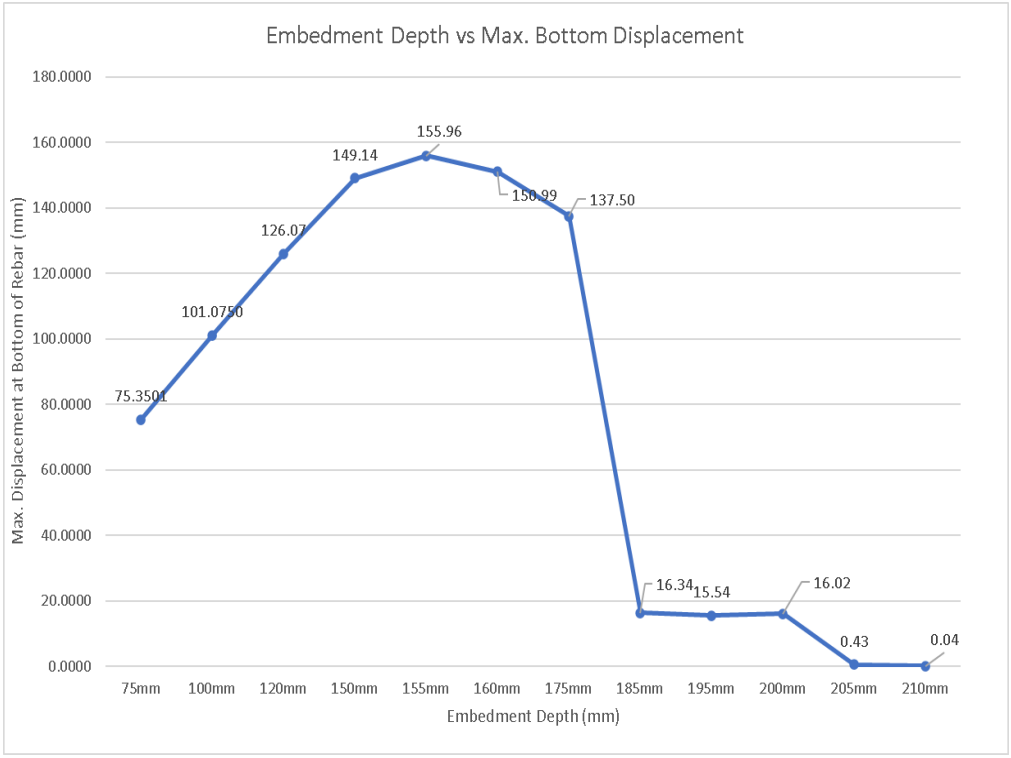

Figure 73: Pull-out test: conn.3a1 embedment vs anchor displacement

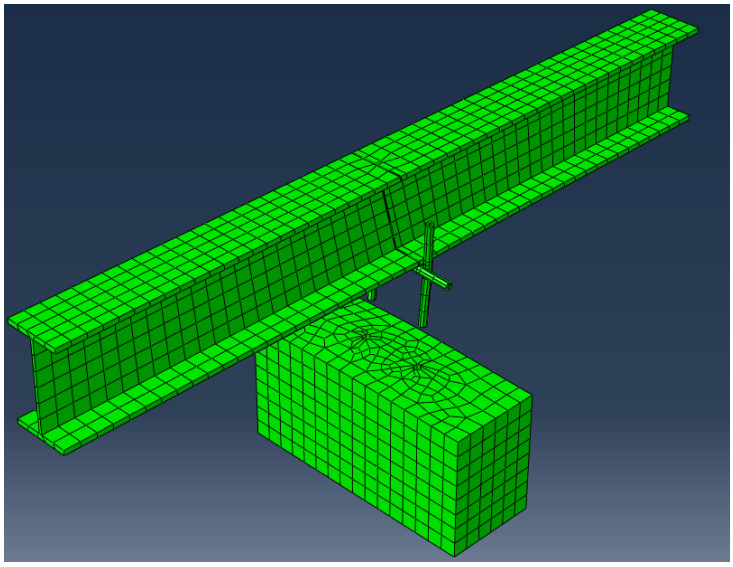

Figure 74: Deflected shape of conn. 3a1 failing by complete pull-out

4.5 Connection Models-Study on Effect of Increasing Rebar Diameter

Connection 2b was used to investigate the effect of increasing the rebar diameter on the performance of the connection. The rebar diameter was increased from 12mm to 16mm and the force as well as the displacement of the rebar was monitored and compared. The results are shown below in figure 75 and figure 76. The results show that with the 16mm rebar, the connection was able to withstand approximately 68,000 newtons of load compared to the connection with the 12mm diameter bar which was able to withstand 39,000 newtons. This is an increase in capacity of approximately 74% percent. Although the 16mm bar connection attained a higher load capacity, it also had greater slippage as shown in figure 76. The 16mm rebar had a bottom displacement of 10.297mm as opposed to the connection with the 12mm rebar which had a bottom displacement of only 0.165mm. This signifies that a larger diameter bar undergoes more slippage in developing its maximum load and thus requires a larger embedment depth.

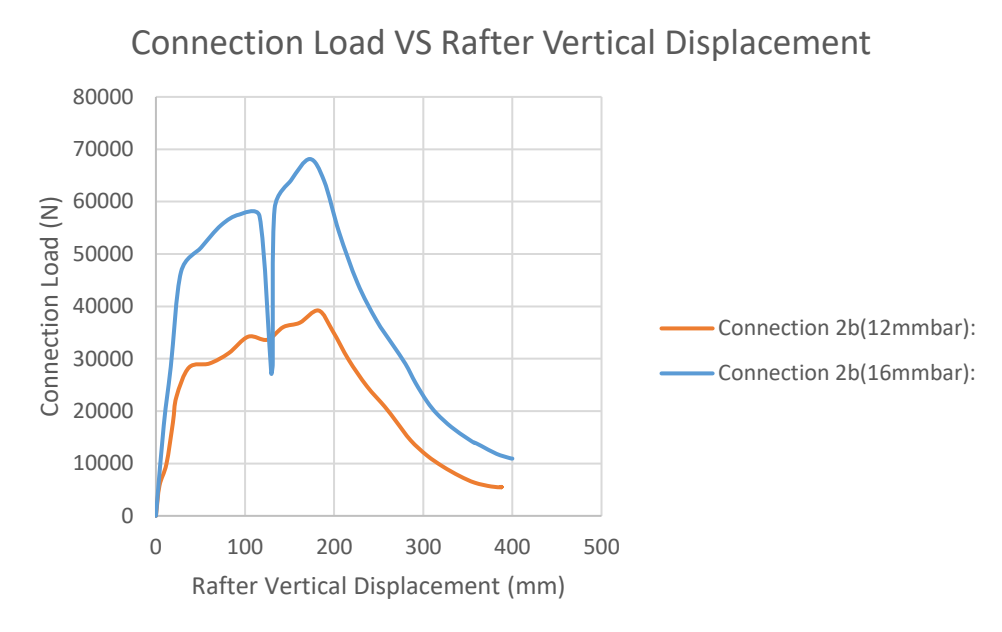

Figure 75: Load vs rafter vertical displacement of 16mm & 12mm rebars

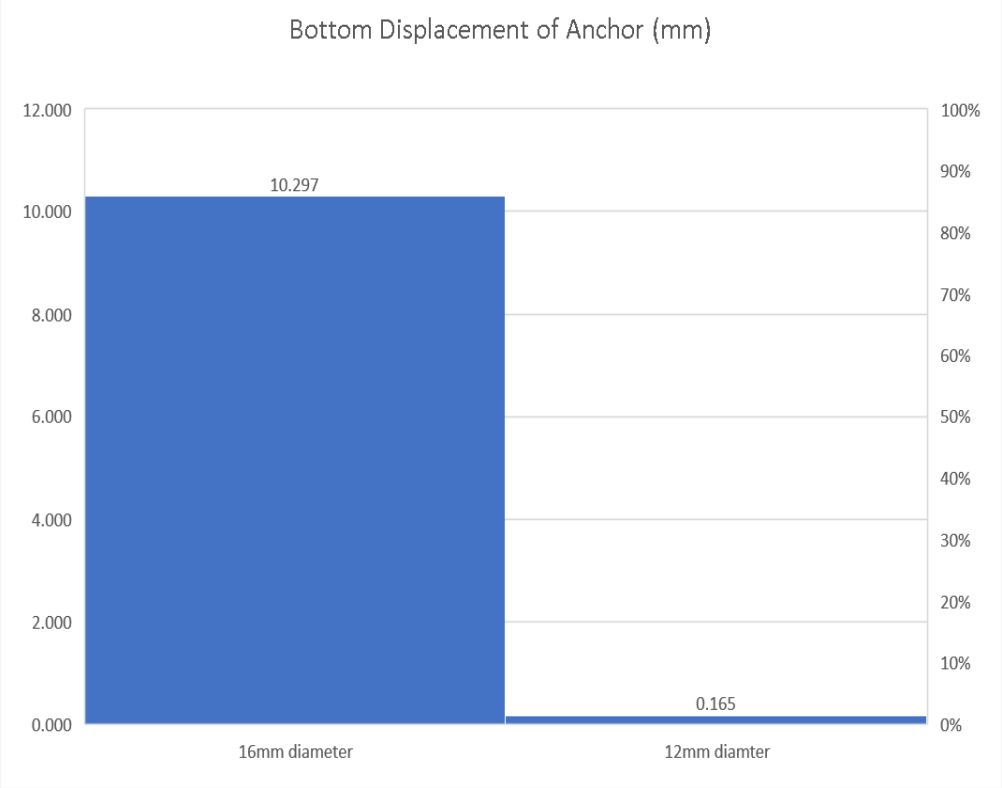

Figure 76: Maximum bot. displacement of 16mm and 12mm rebars

4.6 Wind Load Calculation

Table 3, table 4 & table 5 below summarize the expected connection wind loads for 1, 2 & 3 story buildings in Trinidad and Tobago based on Chapter 6 of the ASCE 7 code.

Table 3: Unfactored connection loads (N) on one story house

one story house		Rafter Spacing (meters)		
		6	5	3
Rafter Span (meters)	12	63250	47438	31625
	11	55344	41508	27672
	9	47438	35578	23719
	8	39531	29649	19766
	6	31625	23719	15813

Table 3 above shows that the minimum and maximum unfactored rafter connection load expected on a one-story house is 15,813 newtons and 63,250 newtons respectively.

Table 4: Unfactored connection loads on two story houses

two story house		Rafter Spacing (meters)		
		6	5	3
Rafter Span (meters)	12	67936	50952	33968
	11	59444	44583	29722
	9	50952	38214	25476
	8	42460	31845	21230
	6	33968	25476	16984

Table 4 above shows that the minimum and maximum unfactored rafter connection load expected on a two-story house is 16,984 newtons and 67,936 newtons respectively.

Table 5: Unfactored connection loads on three story house

three story house		Rafter Spacing (meters)		
		6	5	3
Rafter Span (meters)	12	71449	53587	35725
	11	62518	46889	31259
	9	53587	40190	26794
	8	44656	33492	22328
	6	35725	26794	17862

Table 5 above shows that the minimum and maximum unfactored rafter connection load expected on a three-story house is 17,862 newtons and 71,449 newtons respectively.

4.7 Conn. Models-Force, Displacement & Stress Analysis Results

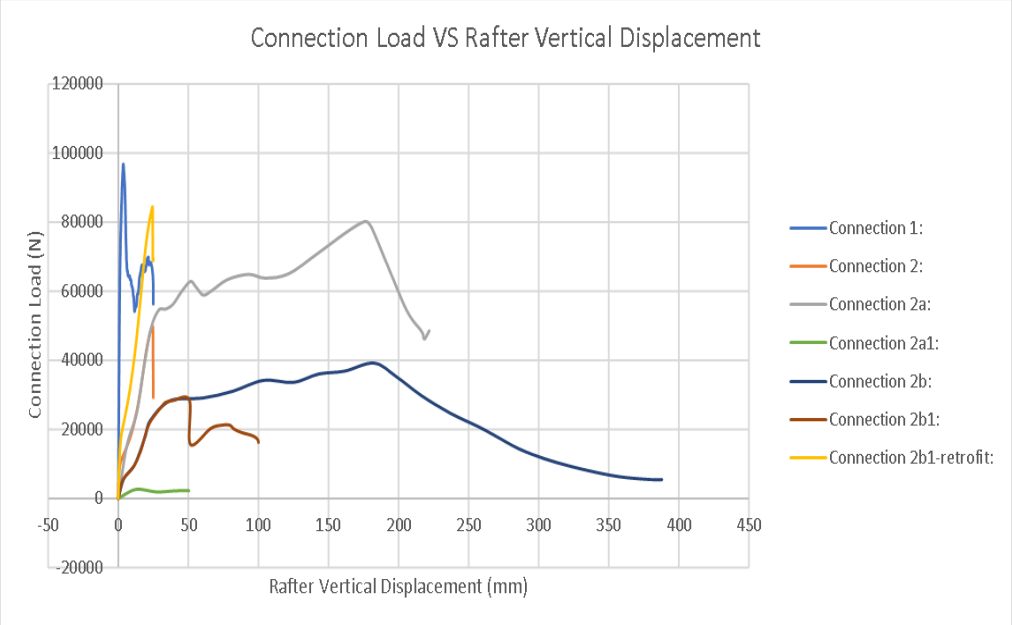

Figure 77: Load vs rafter vertical displacement for control (type-1) & type 2 connections

Figure 77 above shows that the control connection (connection 1) was able to withstand a much higher load than the other connections. The steep initial slope/gradient of the graph for connection 1 demonstrated its stiffness as it underwent the least rafter-vertical-displacement to develop its maximum load. Connections 2b,2b1and 2a demonstrated significantly less stiffness than the control connection as they required very large rafter-vertical-displacements to develop their maximum load. The connection in which the anchors were not welded to the rafter (Connection-2a1), had the least initial slope /gradient and also developed the least load resistance.

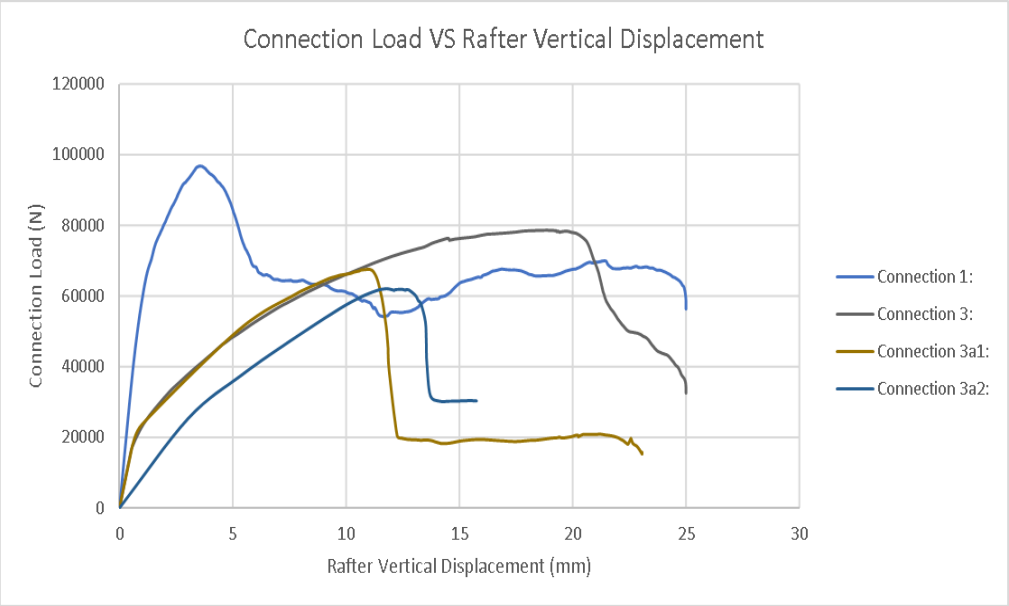

Figure 78: Load vs rafter vertical displacement for control (type-1) & type 3 connections

Figure 78 above shows that the control connection (connection 1) was able to withstand a much higher load than the other connections. The steep initial slope/gradient of the graph for connection 1 demonstrated its stiffness as it underwent the least rafter-vertical-displacement to develop its maximum load.

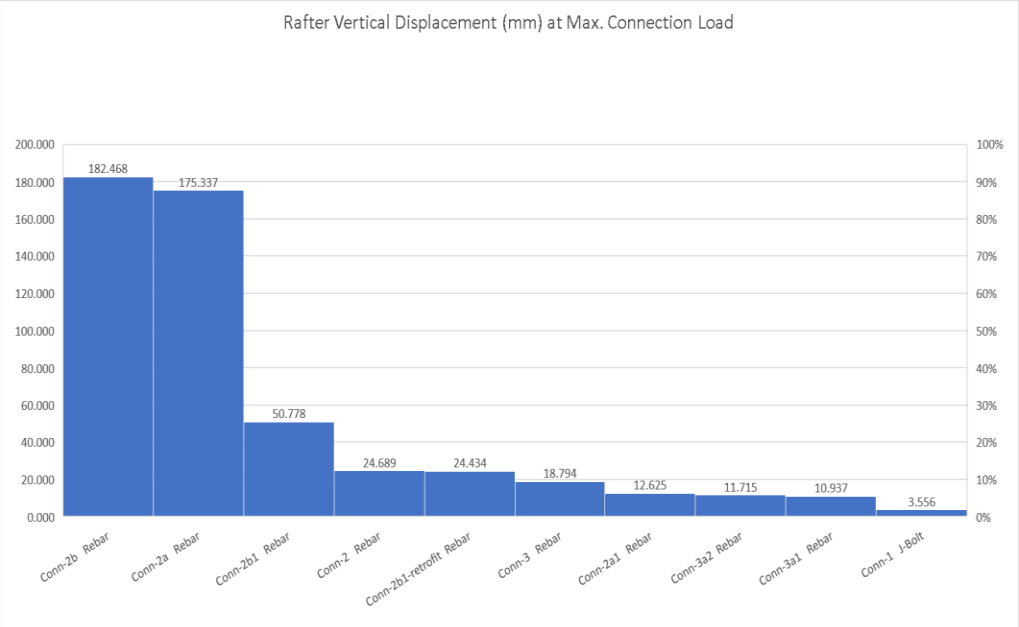

Figure 79: Rafter vertical displacements at max. load

Figure 79 above shows that the control connection (connection 1) underwent the least rafter-vertical-displacement to develop its maximum connection load. The connection 1 rafter displaced vertically by 3.556 mm while in the other connections, the rafters displaced as much as 182.468mm. The connections in which the anchor bars were welded to the bottom flange of the rafters (type-3 connections) were **stiffer** than the other connections as evident by their lower rafter displacements. On the other hand, the connections in which the anchor bars were welded to the top flange of the rafters (type-2 connections) were more **flexible** as they underwent much larger rafter-vertical-displacements.

There was a reduction in the vertical-rafter-displacement at maximum load for the retrofitted connection 2b1 compared with the original connection 2b1. The displacement reduced from 50.778mm to 24.434mm, a reduction of 52%. This indicated that there was improved stiffness in the retrofitted connection.

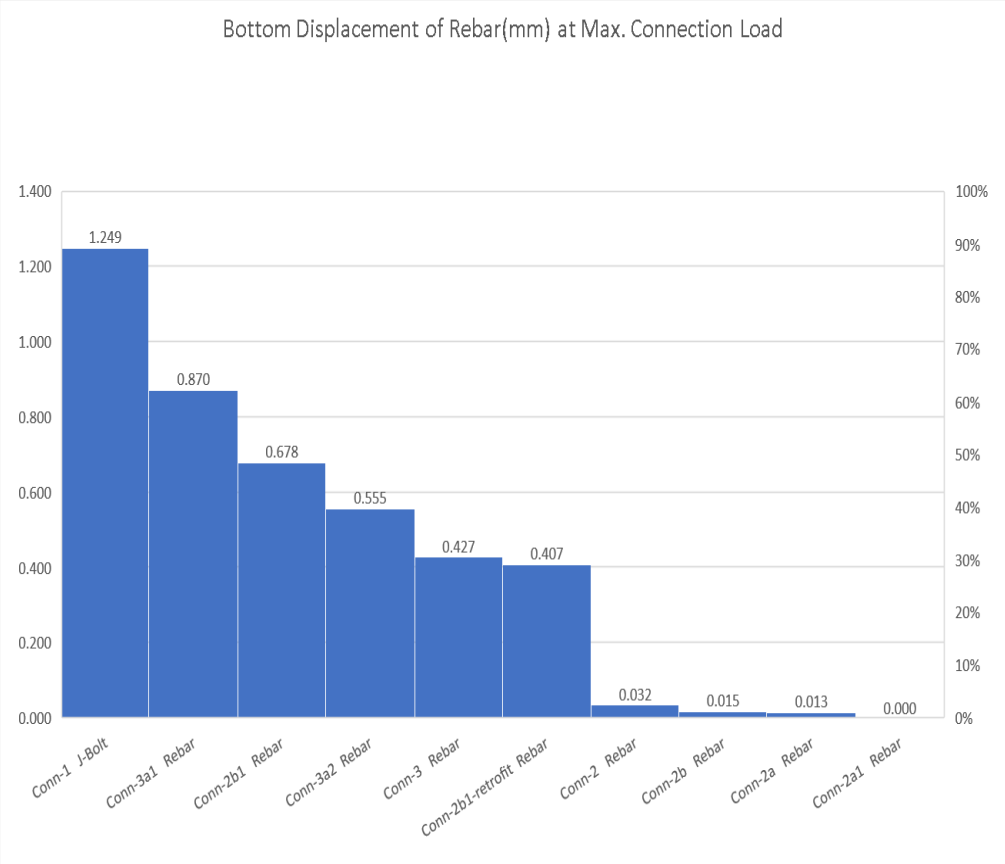

Figure 80: Displacements at bottom of rebars at max. load

Figure 80 above shows the vertical displacement at the bottom of the anchors within the concrete ring beam. This displacement is indicative of **bond-slip** at the interface between the steel anchors and the concrete the ring beam.

The type-2 connections in which the anchor bars were welded to the top flange of the rafters (close to the top of the ring beam) had the least vertical anchor displacement within the ring beam. These connections were more flexible and were not as efficient in transferring the rafter loads down into the concrete ring beam through the anchors. The type-2 connections are therefore least susceptible to bond slip or pull-out failure.

Connection 1 and the type 3 connections in which the anchors were welded to the bottom flange of the rafters (far from the top of the ring beam) had the most vertical anchor displacement within the ring beam. These connections were stiffer and more efficient in transferring their rafter loads down into the

concrete ring beam through the anchors. Connection 1 and the type 3 connections are therefore more susceptible to bond slip or pull-out failure.

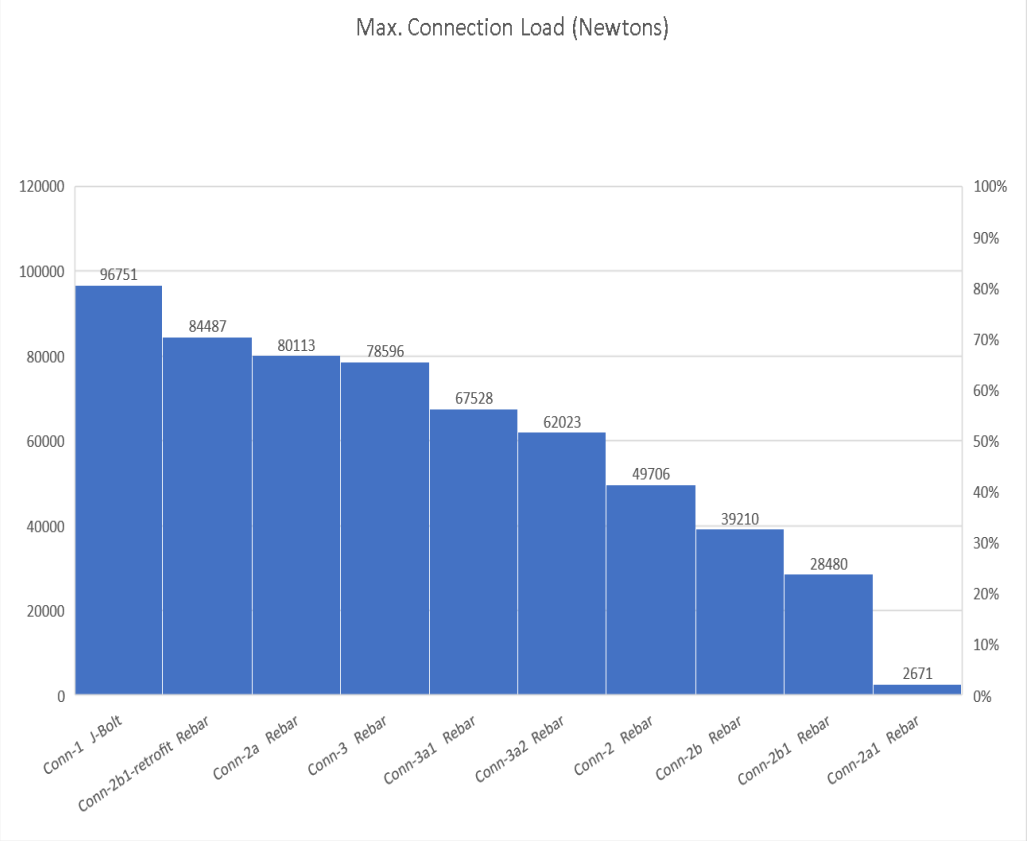

Figure 81: Maximum load resistance for each connection

Figure 81 above shows that connection-1 which is the control connection was able to develop a much higher load resistance than the other connections. This is due to its anchor being sufficiently embedded in the concrete, its anchor being restrained close to the top of the ring beam and due to the high yield strength of its anchor. Connection 2a1 had by far the least load resistance due to its anchor not being welded to the rafter. Connection 2b & 2b1had the next least load resistances due to their anchors being welded to the top of the rafter far from the top of the ring beam.

Connection-1 was able to develop a load resistance of 96,751 Newtons which is more than the maximum expected load of 71,449 Newtons for a category 1 hurricane from **table 5** above. All the other connections except connection 2a1

were also able to develop, at least the minimum connection load of 15,813 Newtons from **table 3** above. This demonstrates that all the connections except connection 2a1, can be considered adequate, once utilized with the appropriate rafter spans and rafter spacings. It is important to note, that these computed loads from **table 3**, **table 4** & **table 5** are un-factored loads and may be factored up for new designs.

It can be shown that there was a reduction of 17% in maximum connection load between the control connection (connection-1) and the next strongest connection (2a). There was also a reduction of 70% in maximum connection load between the control connection (connection-1) and the 2nd weakest connection (2b1). There was a 97% reduction for connection 2a1 which was the weakest connection.

There was also an increase in the maximum load resistance for the retrofitted connection 2b1 compared with the original connection 2b1. The load carrying capacity increased from 28,480 newtons to 84,487newtons, an increase of 196%.

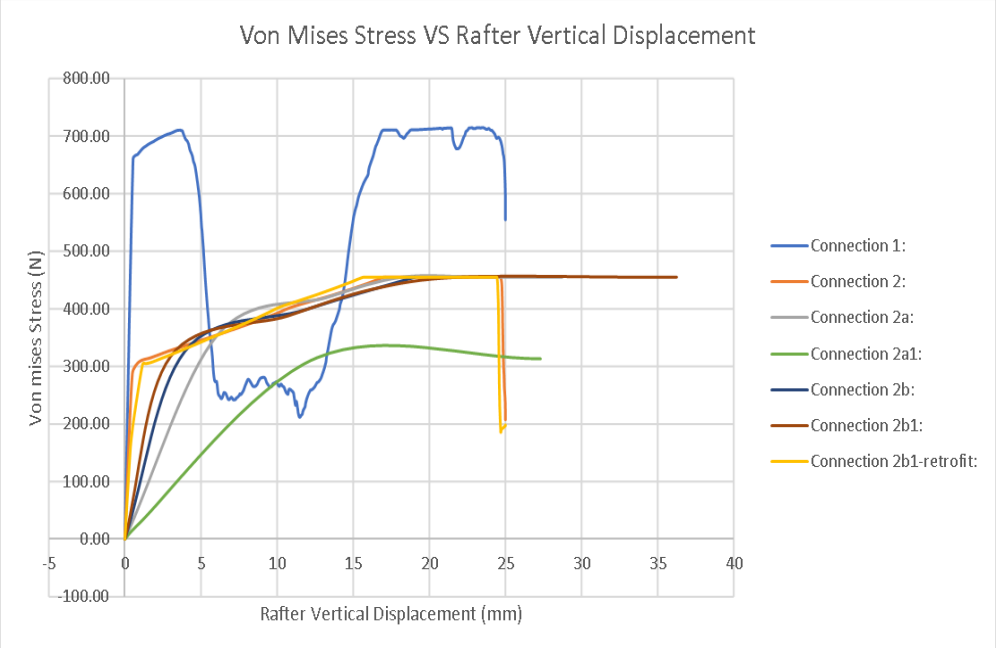

Figure 82: Von Mises Stress vs load for the control (type 1) & 2 connections

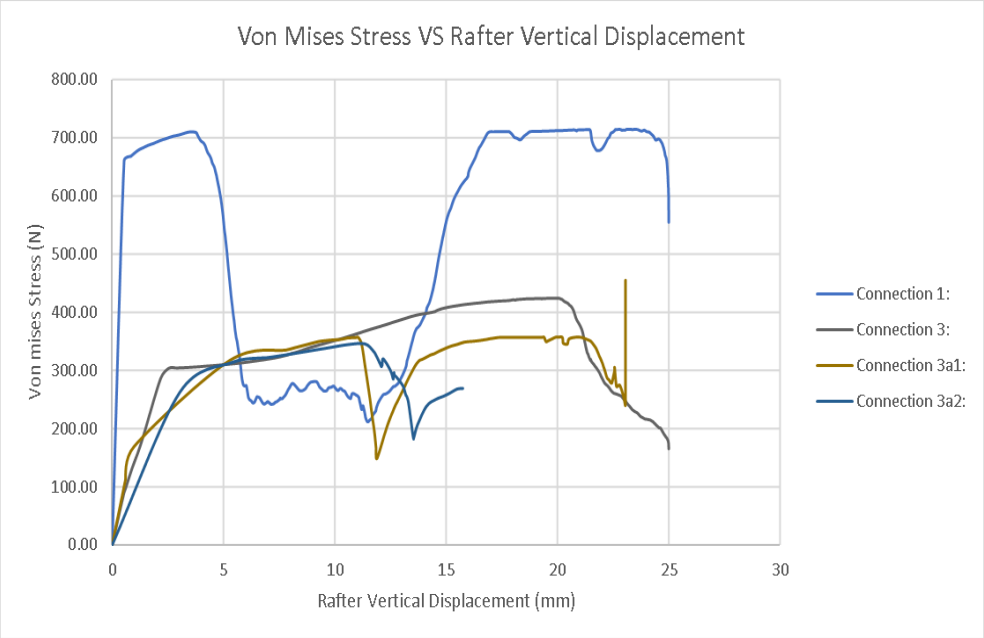

Figure 83: Von Mises Stress vs load for the control (type 1) & 3 connections

Figure 82 and figure 83 above show the von mises stress (at the highest stressed node) vs connection load for each connection. It shows that connection-1 due to the use of high strength anchor bolts, had a much higher yield strength (660MPa) compared with the yield strength (303MPa) of the mild steel anchors used in the other connections. The steep slope in the graph for connection 1 demonstrates its high stiffness. The stresses in the graphs continue to rise even after yielding, this is an indication of strain hardening which allows the connections to continue resisting load even after the yielding.

4.8 Connection Models-Time History Stress Analysis

		Conn-1 Steel Von Mises Stress	Conn-1 Concrete Damage
1/4 Max Force(N)	35912.9	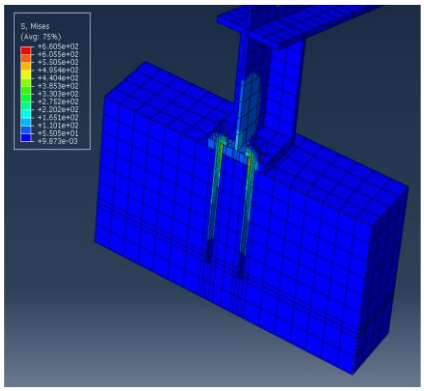	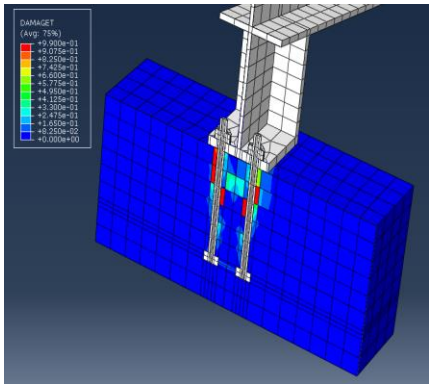
mm	0.01		
1/2 Max Force(N)	51861.3	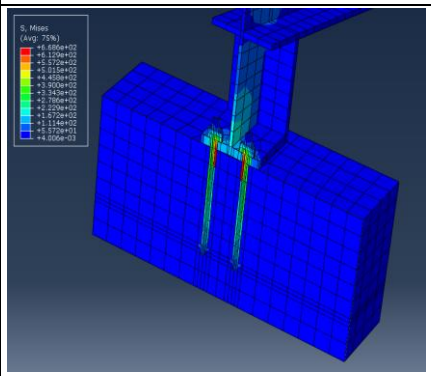	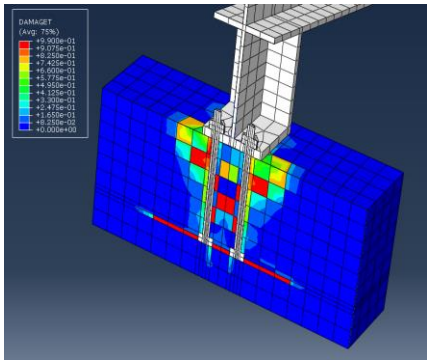
mm	0.03		
Max Force(N)	96751	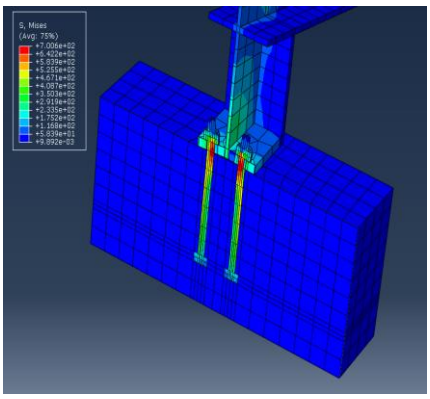	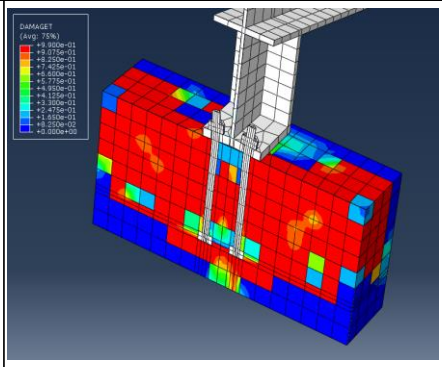
mm	1.24856		number of damaged elements =969

Figure 84: Connection 1 stepped analysis summary

		Conn-2 Steel Von Mises Stress	Conn-2 Concrete Damage
1/4 Max Force(N)	11945.1	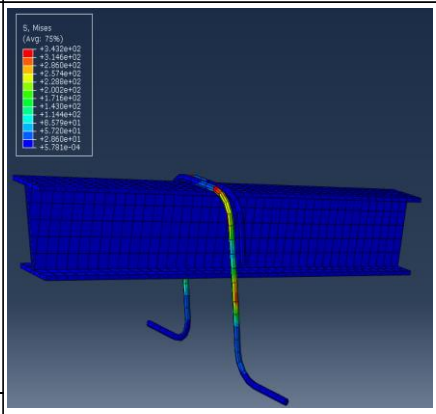	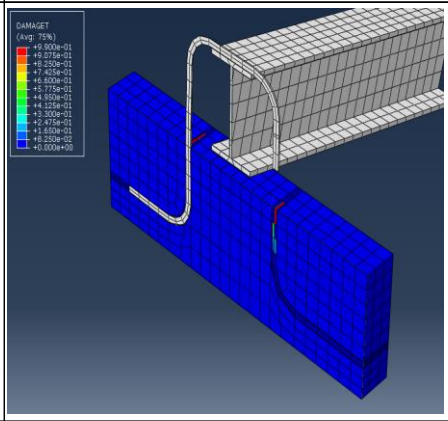
mm	0		
1/2 Max Force(N)	25854.5	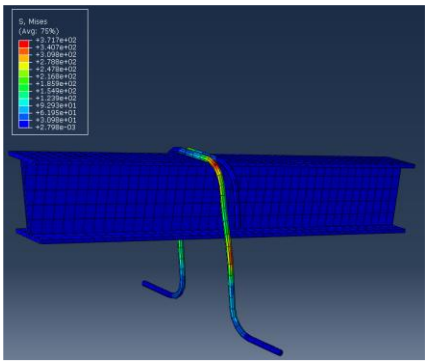	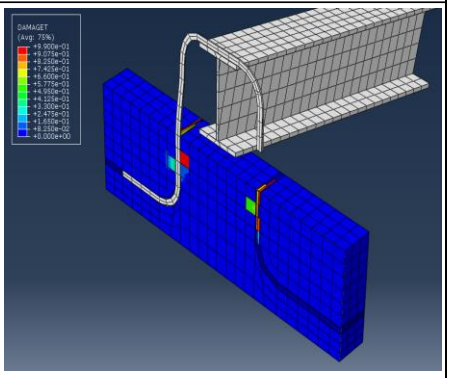
mm	0		
Max Force(N)	49706	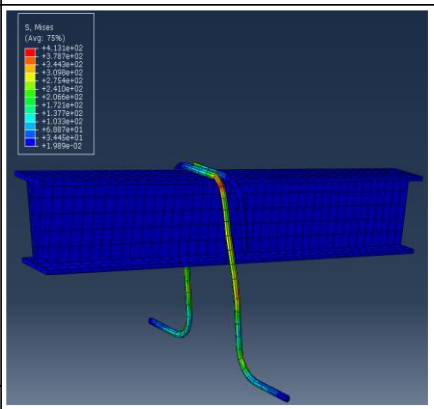	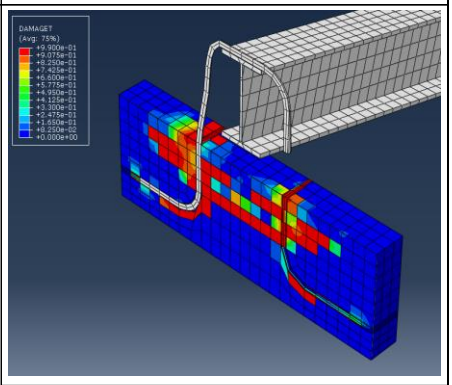
mm	0.03		number of damaged elements =860

Figure 85: Connection 2 stepped analysis summary

		Conn-2a Steel Von Mises Stress	Conn-2a Concrete Damage
1/4 Max Force(N)	25018.2	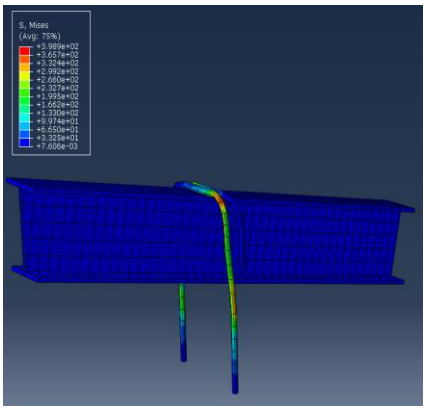	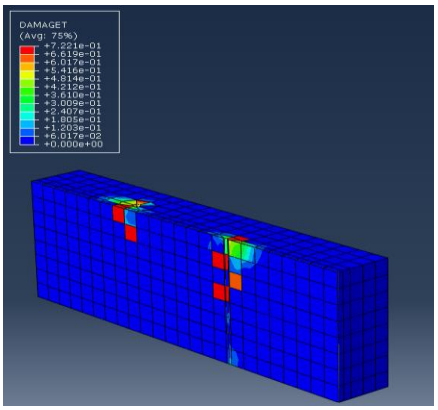
mm	0		
1/2 Max Force(N)	49201	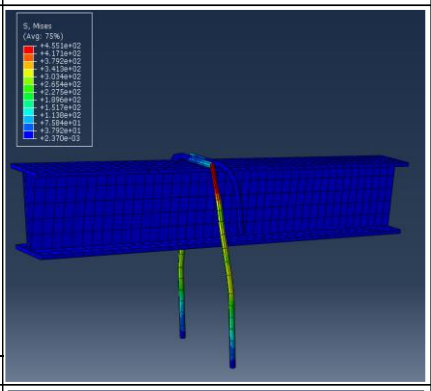	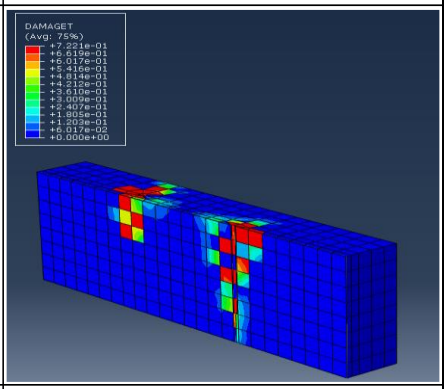
mm	0.002607		
Max Force(N)	80113	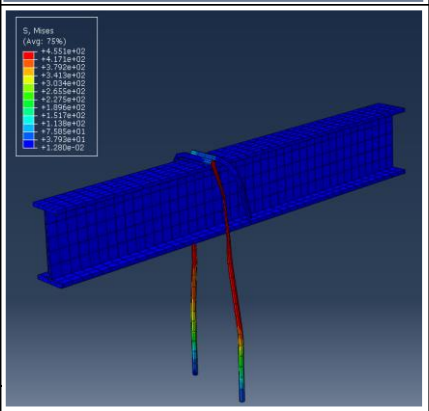	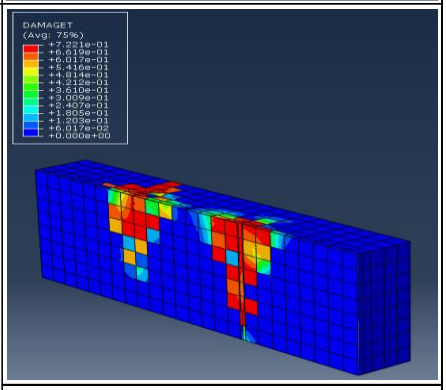
mm	0.013		number of damaged elements =159

Figure 86: Connection 2a stepped analysis summary

		Conn-2a1 Steel Von Mises Stress	Conn-2a1 Concrete Damage
1/4 Max Force(N)	202	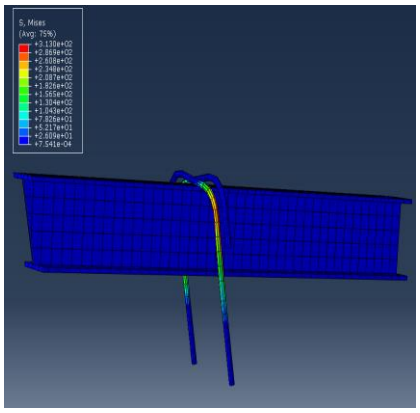	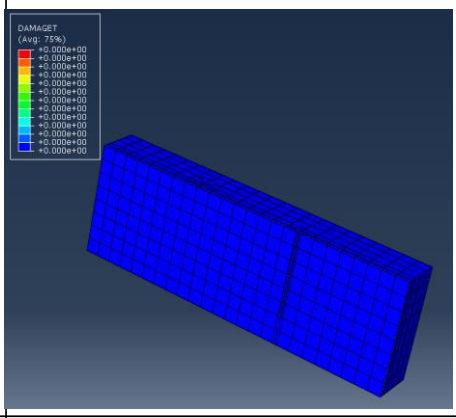
mm	0.00		
1/2 Max Force(N)	202	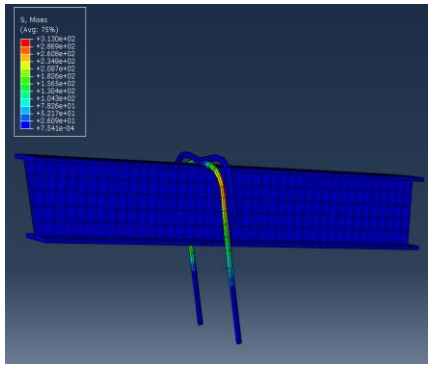	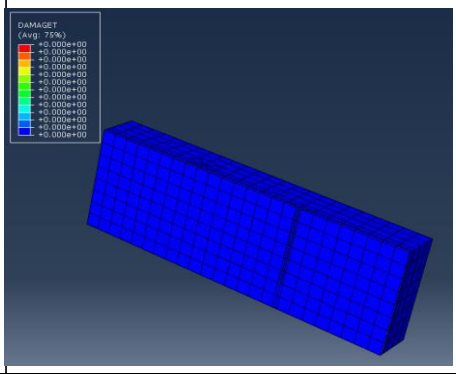
mm	0.00		
Max Force(N)	2671	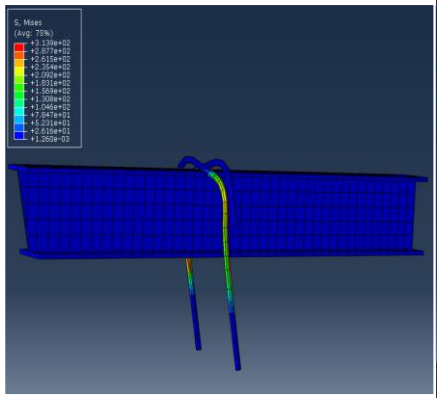	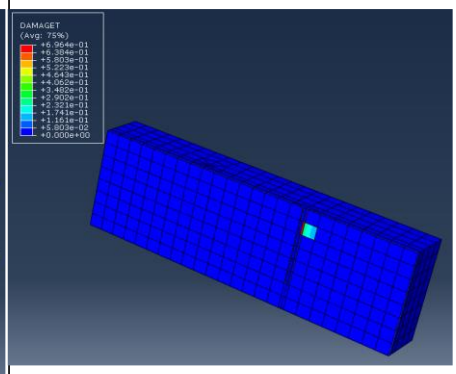
mm	0.00		number of damaged elements =4

Figure 87: Connection 2a1 stepped analysis summary

		Conn-2b Steel Von Mises Stress	Conn-2b Concrete Damage
1/4 Max Force(N)	9926.13	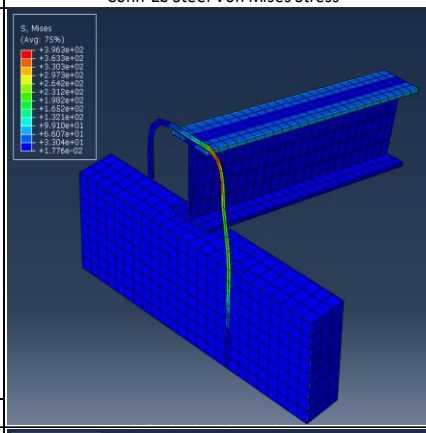	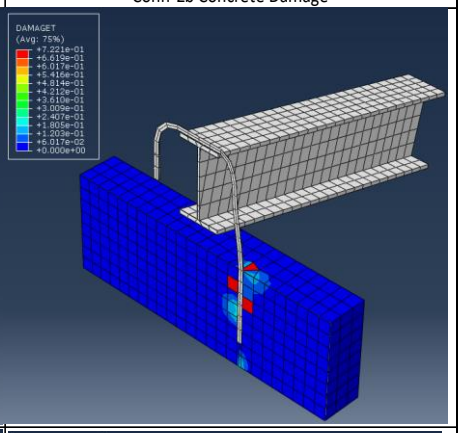
mm	0.00		
1/2 Max Force(N)	22705.1	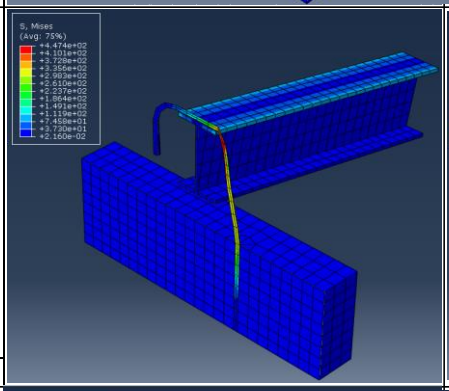	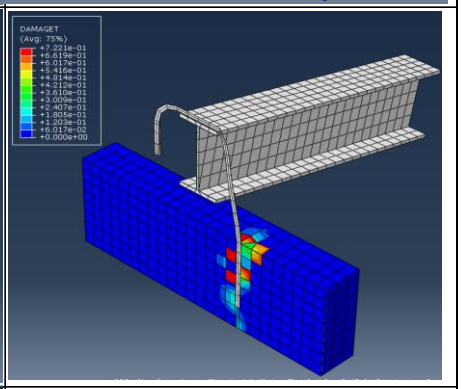
mm	0.0028		
Max Force(N)	39210	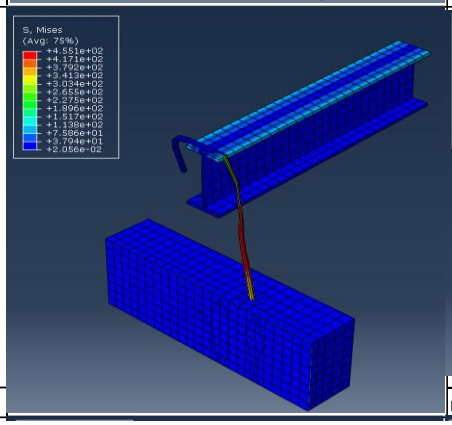	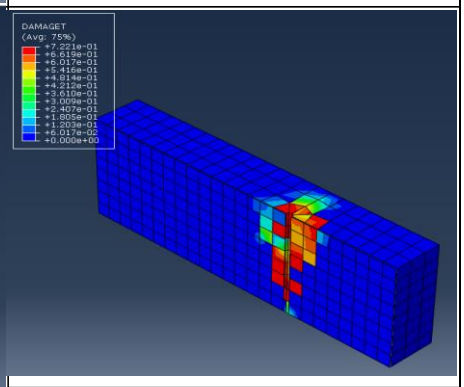
mm	0.02		number of damaged elements =87

Figure 88: Connection 2b stepped analysis summary

		Conn-2b1 Steel Von Mises Stress	Conn-2b1 Concrete Damage
1/4 Max Force(N)	5250.86	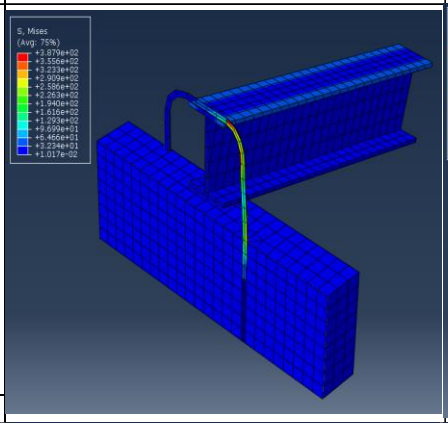	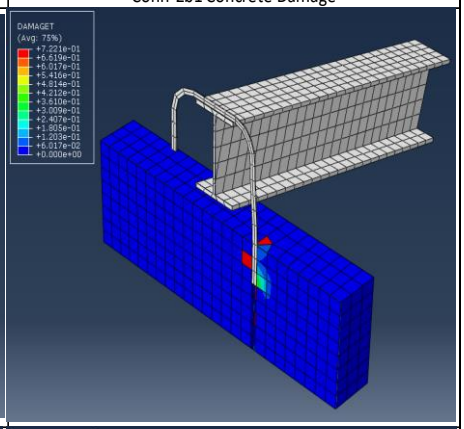
mm	0.02		
1/2 Max Force(N)	14026.8	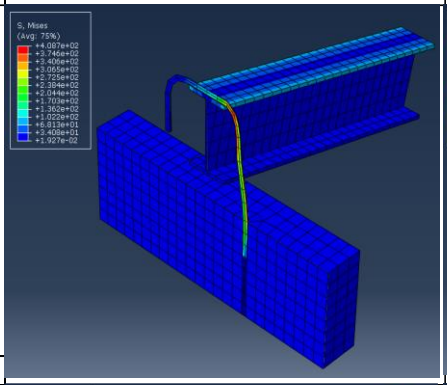	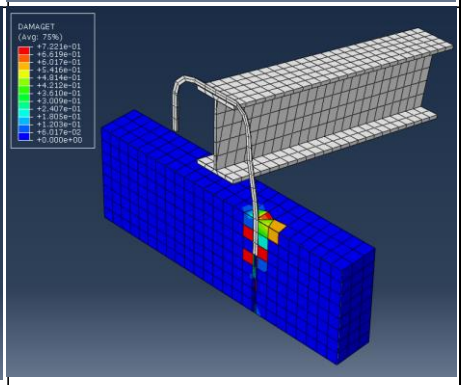
mm	0.072138		
Max Force(N)	28480	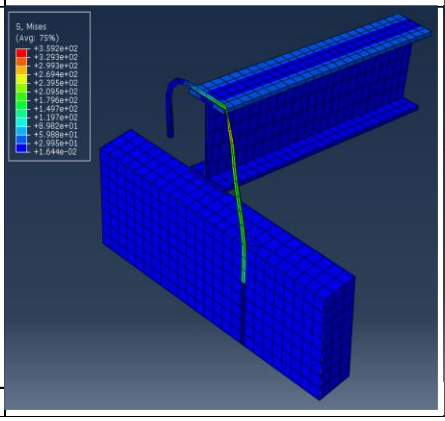	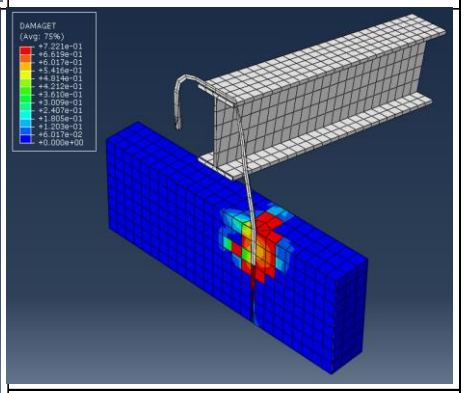
mm	0.68		number of damaged elements =116

Figure 89: Connection 2b1 stepped analysis summary

		Conn-3 Steel Von Mises Stress	Conn-3 Concrete Damage
1/4 Max Force(N)	17876.7	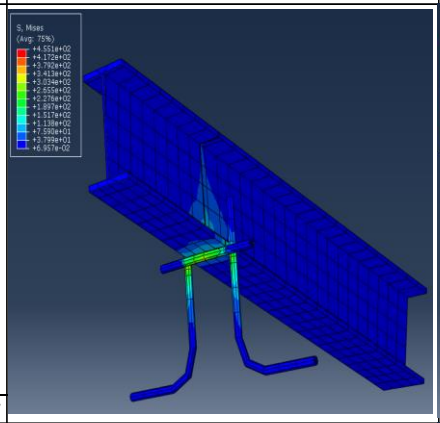	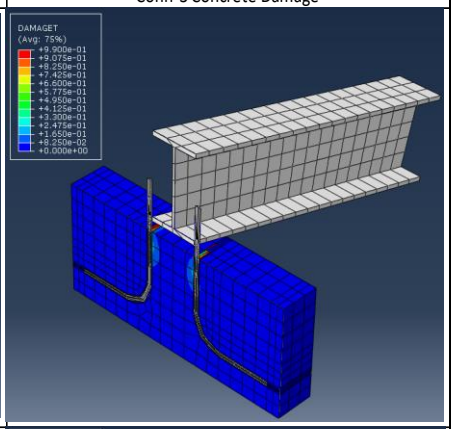
mm	0.000447		
1/2 Max Force(N)	39437.4	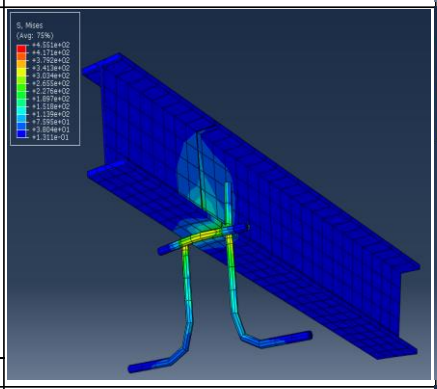	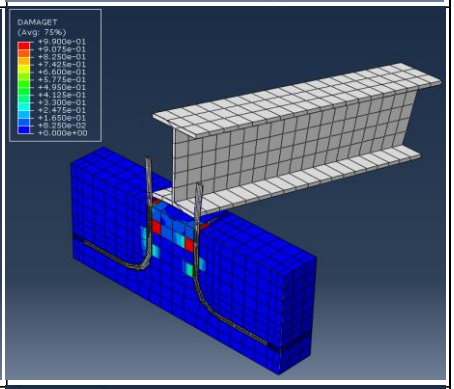
mm	0.004712		
Max Force(N)	78596	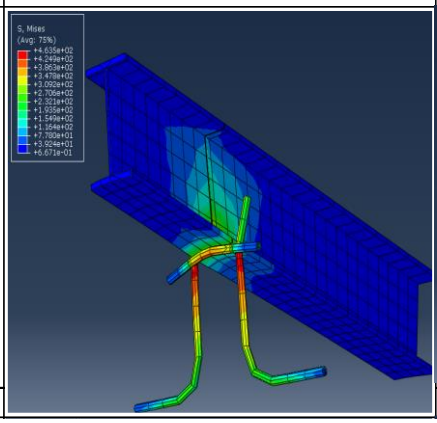	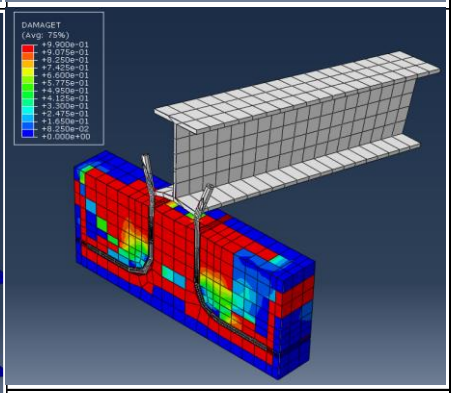
mm	0.43		number of damaged elements =1790

Figure 90: Connection 3 stepped analysis summary

		Conn-3a1 Steel Von Mises Stress	Conn-3a1 Concrete Damage
1/4 Max Force(N)	17872.4	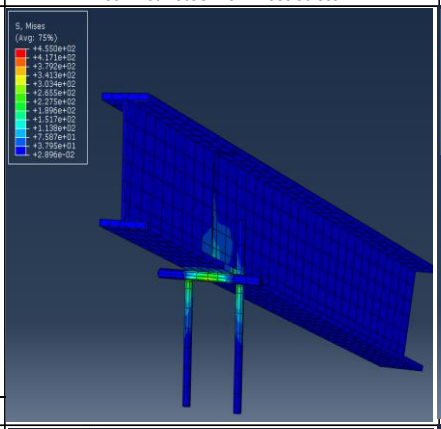	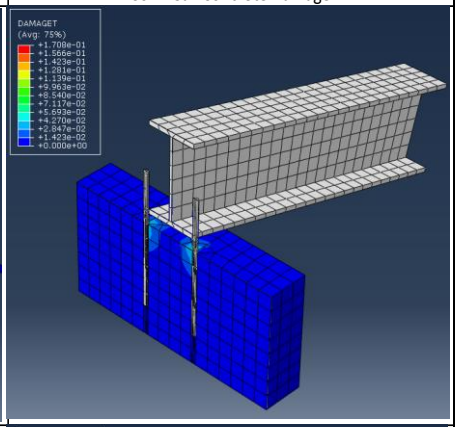
mm	0.000		
1/2 Max Force(N)	50447.7	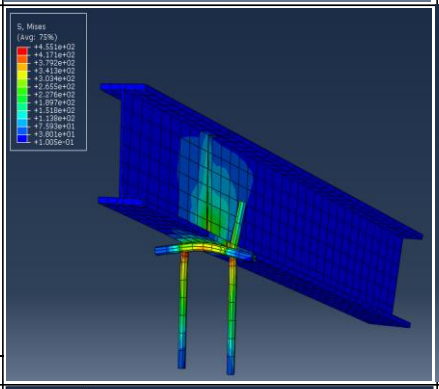	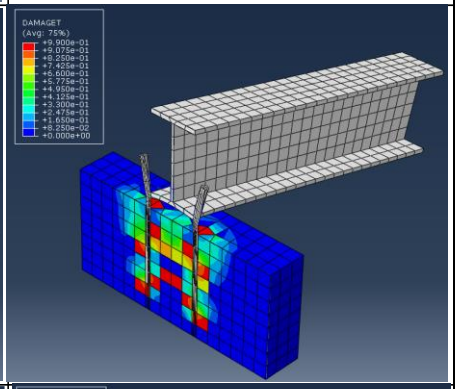
mm	0.055626		
Max Force(N)	67528	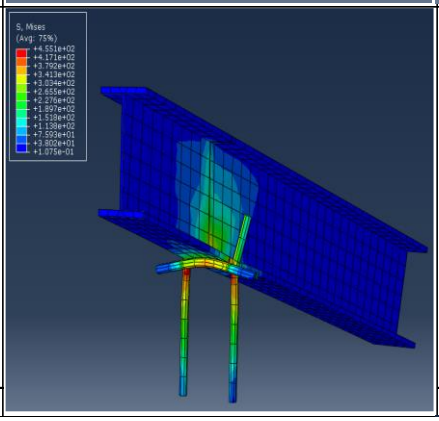	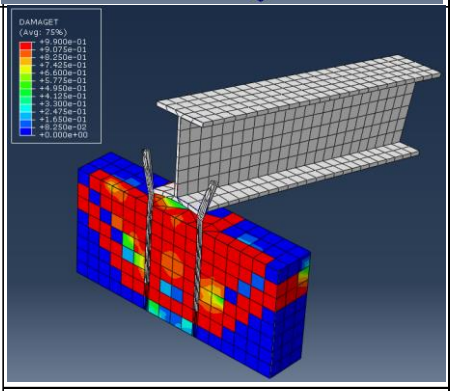
mm	0.87		number of damaged elements =466

Figure 91: Connection 3a1 stepped analysis summary

		Conn-3a2 Steel Von Mises Stress	Conn-3a2 Concrete Damage
1/4 Max Force(N)	25358.7	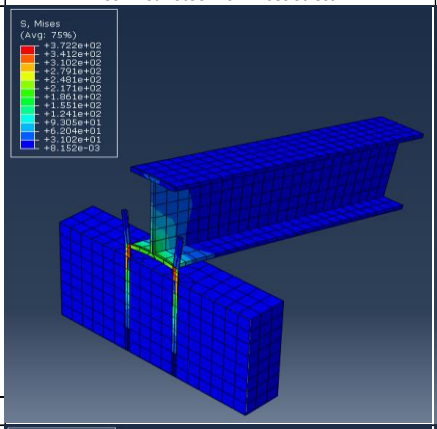	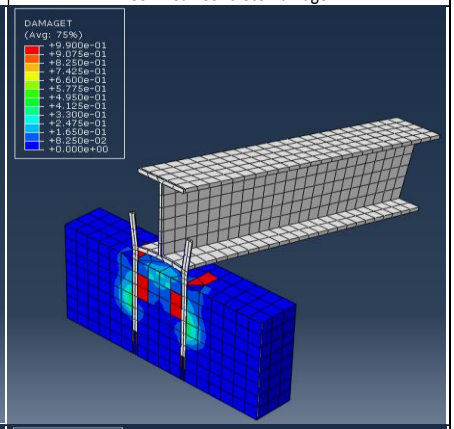
mm	0.025705		
1/2 Max Force(N)	45799.9	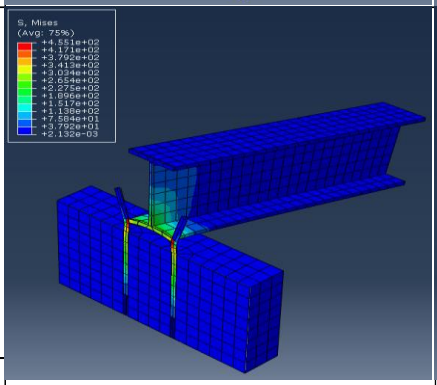	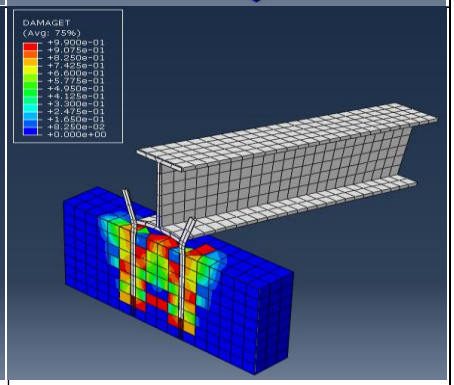
mm	0.055256		
Max Force(N)	62023	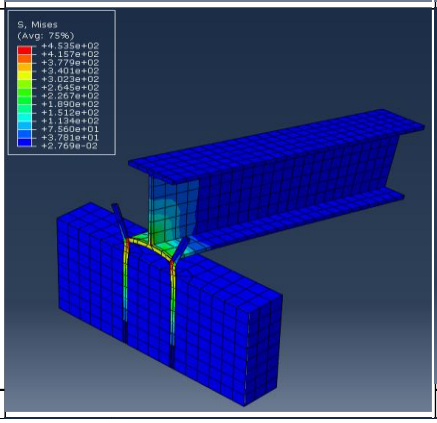	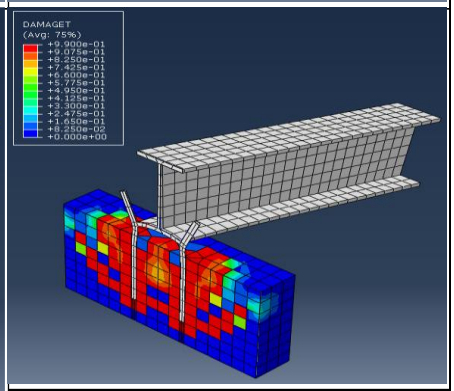
mm	0.56		number of damaged elements =368

Figure 92: Connection 3a2 stepped analysis summary

		Conn-2b1-Retrofit Steel Von Mises Stress	Conn-2b1-Retrofit Concrete Damage
1/4 Max Force(N)	15285.2	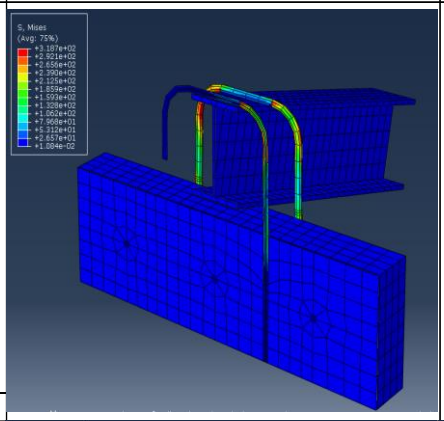	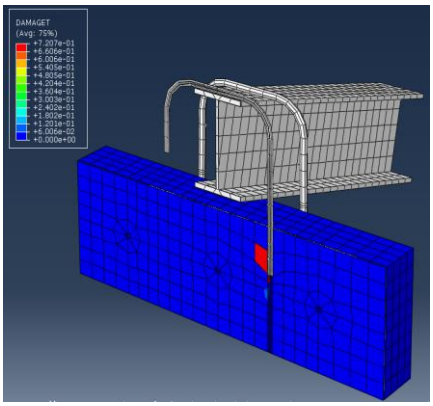
mm	0.07183		
1/2 Max Force(N)	32208.4	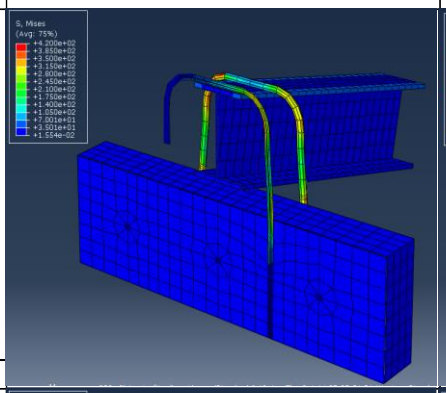	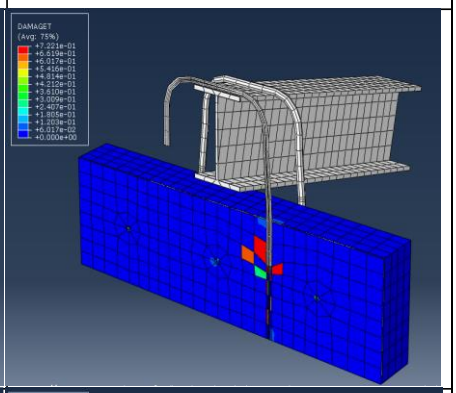
mm	0.02183		
Max Force(N)	84487	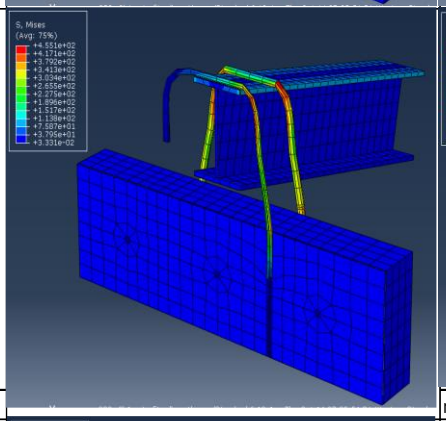	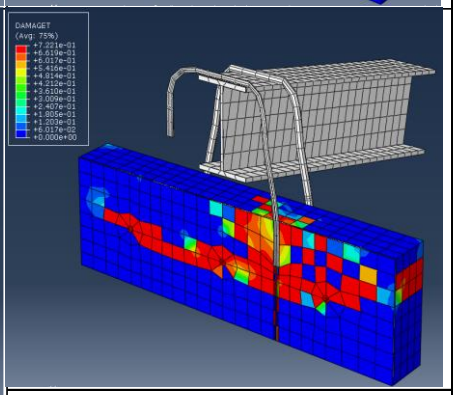
mm	0.41		number of damaged elements =872

Figure 93: Connection 2b1-retrofit stepped analysis summary

4.8.1 Summary of Observed Trends (Steel Anchors)

Figure 84 to figure 93 above show that the stresses in the steel originate at the point of load application i.e., where it connects with the rafter then gradually makes its way down into the concrete ring beam. The pattern of yielding also follows the pattern of stress transfer as the bar starts yielding closest to the point of load application and continues down into the concrete. The anchors for the type 2 connections experience a lot more deformation due to their point of load application (at the top flange of the rafter) being very far from the point of support (at the top of the ring beam). As a result of this, the stresses in the anchors are dissipated mostly via plastic deformation and yielding of the anchors so less stress is available for transfer down into the concrete ring beam. In the type 1 and type 3 connections, the point of load application almost coincides with the point of support i.e., at the bottom flange of the rafter near to the top of the ring beam so stresses are easily transferred through the anchors down into the concrete ring beam.

4.8.2 Summary of Observed Trends (Concrete Ring Beam)

Figure 84 to figure 93 above shows that the damage in the concrete is more significant in the type 1 and type 3 connections due to their point of load application being closer to the point of support i.e. at the top of the ring beam, this allows for better stress transfer from the rafter to the concrete ring beam. The crack patterns observed in the concrete ring beam are an indication of damage. The extent of damage is much larger at the top of the ring beam and gets less towards the base of the anchor forming a distinctive upside-down cone shaped damage pattern. The upside-down cone shaped crack pattern also indicates that the concrete failure follows a typical shear plane where it originates at the anchor base and extends diagonally upward toward the surface of the ring beam. This indicates that higher stresses are developed at the top of the ring beam and dissipates downwards towards the base of the anchor.

If a comparison is made between connection 2 and connection 2a in figure 85 and figure 86 respectively, it can be seen that the hooked bars of connection 2 inflicted more damage and wider crack patterns in the ring beam than the straight bars of connection 2a.

If a comparison is made between connection 2a and connection 2b in figure 86 and figure 88 respectively, it can be seen that the single anchors of connection 2a inflicted less damage to the concrete ring beam than the double anchors of connections 2b.

Figure 89 above for connection 2b shows that a connection with less anchor embedment inflicts less ring beam damage and experiences more anchor slippage than a connection with more anchor embedment. Connection 2b had an anchor embedment of only 75mm.

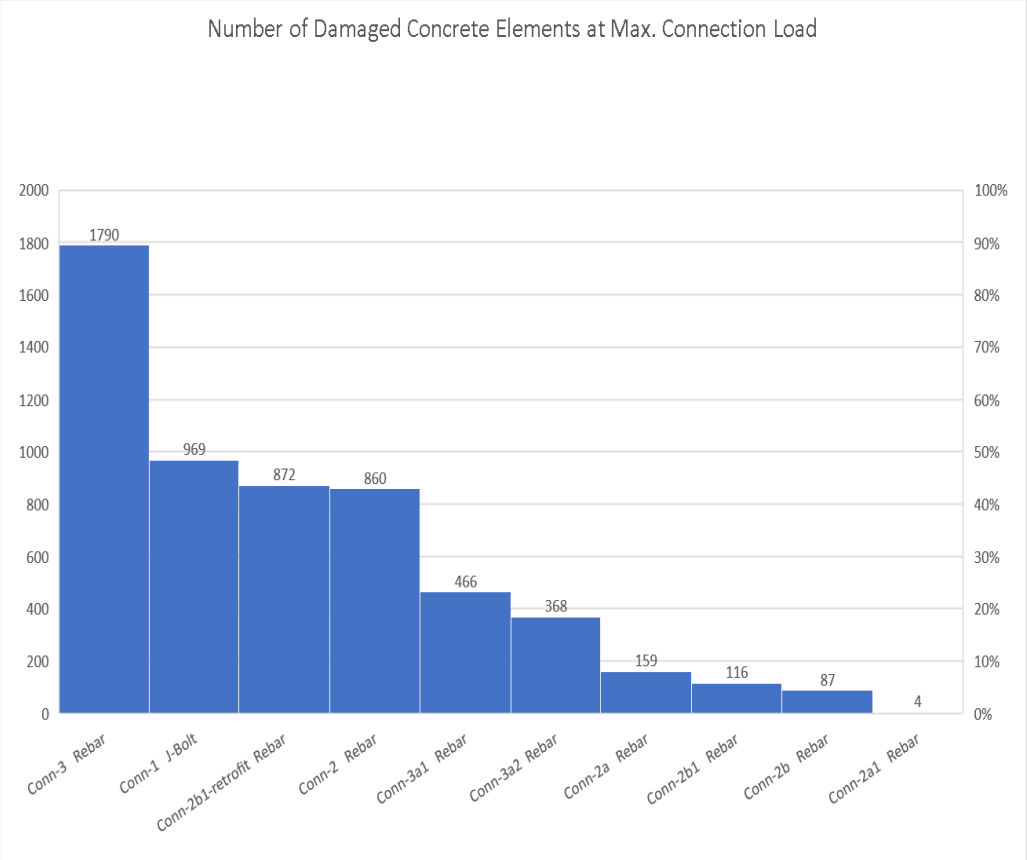

Figure 94: No. damaged concrete elements at maximum connection load

Table 6: Summary of all analysis results at maximum connection load

	force at max conn. load	rafter displacement at max conn. Load	top of rebar displacement at max conn. Load	bottom of rebar displacement at max conn. Load	Number of damaged concrete elements at max conn. Load
Conn-1 J-Bolt	96751	3.556	1.585	1.249	969
Conn-2 Rebar	49706	24.689	1.326	0.032	860
Conn-2a Rebar	80113	175.337	0.101	0.013	159
Conn-2a1 Rebar	2671	12.625	0.000	0.000	4
Conn-2b Rebar	39210	182.468	1.959	0.015	87
Conn-2b1 Rebar	28480	50.778	1.238	0.678	116
Conn-3 Rebar	78596	18.794	4.886	0.427	1790
Conn-3a1 Rebar	67528	10.937	1.243	0.870	466
Conn-3a2 Rebar	62023	11.715	1.647	0.555	368
Conn-2b1-retrofit Rebar	84487	24.434	1.196	0.407	872

Table 7: Percent diff. bet. the control (type-1) & the type 2 & 3 connections

	Percent Difference from Connection-1 (+ve value=percent increase, -ve value=percent decrease)				
	force at max conn. load	rafter displacement at max conn. Load	top of rebar displacement at max conn. Load	bottom of rebar displacement at max conn. Load	Number of damaged concrete elements at max conn. Load
Conn-2 Rebar	-49%	594%	-16%	-97%	-11%
Conn-2a Rebar	-17%	4830%	-94%	-99%	-84%
Conn-2a1 Rebar	-97%	255%	-100%	-100%	-100%
Conn-2b Rebar	-59%	5031%	24%	-99%	-91%
Conn-2b1 Rebar	-71%	1328%	-22%	-46%	-88%
Conn-3 Rebar	-19%	428%	208%	-66%	85%
Conn-3a1 Rebar	-30%	208%	-22%	-30%	-52%
Conn-3a2 Rebar	-36%	229%	4%	-56%	-62%
Conn-2b1-retrofit Rebar	-13%	587%	-25%	-67%	-10%

Table 6 and table 7 above show that with respect to **Maximum Connection Load**, connection 2a1 in which the anchors were not welded to the rafter, had the largest reduction in force i.e. a 97% reduction in force compared to the controlled connection (connection-1). Connection 2b1which had just one anchor achieved the next largest reduction in connection load i.e. a 71% reduction in connection load compared to the control connection. Connection 2a had a 17% reduction in connection load and the retrofit connection had a reduction of 13%, these two connections attained the least reductions in connection load compared to the controlled connection (connection-1).

Table 6 and table 7 above show that with respect to the **Rafter Vertical Displacement**, the type 3 connections i.e. connections 3, 3a1 and 3a2 had the least reduction in rafter vertical displacements compared with the controlled connection (connection-1). These connections were able to provide better stiffness and restraint to the rafter due to their anchors being welded to the bottom flange of the rafters just above the ring beam. On the other hand, the type 2 connections: 2a, 2b and 2b1 were more flexible and had the largest increase in rafter vertical displacement due to their anchors being welded to the top flange of their rafters far away from the ring beam. The stiffness of the connections was proven to be higher when the point of load application to the anchors i.e., the point where it is welded to the rafter is closer to the point of restraint of the anchors i.e., the top of the ring beam.

Table 6 and table 7 above show that with respect to the **Number of Damaged Concrete Elements**, the type 2 connections: 2a1,2b and 2b1 had the largest reductions in the number of damaged concrete elements compared with the controlled connection (connection-1). The highest extent of concrete damage was found in connection 2 and connection 3. Connection 2 had a 11% reduction in concrete damage while connection 3 had an 85% increase in concrete damage. These connections displayed the most concrete damage due to the 90-degree hooks on the end of their anchors which would have resulted in the concrete stresses being distributed over a wider area of the ring beam.

4.8.3 Steel-Concrete Interface & Crack Analysis

The control connection (connection type-1) was analyzed with a much finer mesh to show a better depiction of damage and the propagation of cracks in the concrete. The results are shown below in figure 95 and shows that the concrete damage initiates at the top of the ring beam at the concrete-steel interface and radiates downward alongside the bar before spreading laterally in an upside-down cone shaped pattern.

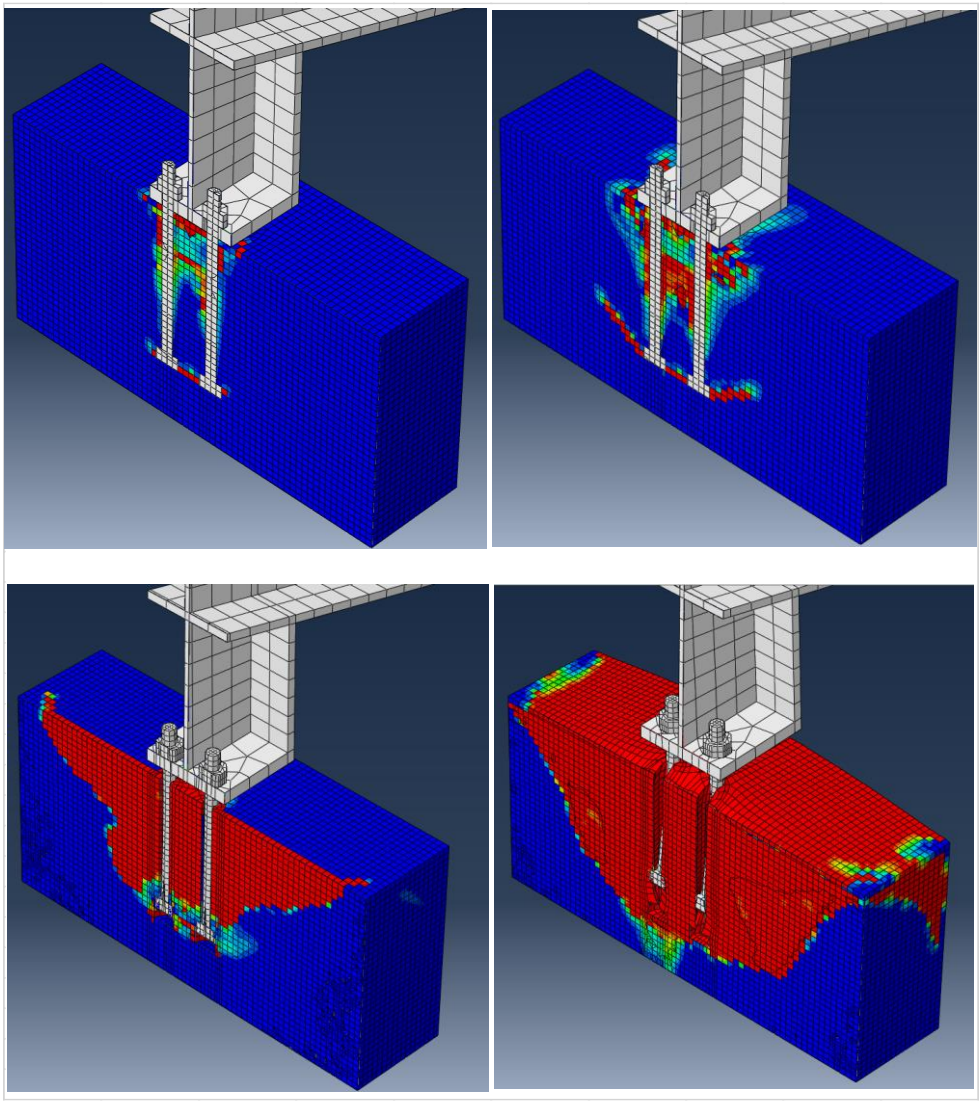

Figure 95: Damage and crack pattern illustrated using finer mesh

CHAPTER 5

CONCLUSIONS

Connection Analysis:

- The connections were expected to withstand hurricane category 1 unfactored loading ranging from 15,183 newtons for a single story to 71,449 newtons for a 3-story. These loads were for typical combinations of rafter spans and spacings.
- For typical combinations of rafter spans and spacings, nine of the ten tested connections had a maximum load capacity that could withstand unfactored loads associated with a category 1 hurricane. The load capacity of these connections was 17% to 70% lower than the control connection.
- Connection type 2a1 was the only connection that was unable to withstand the range of unfactored loads associated with a category 1 hurricane. The anchor rods for this connection were physically wrapped around the top of the rafter and not welded to the rafter as with the other connections. This connection therefore did not possess the capacity to withstand even the lowest level of hurricane category 1 loading and had 97% less load carrying capacity that the control connection.
- The control connection possessed superior load capacity and stiffness compared with the other connections.
- The retrofitted connection attained a load capacity comparable to the control connection. The load carrying capacity of the retrofitted connection was just 13% less than the control connection but higher than all the other tested connections.
- The type 3 connections (anchor rebar welded to the bottom flange of the rafter) inflicted more damage to the concrete ring beam compared with the type 2 connections (rebar anchor welded to the top flange of the rafter). For the type 3 connections, the point of load application (anchor weld to bottom flange of rafter) was much closer to the point of support (top of the

ring beam) and this resulted in more efficient load transfer from the anchors to the ring beam. For the type 2 connections, the point of load application (anchor weld to top flange of rafter) was much further from the point of support (top of the ring beam). This resulted in less efficient load transfer from the anchors to the ring beam as the load was being dissipated during yielding and deformation of the anchors.

- The connections with hooks at the end of their anchors inflicted more damage to the concrete ring beam than the connections without hooks.
- An embedment length of 120mm for an unhooked 12mm diameter anchor was sufficient to prevent pull-out failure for the type 2 connections (anchors welded to top flange of the rafter).
- An embedment length of 205mm for an unhooked 12mm diameter anchor was sufficient to prevent pull-out failure for the type 3 connections (anchors welded to bottom flange of the rafter).
- The type 2 connections (rebar anchor welded to the top flange of the rafter) had 71% more pull-out capacity than the type 3 connections (anchor rebar welded to the bottom flange of the rafter). For the type 2 connections, the point of load application (anchor weld to top flange of rafter) was much further from the point of support (top of the ring beam). This resulted in less efficient load transfer from the anchors to the ring beam as the load was being dissipated during yielding and deformation of the anchors. Less load was available to cause bond slippage at the steel/concrete interface within the ring beam.
- Increasing the diameter of the anchor increased the capacity of the connection but a larger embedment depth was required for the anchor to develop its maximum connection load. The analysis showed that for one of the connections, there was a 74% increase in load capacity when a 16mm diameter anchor was used instead of a 12mm diameter anchor.

Steel Anchor and Concrete Ring Beam Stress Analysis:

- Analysis showed that the connection load initially produces stress in the rafter and in the anchors at the top of the ring beam, this stress then travels down the anchors into the ring beam, resulting in yielding of the anchors progressively from top to bottom.
- Maximum stresses at the top of the anchors were found to be greater than at the bottom of the anchors.
- Stress travelling down the anchor is transferred to the concrete matrix through the interfacial bond. The interfacial bond gradually degrades resulting in slippage of the anchor from the concrete.
- Stress travels through the concrete matrix causing damage or degradation in the elastic stiffness of the concrete. Concrete damage originates at the steel-concrete interface and radiates outward in an upside-down cone shaped pattern i.e. more damage at the top of the anchor and less damage at the base of the anchor.
- Rebar anchors with short embedment depths inflicted less damage to the concrete ring beam.
- Rebar anchors terminating with a 90-degree hook provide better anchorage but inflicted more damage to the ring beam.

CHAPTER 6

RECOMMENDATIONS

- Ensure that ring beams are adequately reinforced to minimize concrete damage particularly when using the type 3 connections (anchor rebar welded to the bottom flange of the rafter) which have been proven in this study to be more damaging to the ring beam.
- All embedded anchors should terminate with a 90-degree hook and the ring beam should be adequately reinforced to minimize damage. Anchors with 90-degree hooks have been proven in this study to be more damaging to the ring beam.
- Ensure that at least two anchors are used to restrain the rafter. In this study, two anchors have been proven to be more efficient than one anchor.
- Avoid the use of plain/smooth rebars which have a lower pull-out resistance than corrugated rebars.
- Larger diameter rebars can be used to increase the capacity of the connection. Larger diameter bars have been proven in this study to provide better pull-out capacity than smaller diameter rebars, as long as they are adequately embedded.
- Connections with inadequate anchorage can be retrofitted using the retrofitted connection proposed in this study.
- Ensure that adequate welds can be provide to anchor the rebar to the rafter by using the appropriate grade of steel for the rebar e.g., using ASTM A706 rebar which is a high strength, low-carbon weldable grade of steel as opposed to the ASTM A615 high-carbon steel which is commonly used and which unsuitable for welding.

REFERENCES

Abaqus Documentation. 2017a. "Concrete Damaged Plasticity." n.p. https://abaqus-docs.mit.edu/2017/English/SIMACAEMATRefMap/simamat-c-concretedamaged.htm.

———. 2017b. "Defining the Constitutive Response of Cohesive Elements Using a Traction-Separation Description." n.p. https://abaqus-docs.mit.edu/2017/English/SIMACAEELMRefMap/simaelm-c-cohesivebehaviour.htm.

Abrams, D.A.B. 1913. *Tests of Bond between Concrete and Steel*. Vol. XI. Champaign, IL, United States: University of Illinois Urbana-Champaign. https://books.google.tt/books?id=jKCeDAEACAAJ.

ACI (American Concrete Institute) Committee 318. 2003. *Bond and Development of Straight Reinforcing Bars in Tension.* ACI 408R 03. Farmington Hills, MI: American Concrete Institute.

ASTM (American Society for Testing and Materials). 2016. *Standard Specification for Deformed and Plain Carbon-Steel Bars for Concrete Reinforcement.* ASTM A615. West Conshohocken, PA: ASTM International.

Beliaev, Mikhail, Semenov Artem, Semenov Sergey, and Andrey Benin. 2016. "Simulation of Pulling the Reinforcing Bar from Concrete Block with Account of Friction and Concrete Damage." In *Topical Problems of Architecture, Civil Engineering, Energy Efficiency and Ecology: MATEC Web of Conferences*, Tyumen, Russia, April 27-29, 2016 edited by Tatiana Maltseva,73: 1-7. Les Ulis Cedex A, France: EDP Sciences. https://doi.org/10.1051/matecconf/20167304010.

Bennett, E.W., and I. G. Snounou. 1982. "Bond-Slip Characteristics of Plain Reinforcing Bars under Varying Stress." *J-Global-Japan Science and Technology Agency*:140-150. https://jglobal.jst.go.jp/en/detail?JGLOBAL_ID=200902020562976925.

Bouazaoui, L., and A. Li. 2008. "Analysis of Steel/Concrete Interfacial Shear Stress by Means of Pull out Test." *International Journal of Adhesion and Adhesives* 28:101–108. https://doi.org/10.1016/j.ijadhadh.2007.02.006.

Braxton-Benjamin, Nikita 2021. "Grateful for Sunshine, Residents Get Chance to Clean up, Repair Roofs." *Trinidad Express*, September 4, 2021. https://trinidadexpress.com/-news/local/grateful-for-sunshine-residents-get-chance-to-clean-up-repair-roofs/article_187cd29c-0de2-11ec-90b0-173284e10b99.html.

Bulck, S. V. D. 2015. "Numerical Analysis of Rebar Pull-out Behaviour in Concrete Using Cohesive Zone Modelling." Masters Thesis. Department of Architecture, Building and Planning, Unit Structural Design. The Eindhoven University of Technology. https://pure.tue.nl/ws/portalfiles/portal/46914164/801714-1.pdf.

Camanho, Pedro, and Carlos Dávila. 2002. *Mixed-Mode Decohesion Finite Elements for the Simulation of Delamination in Composite Materials*. Hampton, Virginia: NASA. https://ntrs.nasa.gov/citations/20020053651.

Carvalho, Eliene, Efigênia Ferreira, José Cunha, Conrado Rodrigues, and Nilton Maia. 2017. "Experimental Investigation of Steel-Concrete Bond for Thin Reinforcing Bars." *Latin American Journal of Solids and Structures* 14:1932-1951. https://doi.org/10.1590/1679-78254116.

CEB (Comité Euro-International du Béton) FIB (International Federation for Structural Concrete). 2010. *Ceb Fib Model Code.* Lausanne, Switzerland: International Federation for Structural Concrete. https://www.fib-international.org/publications/fib-bulletins/model-code-2010-first-complete-draft,-vol-1-pdf-detail.html.

Claudio Amadio, Nader Akkad, and Marco Fasan. 2015. "Three-Dimensional Numerical Simulations of Steel Concrete Composite Beam-to-Column Welded and Bolted Joints." Paper presented at the 8th International Conference on Behaviour of Steel Structures in Seismic Areas, Shanghai, China, July 1 to 3, 2015. https://www.academia.edu/64315968.

Darwin, David, and Ebenezer Graham. 1993. "Effect of Deformation Height and Spacing on Bond Strength of Reinforcing Bars." *ACI Materials Journal* 90 (6): 646-657. https://kuscholarworks.ku.edu/bitstream/handle/1808/31447/Darwin_and_Graham_1993_90-S65.pdf?sequence=1&isAllowed=y.

Edwards, A. D., and P. J. Yannopoulos. 1979. "Local Bond-Stress–Slip Relationships under Repeated Loading." *Magazine of Concrete Research* 31 (107): 109-109. http://ejournals.ebsco.com/direct.asp?ArticleID=40E99EAFF13F9BE58903.

Eligehausen, R., E.P. Popov, and V.V. Bertero. 1982. "Local Bond Stress Slip Relationship of Deformed Bars under Generalized Excitations". *Earthquake Engineering Research Center, University of California* UCB/EERC-83/23: 1-180 Berkeley, California: National Technical Information Service. https://doi.org/10.18419/OPUS-8473.

Ensink, S.W.H., A. van de Graaf, Arthur Slobbe, Man Hendriks, J. A. den Uijl, and Jan G. Rots. 2012. "Modelling of Bond Behaviour by Means of Sequentially Linear Analysis and Concrete-to-Steel Interface Elements." In *Proceedings of the Fourth International Symposium-Bond in Concrete 2012: Bond, Anchorage, Detailing. Vol. 1, General Aspects of Bond*, Brescia, Italy, 17th - 20th June 2012, edited by J. Cairns, G. Metelli and G.A. Plizzari,Manerbio, Brescia: Publisher Creations.

Filho, Fernando, Silvana De Nardin, and Ana Debs. 2019. "Numerical Approach of the Steel-Concrete Bond Behaviour Using Pull-out Models." *Matéria-Rio de Janeiro* 24 (2): 1-14. https://doi.org/10.1590/s1517-707620190002.0656.

Gangolu, Appa Rao, Krishnamurthy Pandurangan, F. Sultana, and Rolf Eligehausen. 2007. "Studies on the Pull-out Strength of Ribbed Bars in High-Strength Concrete." In *Proceedings of the 6th International Conference on Fracture Mechanics of Concrete and Concrete Structures: Fracture Mechanics of Concrete and Concrete Structures*, Catania, Italy, 17-22 June, 2007, 1: 1-6. London: Taylor & Francis. https://framcos.org/FraMCoS-6/295.pdf.

Gangolu, Appa Rao, S. Priyanka, and Rolf Eligehausen. 2016. "Prediction of Analytical Bond Strength of Lap Splices in Tension." In *9th International Conference on Fracture Mechanics of Concrete and Concrete Structures: International Association of Fracture Mechanics for Concrete and Concrete Structures (IA-FraMCoS)*, Berkeley, USA, 28 May to 01 June, 2016, edited by V. Saouma, J. Bolander and E. Landis,1-12. Westerville , USA: Material Sciences. https://doi.org/10.21012/FC9.213.

Gibbs, Tony. 2000. "Detailing for Hurricanes." Paper presented at USAID/ OAS/CCEO Course On Multi-Hazard Building Design (For The Caribbean), Basseterre, St. Kitts, November 13-17, 2000, B3.1. https://www.oas.org/pgdm/document/mhbdc/b3_text.pdf.

Goto, Yukimasa. 1971. "Cracks Formed in Concrete around Deformed Tension Bars." *ACI Journal Proceedings* 68 (4): 244-251. https://doi.org/10.14359/11325.

Holder, Lincoln. 2020. "Photos of the Day." *Trinidad and Tobago Newsday*, October 14, 2020. Accessed September 7, 2021. https://newsday.co.tt/2020/10/14/photos-of-the-day-october-14-2020/.

Jankowiak, Tomasz, and Tomasz Lodygowski. 2005. "Identification of Parameters of Concrete Damage Plasticity Constitutive Model." *Foundations of Civil and Environmental Engineering* 6:53-69. https://www.infona.pl/resource/bwmeta1.element.baztech-article-BPP1-0059-0053/tab/summary.

Kachanov, L. M. 1999. "Rupture Time under Creep Conditions." *International Journal of Fracture* 97:11-18. https://doi.org/10.1023/A:1018671022008.

Kankam, Charles K. 1997. "Relationship of Bond Stress, Steel Stress, and Slip in Reinforced Concrete." *Journal of Structural Engineering* 123 (1): 79-85. https://doi.org/doi:10.1061/(ASCE)0733-9445(1997)123:1(79).

Lee, J., and G. L. Fenves. 1998. "Plastic-Damage Model for Cyclic Loading of Concrete Structures." *Journal of Engineering Mechanics* 124 (8): 1-9. https://doi.org/10.1061/(ASCE)0733-9399(1998)124:8(892).

Lettow, S., U. Mayer, and R. Eligehausen. 2003. "Experimental Investigations on the Bond Behaviour of Ribbed Reinforcing Bars." Doctor of Engineering. The Faculty of Civil and Environmental Engineering. University of Stuttgart: Institute for Materials in Construction. https://d-nb.info/984711392/34.

Lin, Hongwei, Yuxi Zhao, Peng Feng, Hailong Ye, Josko Ozbolt, Cheng Jiang, and Jia-Qi Yang. 2019. "State-of-the-Art Review on the Bond Properties of Corroded Reinforcing Steel Bar." *Construction and Building Materials* 213:216-233. https://doi.org/10.1016/j.conbuildmat.2019.04.077.

Lubliner, Jacob, Javier Oliver, Sergio Oller, and Eugenio Oñate. 1989. "A Plastic-Damage Model for Concrete." *International Journal of Solids and Structures* 25 (3): 299-326. https://doi.org/10.1016/0020-7683(89)90050-4.

Lundgren, Karin. 1999. "Three-Dimensional Modelling of Bond in Reinforced Concrete." Ph.D diss. Chalmers University of Technology. https://research.chalmers.se/en/publication/775.

Lutz, Leroy A., and Peter Gergely. 1967. "Mechanics of Bond and Slip of Deformed Bars in Concrete." *American Concrete Institute Journals and Proceedings* 64 (11): 711-721. https://doi.org/10.14359/7600.

Martin, H. 1982. "Bond Performance of Ribbed Bars (Pull-out-Tests) - Influence of Concrete Composition and Consistency." *Journal of Science and Technology*:289-299. https://jglobal.jst.go.jp/en/detail?JGLOBAL_ID=200902088356854531.

Murcia-Delso, Juan, Andreas Stavridis, and Pui shum Shing. 2013. "Bond Strength and Cyclic Bond Deterioration of Large-Diameter Bars." *ACI Structural Journal* 110 (4): 659-670. https://doi.org/10.14359/51685751.

Mylrea, T.D. 1948. "Bond and Anchorage." *Journal of the American Concrete Institute* 44 (3): 521-552. https://www.concrete.org/publications/internationalconcreteabstractsportal/m/details/id/12190.

Olesen, S. E., M. A. Sozen, and C. P. Siess. 2008. "Investigation of Prestressed Reinforced Concrete for Highway Bridges, Part v: Strength in Shear of Beams with Web Reinforcement." *Journal of the American Concrete Institute* 11 (28): 1-110. https://www.concrete.org/publications/internationalconcreteabstractsportal/m/details/id/16580.

Prevatt, D. O., L. A. Dupigny-Giroux, and F. J. Masters. 2010. "Engineering Perspectives on Reducing Hurricane Damage to Housing in Caricom Caribbean Islands." *Natural Hazards Review-ASCE Library* 11 (2): 2-12. http://dx.doi.org/10.1061/(ASCE)NH.1527-6996.0000017.

Rabotnov, Yu N., F. A. Leckie, and W. Prager. 1970. "Creep Problems in Structural Members." *Journal of Applied Mechanics* 37 (1): 249-249. https://doi.org/10.1115/1.3408479.

Rehm, G., and C. Van Amerongen. 1961. *The Basic Principles of the Bond between Steel and Concrete*. London, United Kingdom: Cement and Concrete Association. https://books.google.tt/books?id=V4U1HwAACAAJ.

Sadeghi, Nader, and Akanshu Sharma. 2019. "Pull-out Test for Studying Bond Strength in Corrosion Affected Reinforced Concrete Structures: A Review." *Otto-Graf-Journal* 18:259-272. https://www.mpa.uni-stuttgart.de/institut/publikationen/otto-graf-journal/.

Sahi, Wjdan, Alaa Al-Zuhairi, and Wjdan Al-Fatlawi. 2009. "Bond-Slip Relationship of Reinforcing Steel Bars Embedded in Concrete." Paper presented at the 6th Engineering Conference, College of Engineering, University of Baghdad, Baghdad, Iraq, 5-7 April, 2009, 1: 18-35.

https://www.researchgate.net/publication/310460356_Bond-Slip_Relationship_of_Reinforcing_Steel_Bars_Embedded_in_Concrete.

Shafaei, Jalil, Abdollah Hosseini, and M. Marefat. 2009. "3-D Finite Element Modelling of Bond-Slip between Rebar and Concrete in Pull-out Test." Paper presented at the 3rd International Conference on Concrete & Development, University of Tehran, Tehran, Iran, 27-29 April, 2009, 403-413. Building and Housing Research Center. https://www.irb.fraunhofer.de/CIBlibrary/search-quick-result-list.jsp?A&idSuche=CIB+DC13701.

Tepfers, Ralejs. 1973. "A Theory of Bond Applied to Overlapped Tensile Reinforcement Splices for Deformed Bars." Ph.D diss. Chalmers University of Technology. https://trid.trb.org/view/94375.

The International Union of Laboratories and Experts in Construction Materials, Systems and Structures (RILEM). 1994. "R.C.6. Bond Test for Reinforcement Steel 2. Pull-out Tests." In *Rilem Recommendations for the Testing and Use of Constructions Materials*, 218-220. Haymarket, London: E & FN SPON.

Trinidad and Tobago Small Building Committee. 2004. *Trinidad and Tobago Small Building Code.* n.p. https://www.oecs.org/en/our-work/knowledge/library/sustainable-energy/oecs-building-codes/trinidad-building-codes-and-standards-in-trinidad-and-tobago-pdf.

Vandewalle, L. 1992. "Theoretical Prediction of the Ultimate Bond Strength between a Reinforcement Bar and Concrete." In *Proceedings of the CEB Conference on Bond in Concrete*, Riga, Latvia, October 15-17, 1992, 1.1: 1-8. Lausanne, Switzerland: CEB. https://www.worldcat.org/title/international-conference-bond-in-concrete-from-research-to-practice-proceedings-riga-latvia-october-15-17-1992/oclc/32077098.

Webb, Yvonne. 2019. "Storm Brings Disaster to South." *Trinidad and Tobago Newsday*, August 15, 2019. https://newsday.co.tt/2019/08/15/storm-brings-disaster-to-south/.

Wight, James K., and James G. MacGregor. 2011. *Reinforced Concrete: Mechanics and Design*. Upper Saddle River, New Jersey: Pearson Education. https://ostad.nit.ac.ir/payaidea/ospic/file4019.pdf.

Xing, Guohua, Cheng Zhou, Tao Wu, and Boquan Liu. 2015. "Experimental Study on Bond Behaviour between Plain Reinforcing Bars and Concrete."

Advances in Materials Science and Engineering 2015:1-9. https://doi.org/10.1155/2015/604280.

Yankelevsky, David Z. 1997. "A Two-Phase One Dimensional Model for Steel-Concrete Interaction." *Computers & Structures* 65 (6): 781-794. https://doi.org/10.1016/S0045-7949(97)00075-8.